A STUDY OF PHASE-DEPENDENT LINE-PROFILE VARIATIONS IN WC+O BINARIES

Thesis submitted for the degree of

DOCTOR OF PHILOSOPHY

at the University of Leicester

by

Christopher Lloyd

Space Science Department

Rutherford Appleton Laboratory

and

Department of Physics and Astronomy

University of Leicester

26th January 1998

ProQuest LLC
789 East Eisenhower Parkway
P.O. Box 1346
Ann Arbor, MI 48106-1346

Abstract

Phase-dependent line-profile variations of Wolf-Rayet + O-star binaries provide an opportunity to probe the physical and ionization structure of WR winds and the shock zone between the two stars. A model is developed to calculate the phase-dependent variation in the absorption by the wind, which takes into account the structure of the shock zone, the cavity caused by the O-star wind, and the changing ionization balance of the wind. Observations of the line-profile variations of γ^2 Vel and HD 152270 are discussed in detail and then compared with the model. The variations of the weaker absorption lines, particularly the Fe IV pseudo continuum in γ^2 Vel are shown to be quantitatively consistent with the expectations of selective absorption. The emission lines on the other hand are shown to vary by more than can be explained by selective absorption alone, and in a way which is inconsistent with selective absorption. These variations are broadly consistent with the scenario of excess emission from the shock zone, fueled by the colliding winds. In both stars the ratios of the emission line strengths relative to single WCL stars suggest unusually strong lines which provides additional support to the idea of excess emission. The level of the excess emission in the lines is probably very large, approaching the intensity of the O star in the lines. The fit to the Fe IV pseudo-continuum lines leads to an iron abundance which is approximately 1 – 2 times solar in both γ^2 Vel and HD 152270. By modelling the region around the N IV λ1718 line it is possible to reduce the upper limit of the nitrogen abundance in WC stars by about 2 orders of magnitude, giving C/N $>$ 1000 and $>$ 20000, in γ^2 Vel and HD 152270 respectively.

Contents

List of Figures

List of Tables

Acknowledgements

Firstly, I would like to thank Jack Meadows who was largely responsible for initiating this project. I would also like to thank my supervisor, Richard Jameson, for his advice and support. In the Wolf-Rayet and wider hot-star community I am pleased to acknowledge the help and advice of many people, including John Hillier, Ian Howarth, Raman Prinja, Ian Stevens and Allan Willis. I would also like to thank Werner Schmutz for our collaborative observing programme on γ^2 Vel during the final year of *IUE* operations and for useful discussions. In particular I would like to thank Dave Stickland for our long term collaboration on hot-star orbits with *IUE* and on our joint observing programmes, his sage advice and professional editorial comments. Finally, I must thank my wife, Margaret, for her continued support, encouragement, and patience.

Chapter 1

Introduction

1.1 Introduction to Wolf-Rayet stars

The evolution of the most massive stars, those with $M_i > 25$, is largely determined by radiation-driven mass loss. Current evolutionary models suggest that early O-type main-sequence stars quickly develop fast stellar winds, which by the time of hydrogen core exhaustion have removed approximately half of the initial mass of the star, exposing the stellar core. The resulting objects have dense stellar winds and their spectra are domination by broad emission lines; they are Wolf-Rayet stars. At this stage the atmosphere contains only a small residual amount of hydrogen. CNO combustion products have been convected to the surface and the composition of the atmosphere is non-solar; little H, enhanced He and N. Subsequent evolution, through He burning will remove the H and N, and the atmosphere will become dominated by C and O, at the expense of He. Evolutionary models are now also being used to calculate WR population statistics in different galactic environments.

Observations support this broad scenario but also reveal complex relationships between the the different classes of luminous massive stars; the evolving O stars, Wolf-Rayet stars and Luminous Blue Variables (LBV). Many evolved massive stars show evidence of episodic mass loss which paint a picture of dynamic and eruptive evolution. Observations of Wolf-Rayet stars and related objects in the Galaxy, the Magellanic Clouds and nearby galaxies also reveal that the characteristics, mass-loss rates, ter-

minal velocities, luminosities etc, are dependent on the environment, i.e. Z, in which the stars are formed.

Modelling WR atmospheres is very difficult because the lines are formed in an expanding, optically thick wind which must be treated spherically and in NLTE. However, the "standard model" as it has become known (Hillier 1995) is now capable of reproducing the observed spectra relatively well, particularly the emission lines. One of the fundamental difficulties of the "standard model" is that the form of the velocity law of the WR wind has to be assumed, and this has to join smoothly to the underlying hydrodynamic structure at low velocities. A second problem with WR atmospheres is that the momentum of the wind appears to be larger than the radiant energy available to drive it.

Of the Wolf-Rayet stars $> 40\%$ are found in binary systems, invariably with massive O stars (but see § 2.2, Cherepashchuk 1996). The evolution of very massive close binaries is a contentious issue depending on the role of mass loss and mass transfer through Roche lobe overflow (RLOF) (see § 2.7). However, whichever is the dominant route it seems likely that there is little difference in the observed properties of WR stars formed by radiation-driven mass loss or mass transfer through RLOF (De Greve 1996). Of the WR+O binaries some 6 show continuum eclipses and are extremely valuable objects for determining the radii and core temperatures of Wolf-Rayet stars. Binaries are also the only means of directly estimating the masses of Wolf-Rayet stars. Rather more of the binaries show what are called "wind eclipses" which are caused when the O star is seen through the WR wind. The light of the O star is selectively absorbed by ions in the WR wind which can lead to dramatic variation in line strengths (Willis & Wilson 1976). The wind eclipses are characterised by phase-dependent profile variations in the lines produced by the wind. More recently the effects of the collision between the winds of the WR star and the O-type companion, which have significant winds in their own right, have been recognised (Shore & Brown 1988). Colliding winds have been shown to generate X-rays but the effects on the wind are only beginning to be explored.

1.2 Phase-dependent line-profile variations

During the orbital cycle of a WR+O binary the continuum of the O star is selectively absorbed by ions in the WR wind, producing a pattern of phase-dependent line-profile variations. The variations are seen in optical spectral but the most suitable lines appear in the ultraviolet and have been observed extensively using the *International Ultraviolet Explorer* satellite. It has been recognised since the discovery of these variations that selective absorption may be used to probe the structure of the WR wind along the line of sight to the O star (Willis et al. 1979). The profile depends in particular on the velocity structure and ionization balance of the wind, and also on the abundance of the element involved. The aim of the work described here is firstly to model the change in absorption and then to verify quantitatively that the selective absorption model is applicable. Finally the model will be used to recover information about the wind velocity law and the abundances. The model requires knowledge of the geometry of the systems, the mass-loss rates and terminal velocities of the stars, and these have to be established first.

1.3 Thesis structure

The thesis begins in Chapter 2 with a brief, general review of Wolf-Rayet stars, their observed properties and a discussion of the status of evolutionary models and model atmospheres. A more detailed discussion of the structure of WR winds is given in Chapter 3 and previous research on phase-dependent variations is described in Chapter4. Chapter 5 describes the model used to calculate the absorption line variation. The spectra used in this study were taken by the *International Ultraviolet Explorer* satellite and details of the instrument, observations and data reduction procedures used are given in Chapter 6. The observations of line profile variations of two WC+O binaries, γ^2 Vel and HD 152270 are discussed in Chapters 7 and 8 respectively and compared with the model. Each chapter ends with a discussion and summary of the conclusion drawn. The final chapter contains a discussion of the results from the two stars and an outline of future work.

Chapter 2

Review of Wolf-Rayet stars

2.1 Prologue

Prior to 1971 Wolf-Rayet stars were considered as rare objects with broad emission lines of He, C and N. The nitrogen and carbon sequences were recognised but it was not known what rôle abundance and ionization played. The widespread realisation that Wolf-Rayet stars were the pure He cores of massive stars took place at the second Wolf-Rayet conference, in Buenos Aires in 1971 (Smith 1995). It had already been shown that it was possible to strip the outer layers from a massive star by mass transfer in a binary system (Kippenhahn & Weigert 1967, Paczynski 1967) to reveal the helium core that might look like a WR star. Single-star evolution appeared less tractable until it was realised that continuous mass loss was large enough to affect the main-sequence evolution of the most massive stars. Conti (1976) proposed the scenario in which massive O-type stars evolved through Of to WN, and set in motion the present wave of Wolf-Rayet research (Maeder 1996).

2.2 Observed properties

The spectra of Wolf-Rayet stars are dominated by broad emission lines of He, N and C. The strongest lines show P-Cygni profiles which indicate that the atmospheres of the stars are expanding at velocities of 1000 – 2500 $\mathrm{km\,s^{-1}}$. Mass-loss rates de-

termined by a variety of methods give $\dot{M} \sim (2 - 10)\times10^{-5}$ $M_\odot\,yr^{-1}$ (e.g., Prinja et al. 1990, Willis 1991b), about an order of magnitude higher than for O-type stars. The spectra define three classes of WR stars the WN, WC and WO stars which are dominated by lines of nitrogen, carbon and oxygen respectively. Spectroscopically the WN and WC stars are very different while the WC and WO stars share many characteristics. The level of ionization seen in the WN and WC stars is broadly similar and increases through the sequence from late (WNL, WCL) to early (WNE, WCE) types. The WO classification was introduced by Barlow & Hummer (1982) for stars whose optical spectra are dominated by the high ionization O VI λ 3811, 3834 doublet. Polcaro et al. (1996) argue that these stars are more correctly an extension of the WC sequence to higher ionizations rather than a separate class, and show characteristics intermediate between WO and WC4. Recent observations show very high ionization stages, up to O VIII, and very high terminal velocities of $\sim$ 5000 $km\,s^{-1}$. Intermediate objects showing WN and WC features have also been observed but are relatively rare. HD 62910 (WR8, WN6-C4) has been shown to be a single star (Willis & Stickland 1990) and Conti & Massey (1989) suggest that most of the other examples are also single, intermediate objects. The galactic population of WR stars was recently determined as 201, comprising 112 WN, 7 intermediate WN/WC, 79 WC and 3 WO. The LMC contains 114 and the SMC 9 known WR stars (all binaries) and an increasing number are being discovered in nearby galaxies. Recent reviews of the O and WR classification schemes and observed properties have been given by van der Hucht (1996) and Willis & Crowther (1996). The masses of WR stars determined from binaries cover a very wide range, 5 - 48 $M_\odot$, or even 86 $M_\odot$ (HD 92740) but the mean masses are WN = 23 $M_\odot$, WC = 13 $M_\odot$, and the mass of the WO4 = 14 $M_\odot$, which provide qualitative support for the evolutionary scenario. Direct information on the radii of WR stars comes largely from V444 Cyg and suggests a core radius $\simeq$ 4 $R_\odot$ which is typical of the more recent theoretical values (Cherepashchuk 1996). Finally there are two particularly anomalous and variable objects. The galactic star Cyg X-3 (WN4-7+c) may contain a neutron star (van Kerkwijk et al. 1996) or black hole (Schmutz et al. 1996) and in HD 5980 (WN+O nominally) in the SMC one of the components has undergone an outburst (see van der Hucht 1996).

2.3 Of/LBV/WR transition objects

Walborn (1971, 1973) drew attention to the similar properties of Of stars and WN stars in Carina OB1, and in particular to HD 93129A (O3f*) and HD 93131 (WR24, WN7+abs, or more recently WN6ha (Smith et al. 1996)). The principal difference is one of degree in the emission lines strengths and the presence of P-Cygni profiles in the WR star as opposed to absorptions in the O star. The LMC star HDE 269227, which Smith (1968b) had given as WN8, Walborn (1977) classified as OIafpe, but suggested that if it were to be classified WN it would have to be WN9 or WN10. Similar uncertainty surrounds the Galactic star HDE 313846 (WR108) which has been classified as WN+OB (Smith 1968b), WN9 (van der Hucht et al. 1981), and most recently WN9ha (Smith et al. 1996). There are many examples of spectroscopically intermediate objects between O3-4f and WN3-7 stars and Ofpe and WN9 stars. Conti & Bohannan (1989) highlighted the problem of differentiating between the least extreme WN stars and the most extreme Ofpe stars and Bohannan (1990) described a smooth progression of spectroscopic properties from Of through the so-called "slash" stars to WN. Quantitative spectral analysis and an atmospheric analysis of the LMC Ofpe/WN9 stars suggest that they all (except HDE 269858 see below) could be classified as WN9-11 stars (Crowther et al. 1995a, Crowther & Smith 1997). Crowther & Bohannan (1997) also conclude that there is little difference in the atmospheric structure and composition of the Galactic O supergiant HD 152408 (O8:Iafpe) and WR108 (WN9ha).

The third member of this group is the class of Luminous Blue Variables (LBV). These are among the most luminous stars and lie close to the Humphreys-Davidson (1979) limit in the HR diagram, which is interpreted as an instability or opacity limit. These stars also show high mass-loss rates, circumstellar shells, but rather slow winds. They are variable on a variety of time scales and include well known stars such as η Carinae, P Cygni and the S Dor and Hubble-Sandage variables. Recent reviews of the LBV's as transition objects have been given by Humphreys & Davidson (1994), Nota et al. (1996) and Morris et al. (1996). Detailed spectral analysis at minimum light of the LBV's He3-519 and AG Car by L.J. Smith et al. (1994) showed that these

stars, which had previously shown Of-type emission and been classified as Ofpe/WN9 (Stahl 1986), were severely depleted in hydrogen, and that WN11 classifications were more appropriate. Conversely one of the original LMC Ofpe/WN9 stars (Bohannan & Walborn 1989), HDE 269858 (R127) has developed an LBV outburst. The close morphological similarity of these groups and their strong physical resemblance is widely taken to imply an evolutionary link between them.

2.4 Evolution

The evolutionary models of Wolf-Rayet stars follow the Conti scenario of evolution with continuous mass loss. Meynet et al. (1994 and references therein) have calculated grids of model for stars up to 120 $M_{\odot}$ and with metal abundances between $Z = 0.001$ and 0.040. The evolution is very sensitive to the mass-loss rates adopted, which for the pre-WR and and WNL phases are in general poorly known, and to the metallicity of the local environment (Maeder 1991, Maeder & Meynet 1994). The models are also unable to take account of any episodic mass loss that may occur during the LBV phase. Recent models (Meynet et al. 1994) use enhanced mass-loss rates (referred to as $2 \times \dot{M}$) over the previous models and are better able to reproduce the lower luminosity WR's and the ratios of BSG to RSG in clusters and the Magellanic Clouds (Maeder 1996). In general luminosities predicted by the models are typically a factor of 2 too large but do show decreasing luminosity and increasing temperatures from late to early spectral types. The evolutionary masses are also a factor of ~ 2 larger than the spectroscopic masses (Herrero et al. 1992, Puls et al. 1996).

The most recent developments concern the thorny subject of mixing. Observationally mixing is suspected for a number of reasons. Enhanced He and N is seen in fast rotating OB stars (Herrero et al. 1992) and in most B and A supergiants (Gies & Lambert 1992, Venn 1993). The ON and OC stars (Walborn 1988), and the existence of the intermediate WN/WC stars (e.g., Conti & Massey 1989) all point to mixing. Mixing processes have been developed by Zahn (1992) for meridional mixing, and for semi-convective mixing by Langer et al. (1985), and suggest that mixing becomes progressively more important at higher masses. Mixing during the H-burning phase

will lead to the formation of many WR stars with a low H content (Maeder 1987) while mixing in the He-burning phase is required to explain the observed frequency of intermediate WN/WC stars (Langer 1991). Maeder (1996) has shown that there will be no mixing by the Zahn theory and has developed a new model which suggests that mixing can yield surface enrichment of He and N appropriate for WNL stars on the main sequence. Generally mixing will prolong WR lifetimes, and for a given mass will enhance the luminosity and reduce radii. In extreme cases mixing can prevent the stars from going through a RSG phase.

As a result of the recent evolutionary theory and work on Ofpe/WN9 and LBV stars different evolutionary sequences have been proposed for O stars depending on their initial mass, M_i. Crowther et al. 1995b (see also Walborn 1989, Crowther & Smith 1997) suggests that for $M_i > 60$ $M_\odot$

O $\Rightarrow$ Of $\Rightarrow$ WNLha $\Rightarrow$WN6-7 $\Rightarrow$ WNE $\Rightarrow$ WC $\Rightarrow$ SN

and for $40 < M_i < 60$ $M_\odot$

O $\Rightarrow$ LBV $\Leftrightarrow$ WN9-11 $\Rightarrow$WN8 $\Rightarrow$ WNE $\Rightarrow$ WC $\Rightarrow$ SN

While Langer et al. (1994) suggest for $M_i > 40$ $M_\odot$

O $\Rightarrow$ Of $\Rightarrow$ H-rich WN $\Rightarrow$ LBV $\Rightarrow$ H-poor WN $\Rightarrow$ H-free WN $\Rightarrow$ WC $\Rightarrow$ SN

For progenitors of lower mass, with $25 < M_i < 40$ $M_\odot$, Chiosi & Maeder (1986) suggest

O $\Rightarrow$ (BSG) $\Rightarrow$ RSG $\Rightarrow$ (BSG) $\Rightarrow$ WNE $\Rightarrow$ (WCE) $\Rightarrow$ SN

Differences in the mass limits and details of the sequences may also depend on Z and rotation. It is likely that for $Z > 0.02$ WNL $\Rightarrow$ WCL avoiding the WNE stage and conversely for $Z < 0.02$ WNL $\Rightarrow$ WCE $\Rightarrow$ WO, mostly avoiding the WCL stage, with WNE not leading to WC stars (Maeder 1996).

2.5 Abundances

Smith (1973a,b) first used the overlapping lines of the He II Pickering and H-Balmer decrement to estimate the level of hydrogen in WR stars. If H is present the He II even-n series lines which coincide with H lines will show an odd-even correlation. Her results showed that hydrogen is depleted in all WN subtypes and that the observational

evidence against any H in WC stars was strong. All the more recent studies (e.g., Conti et al. 1983) have confirmed these findings (see the review by Willis 1991a). Crowther et al. (1995bc) have gone on to show that in general WNL stars do show some hydrogen while WNE do not, although there are well known exceptions. Also Galactic, LMC and M33 WN9-11 stars show the same levels of hydrogen depletion as most other WNL stars (Smith et al. 1994, 1995, Crowther et al. 1995a, 1997, Crowther & Smith 1997). As the stars evolve the C, N and O abundances change from their initial (cosmic) values and approach the CNO-process equilibrium values (e.g., Maeder 1991), which show enhanced N and depleted C and O. In WN stars observed carbon and nitrogen levels are consistent with CNO equilibrium values (Crowther et al. 1995b). By the end of hydrogen shell burning the star has no H and the star has an early WNE spectral classification. With continued evolution the products of He burning appear and the models (e.g., Maeder 1991) predict (C+O)/He $\sim$ 0.5 for high Z and (C+O)/He $>$ 1 for low Z, with H/He = 0 and N/He $< 10^{-7}$. WC stars show no hydrogen and the presence of nitrogen has also never been convincingly demonstrated. On the basis of the UV N IV lines, Smith & Willis (1982, 1983) were able to place a limit on the nitrogen abundance C/N $>$ 60 for WC stars. Eenens & Williams (1992), using 1- and 2-μm spectra, found C/He ratios increasing from WCL to WCE types over the range $\sim$ 0.1 – 0.5 by number, which is consistent with the evolutionary models (see also Smith & Hummer 1988, Smith & Maeder 1991). Finally, neon is predicted to be enhanced by a factor of $\sim$ 10 over solar in WC stars (Maeder 1991), and after some debate this has recently been observed in WR146 Willis et al. (1997).

2.6 X-ray observations

Observations with the *Einstein* satellite revealed that O and WR stars are significant X-ray sources. Pollock (1987, 1989) analysed the *Einstein* IPC observations of 48 WR stars and found $L_X \sim 4$ times greater for single WN stars than single WC stars. The X-ray emission is usually attributed to shocked gas produced by intrinsic instabilities in the radiatively driven wind (Lucy 1982) so it may be no coincidence that WN

stars also show significantly more optical variability than WC stars. This issue is discussed in more detail in § 3.7. Recent *ROSAT* observations (Pollock et al. 1995) of all the 158 stars in the WR catalogue (van der Hucht et al. 1981) show significant fluxes for about 10% of the stars and marginal detections for the rest. *ROSAT* and *ASCA* observations of O stars, reviewed by Willis & Crowther (1996), show a severely attenuated hot component and a cooler component which is formed at large ($> 100\ R_\star$) stellar radii. Hillier et al. (1993) estimate that in ζ Puppis (O4 I(n)f) only about 5% of the total X-ray flux escapes. The WN5 star HD 50896 (WR6) shows a cool spectrum (Willis & Stevens 1996) and the WR+O binary γ^2 Vel (HD 68273) also show a cool component indicative of X-ray emission from the outer parts of the wind (Willis et al. 1995). Pollock also found that WR+O binaries are brighter than single stars (see also Pollock 1995, Pollock et al. 1995) and the excess X-ray emission is generally attributed to the colliding winds of the two components which were predicted theoretically (e.g., Prilutskii & Usov 1976, Cherepashchuk 1976). These observations have fueled recent theoretical developments (e.g., Stevens et al. 1992) on hydrodynamic modelling and observations of colliding wind binaries both, WR+O and O+O. *ROSAT* (Willis et al. 1995) and *ASCA* (Stevens et al. 1996) observations of γ^2 Vel are entirely consistent with the colliding wind model and will be described in more detail in Chapter 7 which is devoted to that star. The other well observed system is the 7.94 year binary WR140 (HD 193793, WC7+O4-5) which is best known for its periodic dust formation around periastron passage. *ROSAT* observations of this system are also consistent with the colliding wind model (Pollock 1995, see also the detailed review by Willis & Crowther 1996).

2.7 Binaries

The proportion of single WR stars to WR+O binaries (at $> 40\%$) is similar to the proportion of O-star binaries (Cherepashchuk 1996). In close binaries Roche lobe over flow (RLOF) in general has an important influence on the evolution of the system. However, opinion is strongly divided over the importance of RLOF as a means of generating Wolf-Rayet stars in the most massive systems. Maeder & Meynet (1994,

see also Maeder 1996) consider the binary route as largely unimportant contributing only 5 – 10% of WR stars while this view has been criticised by Vanbeveren (1996 and references therein), who finds that $\sim$ 80% of O-star binaries in the Galaxy will ultimately contain a WR star. The adopted mass-loss rates used for the single and binary routes have a strong influence on WR lifetimes and therefore on the ratios of WR/O, WNE/WNL and WN/WC stars, but are sufficiently flexible that both can produce the observed values (Vanbeveren 1995, Podsiadlowski et al. 1992, De Greve 1996). One of the consequences of RLOF is the rejuvenation of the initial secondary and this is necessary to produce the high mass companions of some WR stars (e.g., Sk188 WO4+O4 V, HDE 311884 O5 V), the small mass ratios and short periods (e.g., V444 Cyg, CQ Cep, De Greve 1996) observed. However, Moffat (1995) has argued that accretion by the secondary is likely to be prevented by its strong stellar wind. Despite these uncertainties the luminosities and masses of WR stars produced by both routes appear to be very similar (De Greve 1996) and WR components of binaries are also indistinguishable from single WR stars (Moffat 1995).

2.8 Model atmospheres

The classic early papers on line-driven wind theory are those of Lucy & Solomon (1970) and Castor, Abbott & Kline (CAK 1975). Using initially one and then thousands of lines it was shown that luminous early-type stars with modest mass-loss rates could drive a wind at some thousands of $\mathrm{km\,s^{-1}}$. Detailed agreement with observations was not good but the situation improved with a simple modification to the CAK theory. It had been assumed that the radiation field is radial but at small radii this is not true. The introduction of a finite cone-angle correction factor (Friend & Castor 1983, Pauldrach et al. 1986, Friend & Abbott 1986) led to a significantly better agreement with observations. The modified CAK theory was also applied successfully to the WR star V444 Cyg (Pauldrach et al.1985). Other modifications to the standard CAK theory have also been investigated and are reviewed in some detail by Cassinelli (1991). Probably the most significant is the multi-line or multiple-scattering problem which has been studied by Friend & Castor (1983), Abbott & Lucy (1985), Puls

(1987) and Lucy & Abbott (1993). In the standard CAK theory the effect of overlapping lines is ignored so the momentum deposition tends to be overestimated. In the single-scattering limit the ratio of the wind kinetic and radiative momentum, known as the wind performance number, $\eta = \dot{M}v_\infty/(\mathrm{L/c}) \simeq 1$, but in WR stars $\eta \sim 10$ typically (Springman & Puls 1995, Willis & Crowther 1996) and can reach 160. Recent work suggests that multiple scattering can increase the momentum deposition in the wind by up to $\eta \sim 10$ (Lucy & Abbott 1993, Owocki & Gayley 1995, Springman & Puls 1998), much of this is in the outer parts of the wind, $r > 3R_{star}$, which means that the wind continues to accelerate at larger radii. Recently Schulte-Ladbeck et al. (1996) have found that the gradient of the ionization stratification in WN stars in correlated with the wind performance number, which is interpreted as support for multiple scattering.

Current model atmospheres do not use Sobolev theory but instead solve the radiative transfer equations in a spherical model in NLTE using the co-moving frame method. The two main groups of models are those due to Hillier (1987a,b, 1988, 1989, 1990) and to the Kiel group, principally Hamann and co-workers (e.g., Hamann & Wassolowski 1990, Koesterke et al. 1992) and are widely referred to as the "standard model". Their basic assumptions are that the atmosphere is spherically symmetric, stationary, homogeneous and in statistical and radiative equilibrium. For O-type stars subsonic hydrodynamic calculations and metal-line blanketing and blocking may be included. For WR stars this is currently not possible; there is no self-consistent hydrodynamic theory so it is necessary to assume a velocity law, although Schmutz (1997) has attempted to merge the two. Current model atmospheres for O-type stars are more advanced than those of WR stars because the mass-loss rates are lower than for WR stars and the atmospheres are thin.

Synthetic spectra calculated for O stars are in excellent agreement with the observations. Important properties such as the temperature, gravity, radius, luminosity, mass, mass-loss rate, wind velocity and abundance have been obtained for stars in the Galaxy, LMC, SMC, M31 and M33 (Kudritzki 1996). Such is the confidence in the models that it is expected that they may be used to investigate the distance scale to more distant galaxies. Models of WN stars have been extensively compared with

observations and the agreement is generally good. In detail some internal inconsistencies have appeared and there are some systematic differences with the observations. Some relaxation of the assumptions in the standard model will be required to improve the fit to the observations. The problems which need to be addressed include (i) incorrect strengths for some important lines (ii) inconsistent metal-line strengths (iii) electron scattering wings (iv) flat-topped emission lines. Preliminary results (Hillier 1996) suggest that metal-line blanketing actually makes little general difference but can cause changes of a factor of 2 in the strengths of some lines, and even factors of 5 occasionally. Metal-line blanketing is found to change the effective temperature systematically by $\sim$ 2000 K (Hubeny et al. 1998, Schmutz 1998). Introducing clumping or inhomogeneities into the wind (very model dependent) tends to require a lower luminosity and mass-loss rate to produce the same spectrum.

2.9 An opposing view

While the general concepts embodied in the "standard model" are widely accepted there is an opposing view. Underhill (1996, Bhatia & Underhill 1988) continues to propose that Wolf-Rayet stars are pre-main-sequence objects akin to the Herbig Ae/Be stars, but are more massive and have higher temperatures. Underhill does not accept the high mass-loss rates routinely found but prefers values about an order of magnitude lower at $\sim 10^{-6}$ $M_\odot\,yr^{-1}$ similar to those of O stars. Similarly Underhill finds no evidence of chemical anomalies in the spectra of Wolf-Rayet stars; all the stars are found to have solar abundances. The differences in the strengths of the nitrogen, carbon and oxygen lines found in WN and WC stars are caused by different wind densities and electron temperatures. Underhill finds that it is possible to maintain the electron temperatures required in regions with a modest magnetic field of $\sim$ 100 G. Nugis (1991) has applied Underhill's models and found discrepancies of an order of magnitude between the observed and calculated C III and C IV ratios.

On a more philosophical front Underhill dismisses the notion that because two classes of object have similar properties there is likely to be a physical or evolutionary link between them. In particular the similarity of the spectra Ofpe and WN9 stars is

discounted as evidence of an evolutionary connection, but this flies in the face of the recent results (§ 2.3).

Counter arguments in favour of the evolved status of WR stars have been summarised before (e.g., Lamers et al. 1990, 1991) but include (i) the low and decreasing hydrogen content correlated with increasing nitrogen, carbon and oxygen abundance (ii) the high nitrogen abundance found in the nebulae surrounding WR stars (Smith 1996, Rosa & Mathis 1990) (iii)the results of the evolutionary calculations which correctly predict the ratio of WR/O stars and its metal dependence and (iv) the success of the "standard model" in predicting the observed line profiles. Further observational support comes from (v) the continuous carbon dust formation which is seen only around WC stars (e.g., Williams 1996) (vi) the high carbon abundance derived from the X-ray spectrum of the WC7 binary WR140 (Williams et al. 1990) and (vii) the evolved companions found in some WR binaries.

Chapter 3

Structure of Wolf-Rayet Winds

3.1 Physical structure

3.1.1 Symmetry

The major questions about the physical structure of Wolf-Rayet winds are whether or not they are smooth and spherically symmetric. A long-standing argument for spherically symmetric winds has been made by Kuhi (1973) who showed that the flat-topped emission lines seen in many WR stars originate from spherically symmetric, hollow expanding shells. Further evidence comes from a study of eclipsing WR+O binaries and others in which the inclination is known from polarisation measurements. Aslanov & Cherepashchuk (1990) concluded that the characteristics of the optical line emission and X-ray *Bremsstrahlung* are not dependent on the inclination, and by implication the orientation of the rotational axis. Robert (1992) has investigated the moving features in the peaks of some emission lines which are usually attributed to blobs. The time averaged geometries of the blob trajectories appears to be spherical in a number of WR stars. The least direct but nonetheless supporting evidence comes from the excellent fits to the line profiles made by the standard model, which assumes spherical symmetry (Hillier 1995, Hamann 1996).

Arguments for generally non-spherical winds are more circumstantial. One concerns the fate of the angular momentum in the precursors of WR stars, the O stars. The

rotational velocities of O stars range from a few tens to 400 $\mathrm{km\,s^{-1}}$(Conti & Ebbets 1977) and how this angular momentum is transfered or lost as the star evolves, and what effect it has on the wind is unknown. The rotational velocities of WR stars are not known; Schmutz (1990) obtained a value from the H absorption lines in WR138 but this star is now interpreted as a long period WN6+O9 binary (Annuk 1991), and the measurement referred to the O star. Of the other stars with absorption lines it appears that the WNE+abs stars are probably all binaries but the WNL+abs stars are probably single. It is possible that measurements may be made of these few stars but this has not yet been done. Bjorkman & Cassinelli (1993) have considered the effect of rapid rotation on wind structure. Using analytical techniques they found that with increasing rotational velocity the wind would be concentrated towards the orbital plane in what they call a "wind-compressed zone". Ignace et al. (1996) have shown that with modest rotational velocities, $v_e \sim 0.2 v_{\mathrm{critical}}$, it is possible to produce a wind-compressed zone of enhanced density (by a factor ~ 3) towards the equatorial plane. Winds with slower velocity laws will be more affected. Owocki et al. (1994, 1998) have developed this idea using hydrodynamical modelling, initially reproducing the simple case but also included three effects not considered by Bjorkman & Cassinelli, namely; i), a finite disk correction for the radiation field, ii), an asymmetric Sobolev correction, due to the variation in velocity fields for different lines of sight, and iii), gravity darkening at the equator, due to the high rotational velocity. In the simple case Owocki et al. are able to reproduce the results of Bjorkman & Cassinelli and produce a wind compressed zone or disk depending on the rotational velocity. However, when the three processes mentioned above are included entirely the opposite effect is produced. Instead of increasing the density of the wind towards the equator rotation is found to increase the wind towards intermediate latitudes and the poles, and is much more in keeping with the bi-polar structure seen in the nebulosities around LBV's. If WR stars contain an equatorial zone or disk then there should be some indication in the line profiles. Generally WR stars do not look like Be stars; there is weak evidence for some double peaked profiles (Underhill et al. 1990, Vreux et al. 1992) but this is unusual. Models of equatorial ring-type structures with different measures of turbulence, rotation, expansion and viewing angle can reproduce the flat-topped (Underhill & Nemec 1989) and other line profiles (Rumpl 1980,

Mazzali 1990) but do not provide a unique solution to the geometry.

The other indirect line of evidence lies in the shape and structure of the nebulae surrounding WR and LBV stars. These nebulae are complex objects as they result from different episodes of mass loss and ejection through the stars' short history. The inner region of M1-67 around WR124 is axially symmetric, bipolar and clumpy, and the velocity distribution of the clumps is also axially symmetric (Nota et al. 1995). The HST images of η Carinæ and the Homunculus nebula (Hester et al. 1991) clearly show a bipolar structure and there is also evidence of a dusty disk (Hillier & Allen 1992). Coronagraphic observations of the AG Car nebula (Nota et al. 1992) and the LMC LBV R127 (Clampin et al. 1993) also show bipolar structures. Spectropolarimetry of AG Car (Schulte-Ladbeck 1993a) and R127 (Schulte-Ladbeck 1993b) indicates that the winds are asymmetric and perpendicular to the nebular lobes. The structure of these nebulae clearly indicates that there has been non-spherical mass loss and ejection from these stars which persists in the structure of the winds. However, the LBV stars and transition objects like AG Car are short-lived, violent objects so their wind structure may be more related to O stars, and is not necessarily typical of WR stars.

3.1.2 Polarisation

The best picture of the structure of WR winds currently comes from polarimetric studies. There are two ways of discriminating between intrinsic, linear polarisation and interstellar polarisation. The first is to search for temporal variability, which may be made in broad continuum bands, and the second is to use spectropolarimetry to search for polarisation across emission lines, the so-called line effect. Variability in the strength and polarisation vector has been found for many single WR stars and is found to correlate with spectral type; WN stars are more variable than WC's and the variation increases towards later subtypes. Generally the variation appears chaotic with no preferred direction, indicative of an inhomogeneous but time-averaged spherical wind. One star, WR111 (WC5), is presently known to show no intrinsic polarisation and no variability (St-Louis et al. 1987). Very few stars show a preferred

direction, and those that do also show strong variability, indicating an asymmetric as well as inhomogeneous wind. The best observed case is the possibly pathological WR6, but WR134 (HD 191765, WN6), the probably single WR136 (HD 192163, WN6) (Schulte-Ladbeck et al. 1992 loc. cit.), and the recently reclassified AG Car also show this structure (Schulte-Ladbeck et al. 1994). Surveys of WR stars indicate that the winds of single stars show four basic types of behaviour (Moffat 1996); i) smooth and spherically symmetric, e.g., WR111, ii) inhomogeneous but spherically symmetric, e.g., WR40 but most belong to this class, iii) flattened and smooth, no single stars, and iv) flattened and inhomogeneous, very few pathological cases e.g., WR6. In general the emission lines are unpolarised and come directly unscattered from the wind while the continuum is polarised.

The polarisation results show a clear progression of decreasing variation and increasing symmetry from the LBV's and transition objects through the majority of WN stars to the WC types. For most WR stars the time-averaged global structure is basically spherical but inhomogeneous.

3.1.3 Homogeneity

The polarisation measurements have already indicated that the winds of WR stars are not smooth, but there is also other evidence. High-resolution spectroscopic observations of the peaks of strong emission lines reveal a number a small, narrow features within the line. Time-series observations show that these features move coherently from the line centre to the wings, to both higher and lower velocities, where they dissipate. The process typically takes $\sim$ 12 hours and features are seen throughout the velocity range. The properties of these features were first studied using a multi-Gaussian technique (Robert et al. 1991, Robert 1992) but have since been explored using wavelet analysis (Moffat et al. 1994, Lèpine 1994), a mathematical tool for studying turbulence. Wavelet analysis is analogous to a Fourier transform in that it measures the power associated with a particular scale, in this case the velocity dispersion, σ_v, but it does not loose "positional" information, in this case the projected velocity, v_c. In this way it is possible to study the evolution of the structures in

both scale and velocity. An investigation of seven WR stars of different subtypes has shown that the intensity of the features is typically 10% of the emission line flux and between 2 and 9 features are visible at any one time. Early subtypes tend to show larger numbers of features and a larger velocity dispersion (Robert et al. 1991). The wavelet analysis has shown that the flux in each structure, $f \propto \sigma_v^2$, i.e. the brightest structures have a larger velocity dispersion, which implies they are larger, and $\sigma_v \propto v_c$ which suggests some anisotropy in the distribution of the velocity dispersion (Lèpine 1995). The spectrum of properties found for these features is taken as evidence of compressible turbulence. The moving features in the emission lines are interpreted as discrete regions of enhanced density moving in the WR wind; usually referred to as *blobs* or more recently as *clumping*. In reality the clumping is probably associated with complex shocks caused by intrinsic line-driven instabilities in the wind. The processes involved have been recently reviewed by Owocki (1991) and Owocki & Gayley (1995).

If these wind structures are also responsible for the photometric and polarimetric variability then the larger number of more diffuse features found in early subtypes should tend to smear out any variation. In contrast the smaller number of narrower features seen in later subtypes should lead to greater variation, and this is what is seen.

Other short-lived features that are seen in O-type stars are the discrete absorption-line components (DAC's) (e.g., Prinja & Howarth 1988). The behaviour of the DAC's is analogous to WR emission-line features in that they move to higher velocities but, while they are ubiquitous in O-type stars they are usually seen individually in WR winds, unlike the multiple emission-line features. So far only one WR star (WR24, HD 93131, WN6ha) is known to show DAC's (Prinja & Smith 1992).

Five WR stars surrounded by nebulae which are thought to contain stellar ejecta, WR6 (WN5, S308), WR40 (WN8, RCW58), WR75 (WN6, RCW104), WR136 (WN6, NGC6888) and WR124 (WN8, M1-67) have been studied in some detail. A bi-polar structure is frequently seen and they show differences in the ejecta, either signs of mass ejection in the form of ballistic knots or evidence of a wind-blown bubble. However, it is not clear how this relates to the structure immediately surrounding the stars.

3.2 Colliding winds

The signature of colliding winds was first recognised by Shore & Brown (1988) in the WN5+O6 binary V444 Cyg (WR139, HD 193576) but had been foreseen earlier (e.g., Prilutskii & Usov 1976, Cherepashchuk 1976) as a natural consequence of a system containing two stars with significant winds. Early analytical work (see Kallrath 1991, Usov 1995) has given way to 2D and 3D hydrodynamical modelling (Stevens et al. 1992, Walder 1995) with self-consistent cooling. The colliding winds will form two opposing shocks separated by a contact discontinuity which asymptotically tends towards a cone (Kallrath 1991). Material in the shocks will ultimately stream along the contact discontinuity away from the system. The models reveal that the shocks are very turbulent and unstable on a wide range of scales, which leads to significant structure and movement of the boundaries. Where the two winds meet between the two stars, the stagnation point, is determined by the momentum balance of the wind for, which Stevens et al. (1992) give

$$\mathcal{P} = \mathcal{R}^2 = \left(\frac{\dot{M}_{\rm WR} v_\infty({\rm WR})}{\dot{M}_{\rm O} v_\infty({\rm O})} \right) \tag{3.1}$$

and

$$\mathcal{R} = \frac{d_{\rm WR}}{d_{\rm O}} = \frac{x_0}{1 - x_0} \tag{3.2}$$

where $\dot{M}$ and v are the mass-loss rates and velocities of the two winds, $d_{\rm WR}$ and $d_{\rm O}$ are the distances of the stars from the contact discontinuity, and x_0, the stagnation point, is the distance of the contact discontinuity from the WR star, in units of orbital separation. It should be noted that Eichler & Usov (1993) use the momentum ratio in the form $\eta = \mathcal{R}^{-2}$. If v is taken as the terminal velocity then for typical values for WR and O stars the winds will meet at some balance point, but for accelerating winds the O-star wind could be overwhelmed and collapse onto the surface of the O-star. Recently the effects of the radiative pressure of the two stars have been taken into account and it has been found that the effective $\mathcal{R}$ can be significantly altered (Gayley et al. 1997), particularly in the region close to the two stars. As the O-star is usually much more luminous that the WR component the effect of radiation is to move the contact discontinuity away from the O-star, and prevents the O-star wind from collapsing. The size of the regions occupied by the two winds is also largely

dependent on $\mathcal{R}$. The opening angle of the cone defining the contact discontinuity is typically 40° (see Figure 5.3). The shocks lie at some distance on either side of the contact discontinuity and also show considerable movement, which leads to the definition of a "shock zone" covering these regions. The size of the zone, in angular terms, is large, but poorly defined (see Stevens et al. 1992, Stevens et al. 1996). In most of the calculations the orbital motion of the stars is ignored as it is small relative to the wind velocities, but it may be included approximately by tilting the axis of the contact-discontinuity cone by a small angle. At large distances the shock zone will become curved and wound around the system (see Walder 1995).

One of the consequences of shocks caused by colliding winds is the production of X-rays which are observed to be stronger in binaries than single stars (§ 2.6). Within the WR wind the X-rays are strongly absorbed and act much like a source of ionizating radiation. The effect on the structure of the WR wind is not clear but in their model of high-mass X-ray binaries Hatchett & McCray (1977) suggested that a large ionized void would be created. In colliding-wind binaries the X-ray flux is lower than in HMXB's and the effect is likely to be more localised to the shock zone (Stevens 1993). The effect of the increased ionization will be to increase the line emission from the shock zone and is discussed in more detail in § 4.2.

3.3 Ionization structure

Firstly Beals (1929) and later Kuhi (1973) showed a correlation between ionization potential (IP) and line width which showed that lines from ions with higher IP were narrower and therefore formed deeper in the wind. Willis (1982) argued for a correlation between excitation potential (EP) and line width but using the standard model Hillier (1989) demonstrated that the principal relationship is between IP and line width, but that there is a secondary relationship with EP. Further observational evidence of a velocity dependence on EP is given by Niedzielski (1994) for He II lines in 5 WN stars. Within the zone of formation of the He II lines, which according to the models of Hillier (1987) is quite extended, there is clearly an increase in velocity with decreasing EP. For some lines the relationship is not linear but switches on at a

particular velocity, suggesting that there may be optical-depth effects. Using a larger sample of stars, 5 WN and 3 WC, and a larger selection of ions and lines, Dalton et al. (1995) also find stratification within each ionization stage as well as the familiar dependence on IP. The more recent work by Rochowicz (1996) extends these results to 21 Galactic and LMC WN stars. Recently Schulte-Ladbeck et al. (1995, 1996) have found that the gradient of the ionization stratification in WN stars, as measured from the emission line widths, is correlated with the wind performance number.

3.4 Velocity law

The form of the velocity law originates with the CAK models of wind acceleration,

$$v = v_\infty \left(1 - \frac{R_\star}{r}\right)^\beta \tag{3.3}$$

and is widely used. From analytical arguments CAK found a value of $\beta = 0.5$ and this was initially found to be consistent with the observed Hα profiles of O-type stars although different results can be found for the same star. Olson & Ebbets (1981) found it necessary to use a range of velocity laws with β from $\sim 1 - 2$. More recently Puls et al. (1996) using an improved NLTE code to model Hα profiles for a large sample of O stars find a typical value of $\beta \simeq 1$. Using lines in the UV range Howarth (e.g., 1984) finds similar values.

The beta law appropriate for O stars is also generally applied to WR stars. However, as part of the wavelet analysis of the moving features found in WR emission lines it has been possible to estimate the acceleration of the blobs. Their velocities require a much slower velocity law with $\beta \sim 10 - 15$ (e.g., Moffat & Robert 1991). In O stars Prinja (1992) found the DAC's also accelerate slowly, corresponding to $\beta \sim 2 - 5$.

In an attempt to derive the velocity law Moffat (1996) has shown that by assuming a constant acceleration consistent with the observations the velocity is approximated by the beta law with $\beta \simeq 10$. Using a specialised hydrodynamic, line-blanketed, NLTE code with photon loss, Schmutz (1997) has derived the velocity law in a semi-self consistent way from the He Iλ10830 line in WR6. For the outer regions where this line is particularly sensitive $\beta \sim 3$ or possibly as large as 8 depending on the hydrostatic

radius of the star. However, in general the acceleration was not well represented by the usual velocity law. A similar conclusion has been drawn by Springman & Puls (1998) from work on the multiple-scattering problem. They finds it necessary to have $\beta \sim 0.6$ initially rising to $\beta > 1$ at large r.

3.5 Terminal velocity v_∞

The terminal velocity v_∞ of the wind used to be determined from the extreme blue edge of the P Cygni absorption component in the UV resonance lines (referred to as $v_{\rm max}$ or more generally, $v_{\rm edge}$). It was also inferred from the run of widths of the optical emission lines as a function of ionization potential, extrapolated to zero volts (Conti et al. 1983, Torres et al. 1986), and the results were consistent for stars studied in both ways. Williams & Eenens (1989) measured the P Cygni absorption velocities of the He I 2.058 μm line in 8 WR stars and found terminal velocities typically 0.7 of those determined previously. As this He I line is formed in the asymptotic part of the wind it should give a reliable indication of v_∞. In γ^2 Vel the velocity is 1500 km s^{-1} compared to 2000 km s^{-1} determined from $v_{\rm edge}$ of the UV P Cygni profiles. Also in the infrared an analysis of the [Ne II] 12.8 μm line in γ^2 Vel (Barlow et al. 1988) gives $v_\infty = 1520$ km s^{-1}, consistent with the He I velocity. The [Ne II] line gives a rectangular profile consistent with an optically thin line of constant velocity formed at large radii and provides independent confirmation of the He I velocity.

Prinja et al. (1990) have re-evaluated the UV P Cygni absorption velocities for 34 WR and O stars and argue that the blue edge of the saturated part of the absorption profile ($v_{\rm black}$) provides a better estimate of v_∞ than the previous methods. Terminal velocities determined in this way are typically 0.75 of those found from $v_{\rm edge}$ and are consistent with the infrared He I and Ne II results. The additional velocity between $v_{\rm black}$ and $v_{\rm edge}$ is attributed to turbulent motions in the wind associated with the line-driven instabilities.

3.6 Mass loss

Mass-loss rates are derived by a variety of methods each with their own assumptions and model dependencies. Comprehensive reviews of the procedures are provided by Willis (1991b), Abbott et al. (1986) and Barlow (1982). Mass-loss rates may be derived from thermal radio emission which is assumed to arise from free-free emission in the outermost parts of the wind, where the terminal velocity has been reached. In a spherically symmetric wind the mass-loss rate may be derived from the formula given by Wright & Barlow (1975)

$$\dot{M} = 0.095 v_\infty \left(\frac{S_\nu^{0.75} D^{1.5}}{(g\nu)^{0.5}}\right)\left(\frac{\mu}{Z\gamma^{0.5}}\right)$$

where S_ν is the radio flux in Jy at frequency ν in Hz; v_∞ in km s^{-1}; D is the distance in kpc; g is the gaunt factor; μ, Z and γ are respectively the mean molecular weight, rms ionic charge and mean number of electrons per ion. In the radio region the thermal free-free emission is predicted to have a spectral index, $\alpha = 0.6$, where $S_\nu = \nu^\alpha$, for an homogeneous, isothermal, spherically expanding wind with $\rho(r) \propto r^{-2}$ (Wright & Barlow 1975). The departure of α from 2/3 is due to the frequency dependence of the gaunt factor. Altenhoff et al. (1994) observed 11 WR stars between 1.2 mm and 6 cm and found $\alpha = 0.82 \pm 0.09$, with a weak dependence on $T_{\rm eff}$ for the WN stars. The higher spectral index may indicate a variation in $T_{\rm eff}(r)$ or recombination at very large distances, both of which are at odds with the assumptions. Another difficulty lies in the determination of v_∞ which, although now believed to be understood, has led to a rescaling of mass-loss rates. Another area of contention in the radio mass-loss determinations is in the factor $C = \frac{\mu}{Z\gamma^{0.5}}$ from the expression above, for WC stars. Van der Hucht et al. (1986) included the effects of high C abundance from the evolutionary models and proposed an upward revision of the mass-loss rates for WC stars by a factor of 2 – 3. It is now believed that the dominant ion in both WN and WC stars in the radio region is He^+ and for WC stars the ionization balance of C suggests C^{2+} is the dominant species. Based on these revisions Willis (1991) summarises the mass-loss rates at between 10^{-4} and 10^{-5} $M_\odot$ yr^{-1} for WN and WC stars. Finally there is the assumption that the wind is homogeneous. WR winds show clear evidence of clumping which will lead to overestimates of the mass-loss rates

from radio fluxes. The size of the overestimation depends on the clumping density spectrum but the current estimates are a factor of ~ 2 (see Williams 1996, Schaerer 1995). Interestingly, for γ^2 Vel the recent radio determination of $\dot{M}$ is consistent with the distance-independent value derived from fitting X-ray spectra using a colliding-wind model (Stevens et al. 1996, § 7.6), which weakens the need for any correction due to clumping.

Mass-loss rates are also derived from modelling optical and UV, and as seen above, X-ray spectra, and may also be obtained from polarization variations (St-Louis et al. 1988). The agreement between the best estimates is typically a factor of ~ 5. With such wide margins limits on mass-loss variability are poor but evidence from free-free emission fluxes at radio and infrared wavelengths suggests they are generally stable from months to years (see Williams 1996).

3.7 Variability

Wolf-Rayet stars are basically quite stable on time scales of years but have shown an increasing repertoire of low-amplitude variations, mainly on short time scales, in flux and polarisation of continuum and emission lines, and in velocity and line profiles. At the time of the first review of WR variability (Vreux 1987) variations were generally viewed in terms of either pulsation or a binary hypothesis of a Wolf-Rayet plus a compact companion. The WR+c systems were proposed in the evolutionary scenario of van den Heuvel (1976) which may be illustrated schematically as

O+O $\Rightarrow$ WR+O $\Rightarrow$ SN $\Rightarrow$ c+O $\Rightarrow$ c+WR $\Rightarrow$ compact+compact

Moffat (1982) presented a list of 11 stars, for which periods had been found in the velocity variations, as WR+c candidates. Most of the periods have since undergone some revision or have failed the test of time completely. One of the WR+c candidates, WR6, is special case. Variations with a period of 3.76 days in the line profiles, velocity, light, X-rays and polarisation described by Firmani et al. (1980) have persisted and are still found in the light (Antokhin et al. 1994a) and UV spectral variations (Lloyd

& Stickland 1994), St-Louis et al. 1995) but are now thought to be due to rotation and the passage of clumps through the wind.

Variation in the continuum flux and line profiles of apparently single Wolf-Rayet stars have been recognised for some time. Photometric observations of several stars, WR24 (WN7+abs), WR25 (WN7+abs), WR78 (WN7), WR108 (Ofpe/WN9) (Gosset et al. 1994) and WR82 (WN8) (Antokhin et al. 1994b) show apparently random variations of < 0.1 mag but clearly above the observational noise. Variations of similar amplitude on a time scale of hours have been seen in WR46 (WN3p), WR50 (WC6) WR86 (WC7) (van Genderen et al. 1990). The subject of variation has been reviewed by Moffat & Robert (1991) and Antokhin (1996).

O-star micro-variability is small but largely uncharted territory. In a review of O-star photospheric variability Fullerton (1994) found no evidence of pulsation in early O-type stars although there is clearly wind variability (e.g., Kaper & Henrichs 1994, Harries & Howarth 1996, Reid & Howarth 1996) which is linked to rotation (e.g., Massa et al. 1995, Howarth et al. 1995).

Chapter 4

Phase-dependent variations

4.1 Selective absorption

The first phase-dependent line-profile variations seen in WR+O binaries were in UV spectra of γ^2 Vel taken with the S2/68 experiment on the TD1-A satellite (Willis & Wilson 1976). Spectra with the O-type star near superior and inferior conjunction show dramatic differences in the Si IV λ1400 and C IV λ1548, λ1550 resonance lines and in the subordinate C III λ2297 line. At superior conjunction, i.e. when the O star is behind the WR star, the emission lines are considerably weakened or absent. Observations at the same phase with other experiments confirm that this is a phase-dependent effect. Further observations with the Copernicus satellite (Willis et al. 1979) which cover a wider wavelength range at higher resolution, show variation in many resonance and low-excitation lines. Higher-excitation lines such as C IV λ2405, λ2530 show no such variation with phase.

The variations were interpreted by Willis & Wilson (1976) as being due to the eclipse of the O-type star by the Wolf-Rayet wind. At superior conjunction the continuum of the O star will be preferentially absorbed by the ions responsible for the emission lines across the whole velocity range of the wind. The lines that show the greatest variation will be those which arise in levels with relatively high populations, that is, resonance and low-excitation lines, (semi) forbidden lines (under the right circumstances) and, perhaps less obviously, lines in which the lower level is coupled with an optically thick

resonance transition. These lines behave much like resonance lines e.g., N IV λ1718 and C III λ2297, which are prominent features of WN and WC stars respectively. The profile of the selective absorption will depend on the velocity and ionization structure of the wind and may be used as a probe to study the wind itself. The inclination of the system will also have a large effect. If it is low the O star will be absorbed, but there will be little variation in the depth of wind that the O-star continuum passes through. However, if it is high then the change in depth of the wind the O-star continuum passes through will be large, and at superior conjunction the line of sight will pass close to the WR star, sampling a large range of radii. More recent observations of WR + O binaries with *IUE* have confirmed and developed the findings of the earlier work (e.g., Koenigsberger 1990, St-Louis et al. 1993).

The first attempts to use the effects of the selective absorption by the wind as a diagnostic were made by Willis et al. (1979) and Howarth et al. (1982). A simple estimate of the change in the absorbing column between superior and inferior conjunction was combined with the observed change in equivalent width of the line to constrain the mass-loss rate. The column is estimated by integrating the density along the line of sight to the O star, and this may be done analytically by assuming a constant wind velocity and a constant fraction of absorbing ions. The equivalent width of the selective absorption is then calculated from

$$\frac{W_\lambda}{\lambda} \leq \frac{\pi e^2}{mc^2} N_a f \lambda$$

in which the equality holds if the line is unsaturated.

Stickland et al. (1986) generalised this approach to deal with all phases and further introduced a shell structure which enabled the radial dependence of absorbers to be varied, while maintaining a constant velocity. Using low-resolution *IUE* spectra and optical data for CV Ser they found it difficult to fit both the C III] λ 1909 and the C III/C IV λ 4650 equivalent widths simultaneously. Individual lines posed less of a problem and the qualitative agreement with the observations was good.

Koenigsberger & Auer (1985) have studied the variations of six WN binaries at low resolution with *IUE* and found variations common to all the systems. The P-Cygni structure of the N IV λ1718 line changes from a strong emission with weak or absent

absorption to broad and deep absorption with weak or absent emission. The behaviour of C IV λ1550 is similar although the suppression of the emission component is not as great and the absorption component is narrower than λ1718. The He II λ1640 emission line develops a small P-Cygni absorption near superior conjunction. Variations in the line strengths occur smoothly with orbital phase and are remarkably consistent from star to star. For the N IV λ1718 line Koenigsberger & Auer (1985) find that for $r > 14R_\odot$ the optical depth $\tau \propto r^{-1}$ and that the ionization stage of N IV continues to $r \sim 60R_\odot$. Using an early version of the model described in Chapter 5, Lloyd & Stickland (1995b) modelled the equivalent width variations of the N IV λ1718 line in the WN4+O5 binary HD 90657. The density of N IV was found to vary as $\propto r^{-1}$ or r^{-2} and continued to absorb at $r > 60$ $R_\odot$. Castor & van Blerkom (1970) find the He II emitting region extends to $r \sim 70R_\odot$ and as the ionization potentials are very different it provides further confirmation that ions with different ionization potentials can co-exist (Willis 1982, see § 3.3).

As well as the lines the apparent continuum short-ward of $\sim$ 1500Å also shows variation similar in scale to the N IV λ1718 variation (Koenigsberger & Auer 1985). In extreme cases the intensity can fall by $\sim$45% near superior conjunction while longer wavelengths (1500 – 3300Å) are unchanged (Hutchings & Massey 1983). Koenigsberger & Auer (1985) suggested that these variations are due to a pseudo-continuum formed by a large concentration of Fe V and Fe VI lines. In particular Fe V has 236 lines in the range 1300–1500Å but only 78 weak lines in the range 1500 – 1700Å. Also Fe V has the same ionization potential as N IV. In an analysis of high-resolution spectra of γ^2 Vel, V444 Cyg and CV Ser St-Louis et al. (1993) constructed an empirical model of the pseudo-continuum of Fe V lines which provided a good fit to the observations

Observations of the SMC binaries HD 5980 (WN4+O7), Sk188 (WO4+O4V) and Sk108 (Koenigsberger et al. 1987, Koenigsberger et al. 1988) find variations of N IV λ1718 similar to galactic WR stars but there is no significant variation of the Fe V $\lambda\lambda$1350 – 1490Å pseudo-continuum. The absence of this variation is interpreted as being due to the abundance differences between galactic and SMC stars and an estimate of the Fe/N ratio is consistent with other determinations.

Auer & Koenigsberger (1994) have developed a model for calculating the absorption variation using a Monte Carlo technique. They have shown that a variety of profiles are possible depending on the velocity law, and where the line is formed. When applied to the variations of the N IV λ1718 line in V444 Cyg the model provided an adequate fit, but they were unable to recover information on the velocity law as the line was saturated. Auer & Koenigsberger found differences between what was observed and the modelled profiles which they suggested might be due to the effects of colliding winds. Stevens (1993) calculated the line profiles assuming resonant scattering and included the effects of the O-star wind. When applied to V444 Cyg the results for the N IV λ1718 line are in good general agreement with observation; the reduction in absorption and increase in emission at inferior conjunction, and the visibility of the O star.

4.2 Colliding winds

In WR+O binaries both components have strong winds. The terminal velocities of O stars in general are slightly larger than that of WR stars, typically 1500 – 3000 $\mathrm{km\,s^{-1}}$ as opposed to 1500 – 2500 $\mathrm{km\,s^{-1}}$ (Prinja et al. 1990), but the mass-loss rates of WR stars are typically 10 times those O stars. Prilutskii & Usov (1976) and Cherepashchuk (1976) initially proposed that the collision of supersonic winds in hot binaries should produce large amounts of X-ray-temperature gas. WR+O binaries are in fact relatively weak X-ray sources but are on average a few times brighter than single stars, and Pollock (1987) suggested that this was due to colliding winds (see § 2.6). A similar picture has also been found for O stars (Chlebowski & Garmany 1991). Evidence of wind-wind collisions was seen by Koenigsberger & Auer (1985) in the *IUE* spectra of 3 WN binaries. When the O star is in front the wind shows a larger terminal velocity due to the O star dominating that part of the wind. In a detailed analysis of V444 Cyg, Shore & Brown (1988), found a cavity in the WR wind where it sweeps around the O star. The cavity occupies only a small range of phases near inferior conjunction and is also associated with the highest terminal velocities. St-Louis et al. (1993) also found evidence of wind collisions in γ^2 Vel. The terminal

velocities of the WR and O components could be identified and the phase-dependent variations were consistent with the line of sight passing through the O-star wind at inferior conjunction.

Another effect of the colliding winds on the spectra seems to have been first discussed by Neutsch et al. (1981). They found the C III λ5696 emission line in HD 152270 to have a broad absorption, creating two emission peaks which varied in velocity with phase. Using a Monte Carlo technique they were able to describe the variations in terms of excess emission from the shock zone and included the lack of the usual WR emission from the O-star cavity. The method has recently been revived by Lührs (1997), who has taken advantage of recent developments on colliding winds to re-examine the variations in HD 152270. The double peaked structure seen by Lührs and other asymmetric features have been simulated in 'generic' models of emission line variation in Symbiotic stars by Nussbaumer & Walder (1993). St-Louis et al. (1996) have observed similar variations in seven WR+O systems but have been able to find a satisfactory fit with the model for HD 152270 only.

Chapter 5

The absorption-line model

The observed flux is usually assumed to comprise three components (see Figure 5.1), i) the WR emission and P-Cygni spectrum as in a single WR star, $F_\nu(\mathrm{WR})$, ii) the O-star flux $F_\nu(\mathrm{O})$, which is strongly modulated by a phase-dependent absorption function, $A_\nu(\phi)$, and iii) the flux in the WR wind occulted by the O-star, which is also a function of phase, $F_\nu(\phi)(\mathrm{OCC})$, giving the observed flux,

$$F_\nu = F_\nu(\mathrm{WR}) + F_\nu(\mathrm{O})\, A_\nu(\phi) - F_\nu(\phi)(\mathrm{OCC}) \tag{5.1}$$

To calculate the first term, the WR flux, requires the most modern spherical, line-blanketed NLTE models, and is not the aim here. The philosophy behind the model is to use the *difference* in the observed profiles to probe the wind. The first term is complicated, but it is assumed to be constant, and therefore plays no rôle in the observed variation. The second term, in particular the variable absorption function, $A_\nu(\phi)$, is the subject of the model. Finally, the third term also requires detailed models in order to calculate it, but even in short-period systems the effects are expected to be small (Auer & Koenigsberger 1994).

In the model described here the simplicity of a pure absorption scheme is retained but a more sophisticated approach enable a velocity law to be used, a variation in the radial concentration of absorbers, and line profiles to be calculated. The full model is also able to take into account the cavity in the WR wind created by the O-star wind, and the effects of the shock zone.

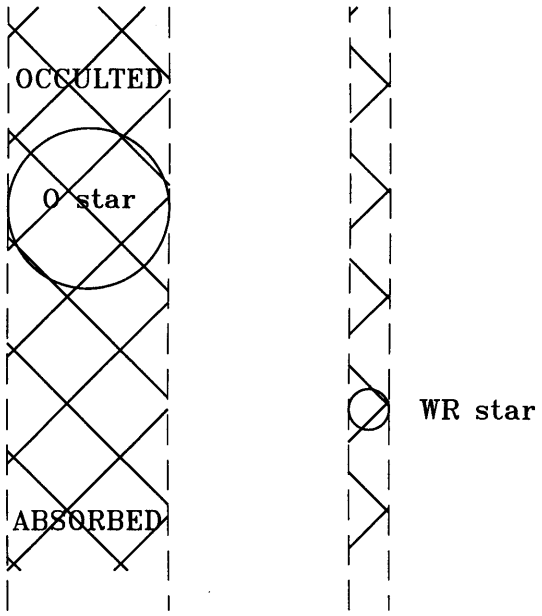

Figure 5.1: The WR wind showing the occulted and absorbed regions (*hatched*) for the O star and the WR component. For the WR star these regions are effectively constant but for the O-star are a strong function of phase. The system viewed perpendicular to the line of sight with the observer towards the bottom of the page.

5.1 Geometry

In a binary system the separation of the two stars is given by

$$r = a_0(1 - e\cos E)$$

where a_0 is the length of major axis, e is the eccentricity and E is the eccentric anomaly. E is determined by iteration from the solution of Kepler's law

$$E = Me\sin E$$

where M is the mean anomaly and related to the phase from periastron by

$$M = 2\pi\phi$$

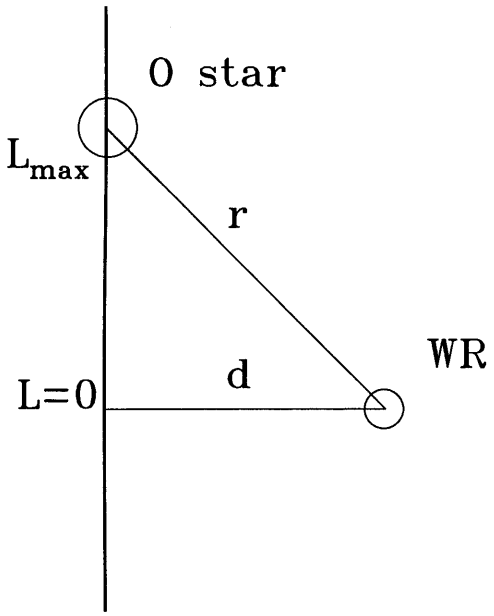

Figure 5.2: The system viewed perpendicular to the line of sight with the observer towards the bottom of the page, showing the relationship between r and d, and L_{max}.

The eccentric anomaly, ν, is related to E through

$$\tan\frac{\nu}{2} = \sqrt{\frac{1+e}{1-e}}\tan\frac{E}{2}$$

The other geometric parameters of a spectroscopic binary orbit are ω, the argument of the perihelion and i, the orbital inclination.

For an observed phase at time t, $\phi = (t - T_0)/P$, where T_0 is the time of periastron passage and P is the period, these relationships are used to solve for ν. In circular orbits $\nu = \phi$ but in eccentric orbits this relationship is non-linear. It should also be pointed out that photometric phases will also used later in the discussion of HD 152270. Photometric phase zero is defined as the time of superior conjunction of the O star, i.e. when it is behind the WR star.

A line of sight passing through the system to the O-type star defines the L axis (see Figure 5.2). The observer lies at $L = -\infty$; $L = 0$ is defined as the plane of the sky

passing through the WR star and the position of the O star is given by

$$L_{max} = r \sin(\nu + \omega) \sin i \tag{5.2}$$

The minimum distance of the L-axis from the WR star, the impact parameter, is given by

$$d = r(\cos^2(\nu + \omega) + \sin^2(\nu + \omega) \cos^2 i)^{1/2} \tag{5.3}$$

At each orbital phase a grid of points is created along the line of sight to the O star (L-grid). In theory these should run from $-\infty$ to L_{max} but in practice $-\infty$ is replaced with a suitably large negative value, typically $5000\mathrm{R}_\odot$.

5.2 Shock zone

The mutual interaction of the WR and O-star winds has a significant effect on the geometry of the winds. As described earlier (§ 3.2) a variable, turbulent shock zone is formed at the interface between the two winds which will have very different properties to the undisturbed winds. In the model three zones are defined, the WR wind, the shock zone and the O-star wind. For simplicity the boundary between each wind and the shock zone is treated as a cone following the approximations of Kallrath (1991) and Usov (1995). If the momentum balance

$$\mathcal{R} = \left(\frac{\dot{M}_{\mathrm{WR}} v_\infty(\mathrm{WR})}{\dot{M}_{\mathrm{O}} v_\infty(\mathrm{O})} \right)^{1/2} = \frac{x_0}{1 - x_0} \tag{5.4}$$

then the centre of the shock zone, the contact discontinuity has an opening angle θ, where

$$\theta \simeq 120 \left(1 - \frac{\mathcal{R}^{-\frac{4}{5}}}{4} \right) \mathcal{R}^{-\frac{2}{3}} \quad degrees \tag{5.5}$$

from the cone axis The thickness of the zone is also taken as θ. In theory $\Delta\theta$ should be $< 0.5\theta$ for short period systems (Usov 1995) but the turbulence revealed by the hydrodynamical calculations suggests that $\Delta\theta \sim 0.5\theta$ is not a bad choice. In the region

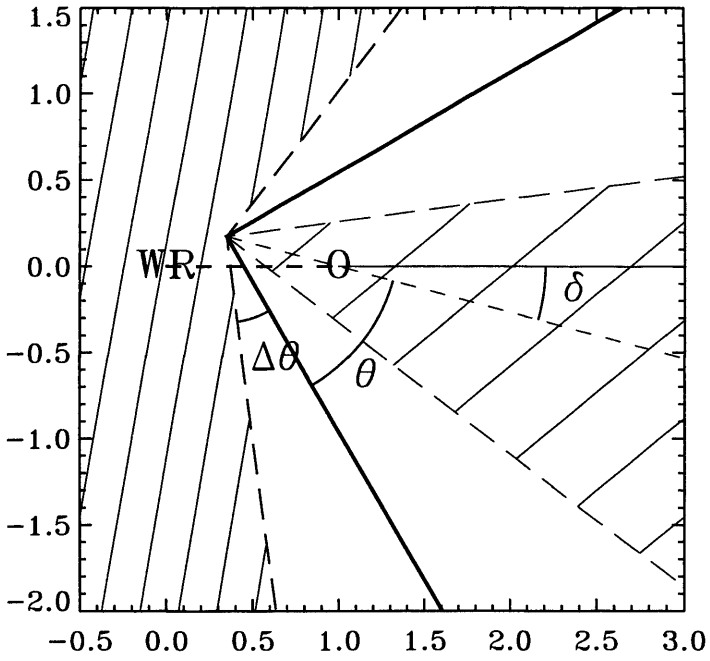

Figure 5.3: The geometry of the shock zone in the plane of the orbit. The units are orbital separation. The positions of the WR and O stars are indicated at either end of the major axis (*thick dashed line*). The thick solid line indicates the position of the contact discontinuity, and the opening angle, θ, offset angle, δ, and half width of the shock zone, $\Delta\theta$ are indicated. The regions of the undisturbed WR and O-star winds are also indicated (*hatched areas*).

close to the O star the contact discontinuity will be approximately hemispherical but as this region is not important to the discussion here, this additional complication has not been implemented. At intermediate distances, out to $r \sim v_{WR\infty}P/2$, from the O star, the contact discontinuity approaches the conic while at larger distances the effect of orbital rotation begins to dominate and the contact discontinuity takes on a spiral structure. Such a complex structure is difficult to model simply; however, as the region of interest lies mostly at intermediate radii the contact discontinuity may be approximated by a cone, offset from the line between the two stars, by an angle

$$\delta \simeq \tan^{-1}\left(\frac{v_{orb}}{v_\infty(\mathrm{WR})}\right) \tag{5.6}$$

in the orbital plane of the binary. The apex of the cone lies at a distance of

$$d_{apex} = ax_0$$

from the O star (Kallrath 1991), where a is the orbital separation and x_0 is the stagnation point. as defined in Eqn. 5.4. The geometry of the shock zone is shown in Figure 5.3. The thick solid line indicates the position of the contact discontinuity, which has an opening angle, θ, measured from the axis of the cone. The axis of the cone is offset by an angle, δ, from the line of the major axis by orbital motion. The edge of the shock zone is an angle $\Delta\theta$ on either side of the contact discontinuity, which defines the regions of the undisturbed WR and O-star winds (*hatched areas*).

The initial values of θ, δ and x_0 are calculated using the available information but all are treated as variable parameters in the model. When the L-grid is constructed each point is associated with one of the three zones and the velocity and density are calculated appropriately. In the shock zone the velocity is taken as the WR-wind velocity at that radius but the direction of flow is taken as parallel to the contact discontinuity. The density in the shock zone *may* be calculated from the degree of compression of the WR and O-star winds. However, as the temperature and ionization may be very different to the undisturbed winds the density is not a reliable indicator of the number of absorbing ions responsible for a particular line. To handle this position simply, the effective density in the compression zone is treated as a variable factor of the WR-wind density at that radius.

5.3 Density of absorbers

From considerations of mass continuity the density in the wind as a function of radius is given by

$$\rho(r) = \frac{\dot{M}}{4\pi r^2 v(r)}$$

where the mass-loss rate, $\dot{M}$, is assumed to be spherically symmetric and constant, and $v(r)$ is the velocity of the wind is given by the standard velocity law

$$v(r) = v_\infty(1 - \frac{R_\star}{r})^\beta$$

where v_∞ is the terminal velocity of the wind, $R_\star$ is the stellar radius and β is the acceleration parameter.

The number density of atoms of a particular element, z, at r, using the density appropriate for the zone, is given by

$$N_z = \frac{\rho(r) f_z}{A_z m_H}$$

where A_z is the atomic weight and f_z is the relative abundance of the element by mass. The number density of absorbing ions

$$N_a = N_z f_j f_i$$

where f_j and f_i are the fraction of atoms in the relevant stage of ionization and level of excitation respectively. In the model there are two different ways of handling the variation in density of absorbing ions with radius. In the first and simplest case f_i may be fixed at an arbitrary value throughout the wind and f_j may be varied with r by a simple power law

$$\log f_j = \alpha \log r + const$$

such that $0 \leq f_j \leq 1$. Although f_i in reality will not be constant this simple arrangement enables the product $f_j f_i$ to be modelled. In the second case the variation of electron temperature with radius is specified and f_i and f_j are calculated using the Boltzmann distribution and the Saha ionization equation, assuming LTE. Although the winds are not in LTE this approach does allow the rise and fall of different ionization stages to be calculated in a more flexible and possibly more physically meaningful way. After some experimentation it was decided to define the temperature T_e through a power-law like expression which gives a suitably slow decline at large r.

$$\log(T_e - T_a) = \log T_1 + A_T \log r$$

where T_1 is a constant, A_T is the gradient and T_a is an asymptotic value at large r. The template for the run of electron density N_e and the helium ionization balance with radius broadly follows the WC models of Hillier (1989) and Hamann et al. (1992). The electron density is derived assuming that the wind is composed entirely of helium, according to the prescription

$$N_e = 2N_{He^{2+}} + N_{He^{+}}$$

which is solved iteratively with the Saha ionization equation

$$\log \frac{N_k N_e}{N_j} = -\chi_{j,k}\Theta - \frac{3}{2}\log\Theta + 20.9366 + \log\frac{2U_k}{U_j}$$

for all three helium ionization stages. Here the subscripts j and k refer to successive stages of ionization, $\chi_{j,k}$ is the ionization potential from j to k, Θ is $5040/T_e$, N_j, N_k and N_e are the number density of ions, j and k, and electrons, and U_j and U_k are the partition functions. As a first approximation U_j is taken as the statistical weight of the ground level, $g_{0,j}$, and its dependence on T ignored (Mihalas 1978). When N_e has been determined the Saha ionization equation is applied repeatedly to calculate the ionization balance for the element responsible for the line of interest, and finally the fraction in the particular stage of ionization, f_j, is calculated. The fraction of ions, j, in a particular level of excitation, i, is calculated from the Boltzmann distribution

$$f_i = \frac{N_i}{N_j} = \frac{g_i}{U_j} e^{-\chi_i/kT_e}$$

where χ_i is the excitation potential of level i, g_i is the statistical weight of level i and again $U_j = g_{0,j}$.

At each orbital phase the density in the wind is calculated at each of the L-grid positions.

5.4 Doppler broadening

The absorbing ions have a velocity ξ_0, as given by the velocity law and will have an intrinsic velocity dispersion, which is assumed to be similar to a thermal distribution.

Following Mihalas (1987), for a Maxwellian distribution velocity distribution of ions where the ξ_0/c is small, the total absorption coefficient at frequency ν is given by

$$\alpha_\nu = \frac{\sqrt{\pi}e^2}{mc} f \frac{1}{\pi} \int_{-\infty}^{\infty} \frac{(\Gamma/4\pi)\exp(-\xi^2/\xi_0^2)}{(\nu - \nu_0 - \xi\nu_0/c)^2 + (\Gamma/4\pi)^2} \frac{d\xi}{\xi_0}$$

The Doppler width of the line is defined as

$$\Delta\nu_D = \frac{\xi_0\nu_0}{c}$$

and the Doppler shift due to velocity ξ is

$$\Delta\nu = \frac{\xi\nu}{c}$$

Defining

$$v = \frac{\nu - \nu_D}{\Delta\nu_D} \qquad y = \frac{\Delta\nu}{\Delta\nu_D} = \frac{\xi}{\xi_0} \quad \text{and} \quad a = \frac{\Gamma}{4\pi\Delta\nu_D}$$

then the absorption coefficient may be rewritten as

$$\alpha_\nu = \frac{\sqrt{\pi}e^2}{mc} f \frac{H(a,v)}{\Delta\nu_D}$$

where

$$H(a,v) = \frac{a}{\pi} \int_{-\infty}^{\infty} \frac{\exp(-y)^2 dy}{(v-y)^2 + a^2}$$

is the Voigt function. For the line of interest the opacity of the transition is is given by

$$l = \frac{\pi e^2}{mc} f N_a$$

Where N_a is the density of absorbing ions. If the line has a Voigt profile then

$$l_\nu = \alpha_\nu N_a = \frac{l}{\sqrt{\pi}\Delta\nu_D} H(a,v).$$

The optical depth at each point in the line is the integral of the absorbing column

$$\tau_\nu = \int_{-\infty}^{L_{max}} l_\nu \, dL$$

and the intensity profile is simply

$$I_\nu = I_0 e^{-\tau}$$

The number density of absorbers, and hence the line absorption, is calculated on a wavelength grid which covers the line or spectral region of interest for each of the L-grid points. The optical depth is then calculated at each λ-grid point by numerically integrating along the line of sight to the O star. Finally the intensity in the line is calculated from the optical depth.

5.5 Assumptions

The basic assumptions in Eqn 5.1 are that the WR and O-star fluxes are constant. The O star is treated as a point so any effects of gradients across the surface of the O star are ignored. It is also implicitly assumed that the form of the velocity law is correct. The WR and O-star winds are initially assumed to be spherically symmetric and smooth see § 3.1. Following the earlier discussion the undisturbed wind is likely to be spherically symmetric on the average and there should be no large systematic asymmetry intrinsic to the winds. The most dramatic asymmetry is caused by the wind interaction and this is handled through the shock zone. The short-lived coherent features which move through the emission lines are attributed to blobs of material in the wind. Also the boundary of the wind shock zone is uneven and variable. The moving features in the emission lines are relatively small, $\sim$ 10%, and will be lost in the absorption lines. In the context of the model they will not be significant. They may contribute to the noise of individual spectra but should average out. The mass-loss rate is assumed to be constant and smooth.

It is assumed that the continuum light of the WR and O star is constant and in both cases this is probably sufficiently true. WR continuum light variations are small, typically $<$ 10% for WN stars and less for WC's.

5.6 Areas of uncertainty

The physical parameters of the binary orbits are generally known to a greater or lesser degree. The period, velocity amplitudes and eccentricity can be measured. The inclination can be determined from polarization measurements, although some assumptions are required. The mass-loss rates and terminal velocities of the WR component may be measured and depending on the circumstances the terminal velocity of the O star may also be measured, but its mass-loss rate has to be assumed. These quantities determine the opening angle of the contact discontinuity which must be regarded as the least secure parameter.

5.7 Examples

In this section the model will be used to show the general behaviour of the line profiles produced by the selective absorption of the O-star continuum for differing orbital inclinations, wind velocity laws and radial variation of absorbing ions. Initially the WR wind will be considered alone, then the cavity in the WR wind created by the O star will be introduced, and finally the full effect of the shock zone will be shown.

5.7.1 WR wind

In the first set of examples the profiles are calculated at photometric phase zero (superior conjunction of the O star) where the absorption is at a maximum, and phases $\phi = 0.1$, 0.25 (quadrature) and 0.5 (inferior conjunction) where the absorption is at a minimum. The mass-loss rate, abundance and atomic parameters have been adjusted so that the maximum absorption just reaches saturation. The size of the system, $a_0 \sin i = 35 R_\odot$, is similar to WR79, the velocity law $\beta = 1$ and the fraction of absorbing ions f_j is constant through the wind. The profiles have been calculated for inclinations $i = 80°$, $60°$ and $40°$ and are shown in Figure 5.4. At phase zero the absorption covers most of the velocity range of the wind as the O star is at some distance beyond the WR star. As the phase increases two effects take place.

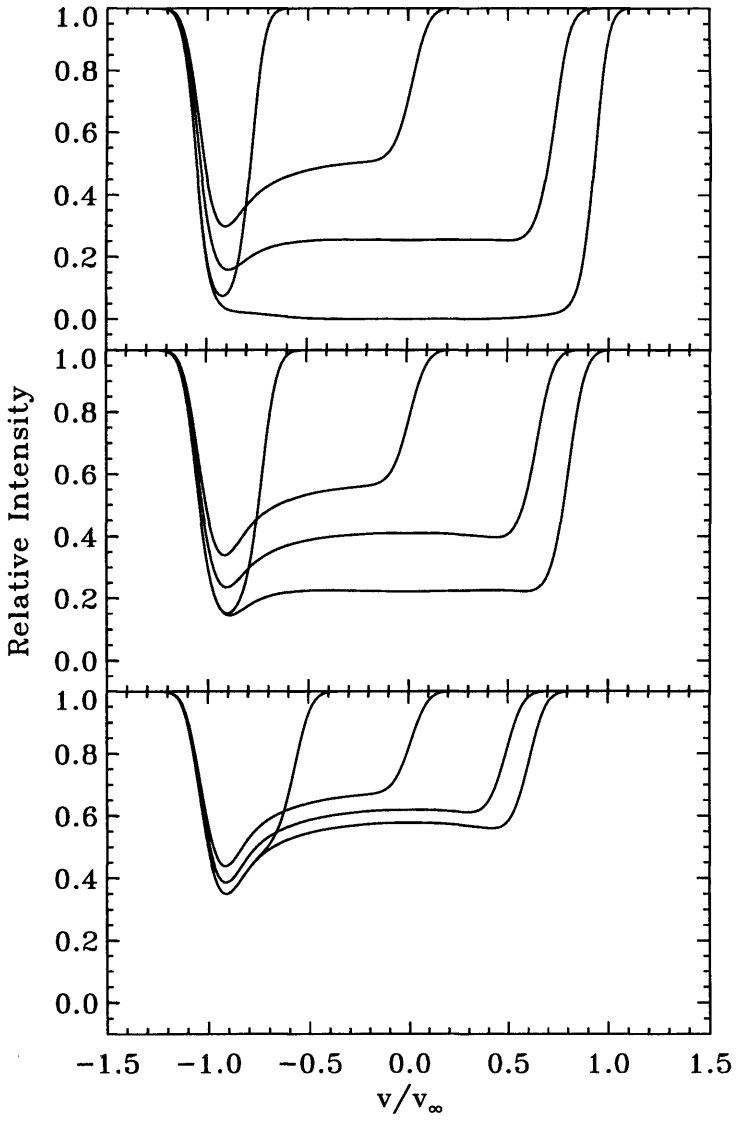

Figure 5.4: Profiles showing the change in the selective absorption at phases 0.0, 0.1, 0.25 and 0.5 for inclinations of 80° (top), 60° and 40° (bottom).

Firstly the red edge of the profile steps towards the blue as the material at more extreme positive velocities is beyond the O star. Secondly the depth of the absorption decreases from phase 0.0 to a minimum at phase 0.25 and then increases again to phase 0.5. The reason for this behaviour is that at quadrature the line of sight to the O star is at its maximum distance from the WR star and less dense material is being sampled. Also at this phase material at intermediate radii will have a larger component of its velocity across the line of sight and so its absorption will be displaced

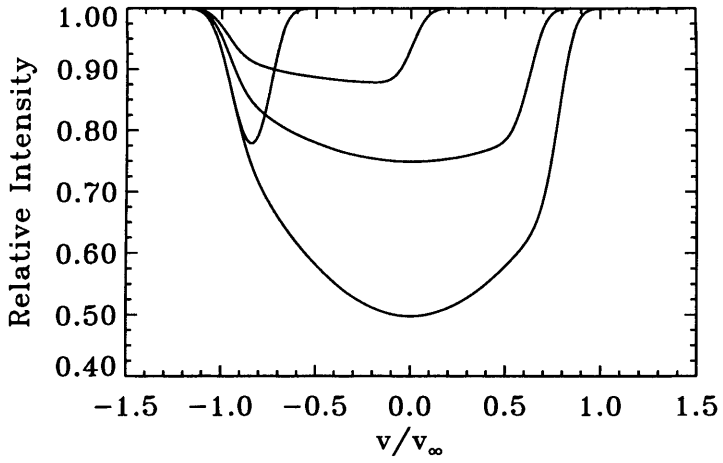

Figure 5.5: Profiles at phases 0.0, 0.1, 0.25 and 0.5, showing the change in the selective absorption when the fraction of absorbing ions, f_j falls linearly with radius, from 0 at r = 0 to 1 at $r = 5000R_\odot$. The inclination $i = 60°$ and all other parameters are the same as in the previous plot.

slightly to the red, pulling in the lower part of the blue edge of the line. At phase 0.5 the line of sight is the same as at phase 0.0, (and similarly with phases 0.4 and 0.1 and all other complimentary phases), except that the absorption is truncated because the O star is now on the near side of the system. As the inclination decreases from 80° to 40° the line of sight to the O star also samples progressively less dense material and the absorption decreases. Also the variation with phase becomes progressively smaller as the blue edge of the absorption tends to zero velocity. The variation at phase 0.5 shows this most clearly.

When the fraction of absorbing ions, f_j is allowed to change the behaviour is radically altered. Figure 5.5 shows the profiles when f_j falls linearly with radius, α = -1, and as may be expected, the absorption at large radii is significantly reduced. Elements of the behaviour in the simple case described above may still be seen, in particular the reduction in absorption towards quadrature.

In the reverse situation (Figure 5.6), when f_j increases with radius, the absorption is reduced at small radii and only becomes significant at the edge of the wind. As the absorption takes place at large radii the variation with phase is all but eliminated.

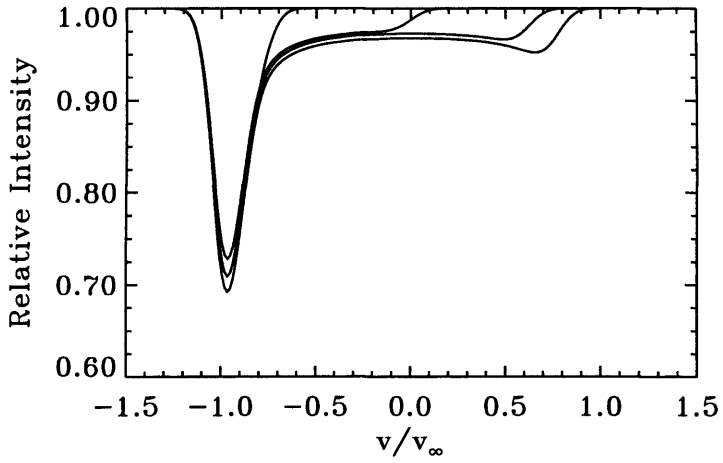

Figure 5.6: Profiles at phases 0.0, 0.1, 0.25 and 0.5 showing the change in the selective absorption when the fraction of absorbing ions, f_j increases linearly with radius out to $r = 1000R_\odot$. All other parameters are the same as in the previous plot.

The final Figure (5.7) in this section shows the effect of increasing β from 1 to 3, while keeping f_j constant. The effect of a slower velocity law is to increase the density at all points in the wind, but preferentially at smaller radii, with a correspondingly increase in the absorption (cf., Figure 5.4b). The profiles under these circumstances bear some resemblance to the those with a decreasing ion fraction (cf., Figure 5.5), for obvious reasons. However it is conceivable that observationally it may be difficult to discriminate between the two cases in the absence any other information.

5.7.2 O-star cavity

As the O star revolves around the WR component (relatively speaking) the cavity in the wind will remove material over a range of velocities, depending on the orbital phase. At phase zero the cavity will be directed generally away from the observer and only a small part of the absorbing column, between the two stars, will fall in the cavity. As the phase increases more of the absorbing column will lie in the cavity and it will have a progressively larger effect on the profiles. Near phase 0.5 little, or even none, of the WR wind will lie along the line of sight to the O star leading to a substantial reduction in absorption. If the the cone opening angle $\theta + i > 90$ then the

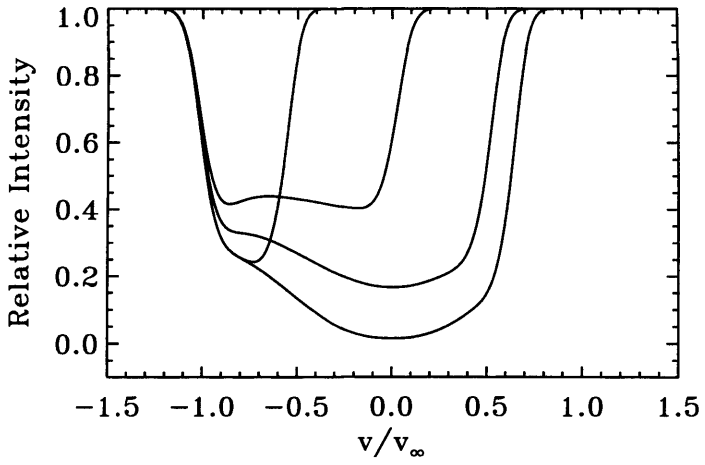

Figure 5.7: Profiles at phases 0.0, 0.1, 0.25 and 0.5 showing the profiles with $\beta = 3$. The fraction of absorbing ions, f_j is constant and $i = 60°$. All other parameters are the same as in the previous plots. cf., Figures 5.4b and 5.5.

undisturbed O-star wind will be seen with its own spectral signature. The cavity will also have a second effect on the profiles. Due to orbital rotation the axis of the cavity will be offset from the line connecting the two stars. The effect will be to cause an asymmetrical perturbation of the profiles so that the absorption at opposite phases, e.g., 0.25 and 0.75 is no longer identical. In the example the stars have the following parameters, $\beta = 1$, $\alpha = 0$, $\dot{M}_{WR} = 5.10^{-5}$ $M_\odot\,yr^{-1}$, $\dot{M}_O = 5.10^{-6}$ $M_\odot\,yr^{-1}$, $v_{WR\infty}$ = 2200 $km\,s^{-1}$, $v_{O\infty}$ = 2750 $km\,s^{-1}$, which lead to $\mathcal{P} = 8$, $x_0 = 0.74$ and $\theta = 54°$. For an orbital velocity of 300 $km\,s^{-1}$, the offset angle, $\delta = 9$ °. Figure 5.8 compares the simple case, as in the previous section, with the cavity included at six phases 0.0, 0.15, 0.25, 0.5, 0.75 and 0.85. In the simple case there are apparently only 4 profiles as those at opposite phases are identical. When the cavity is included the red edge of the absorption moves to the blue and the profiles at opposite phases are split. At phase 0.5 the line of sight lies entirely within the O-star wind and so the absorption is almost eliminated. In the second example (Figure 5.9) the O star shows the same line as seen in the WR wind which contributes to the absorption at all phases, but is particularly obvious at phase 0.5 where it is revealed by its higher terminal velocity.

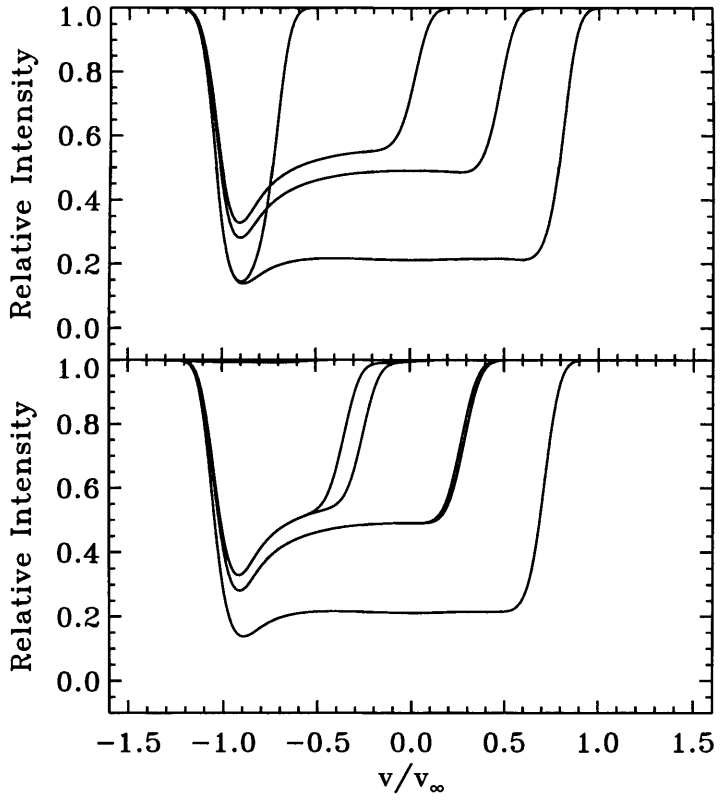

Figure 5.8: Profiles at phases 0.0, 0.15, 0.25, 0.5, 0.75 and 0.85 showing the simple case (*above*) and with the cavity included (*below*). The fraction of absorbing ions, f_j is constant and $i = 60°$. The opening angle, θ, and offset angle of the cone, δ, are 54° and 9° respectively.

5.7.3 Shock zone

The number of free parameters available to describe the shock zone makes a very wide variety of profiles possible, especially when the distribution of absorbing ions can also be changed. However, there are only two basic effects. One depends on where the absorption line is formed in the wind, either inside or outside the orbit, and the second depends on whether or not the line of sight ever falls completely within the shock zone. The first effect is a wave of absorption moving to negative velocities from phase 0.0 to 0.5 and back again from phase 0.5 to 0.0. As the material in the shock zone is streaming along the contact discontinuity and not moving radially it will have a different velocity component along the line of sight, relative to the WR wind. When the shock zone is projected against the O star the additional absorption will be seen, and will lead the O star around the first half of the orbit, and the opposite side of

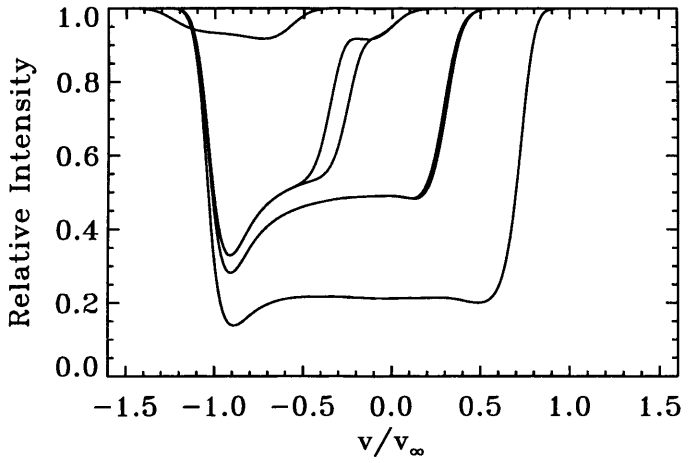

Figure 5.9: Profiles at phases 0.0, 0.15, 0.25, 0.5, 0.75 and 0.85 calculated with the cavity included showing the effect of the relatively strong line in the O-star wind. All other parameters are as in the previous plot.

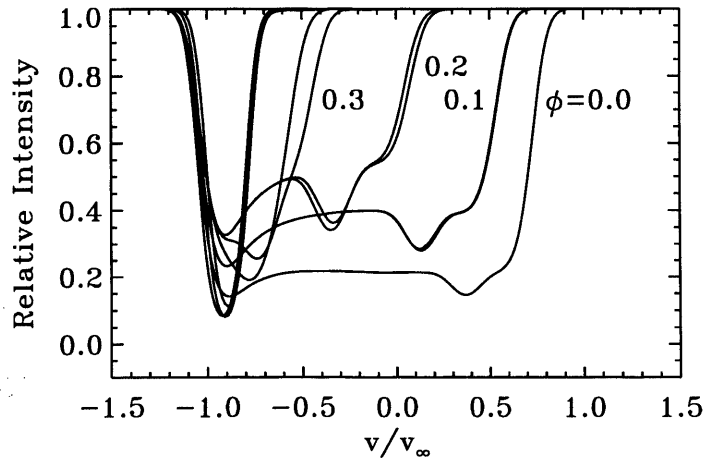

Figure 5.10: Profiles at calculated at every 0.1 phase with the cavity included showing the effect of the shock zone on a strong line. The profiles at $\phi = 0.0$, 0.1, 0.2 and 0.3 and their complimentary phases are indicated, while the profiles at $\phi = 0.4$, 0.5 and 0.6 are superimposed. The wave of additional absorption due to the shock zone is clearly seen moving to negative velocities.

the shock zone will follow the O star around the second half of the orbit. For this effect to be seen there needs to be a sufficient density of absorbing ions over most of the velocity range. In the first example the wind parameters have been adjusted

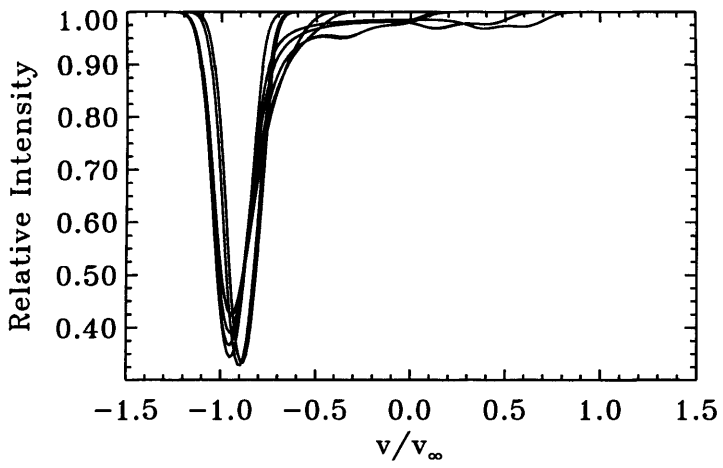

Figure 5.11: Profiles at calculated at every 0.1 phase with the cavity included showing the effect of the shock zone on a weak line. The profiles are mostly superimposed but at $\phi \sim 0.5$ they show a clear shift to positive velocities due to the inclination of the stream along the contact discontinuity to the line of sight.

to create an almost constant fraction of absorbing ions (similar to the $\alpha = 0$ case, Figure 5.4) and the other parameters are as before, except that the system is viewed along the edge of the shock zone at inferior conjunction.

In the second example the line is weaker and formed over a large distance in the outer part of the wind, similar to Figure 5.6. Although the profiles are mostly superimposed there are changes in strength, and around inferior conjunction the line shows a clear shift to positive velocities. The shift is relatively small, in this case $\sim 0.1 v_\infty$, but by optimising the combination of inclination and opening angle it is possible to at least double the movement. However, it must be remembered that the shock zone is treated in an idealised way, and the velocity distribution, along with many other important parameters are uncertain.

Chapter 6

Observations and Data Reduction

6.1 IUE data

The data analysed consist entirely of UV spectra obtained with the *International Ultraviolet Explorer* (*IUE*). *IUE* carries two echelle spectrographs which cover the wavelength ranges 1150 - 2100Å, (the short wavelength, SW) and 1900 - 3300Å, (the long wavelength, LW), and both have two resolution modes. At high resolution (HIRES) $\Delta\lambda \sim 0.1$Å the spectrographs are used in full echelle mode and ~ 60 spectral orders fill the camera faceplate. In low resolution (LORES) mode $\Delta\lambda \sim 6$Å the echelle cross dispersers are used alone to produce a single spectral order covering the full wavelength range. The spectrographs have two apertures. The large aperture (LAP) is 10×20 arcsec while the small aperture (SAP) is $\sim$ 3 arcsec in diameter and vignettes the beam. LORES images through the LAP are absolutely calibrated but HIRES images are not. Imprecision in centring the star in the SAP make the transmission unpredictable so these spectra lose their absolute photometry. Many of the early high-resolution spectra of γVel were taken through the SAP and have to be scaled before they can be inter-compared. Both spectrographs have prime (P) and redundant (R) cameras. The SWP camera has been used throughout the mission while the LWR was used until 1984 and the LWP since then.

The standard *IUE* processing, IUESIPS, takes the *raw* image, and produces a *photometric* image, together with some other intermediate partly processed images, and

the final extracted 1-d spectrum. The intensity in each pixel in the raw image is given as a Data Number (DN) in the range 0 – 255. Overexposed (*saturated*) parts of the spectrum are set to 255 DN. In the photometric image the DN values for each pixel are converted to fluxes via an Intensity Transfer Function (ITF) and are given in terms of a Flux Number (FN). Two types of photometric image have been used. Until about 1981 the raw image was geometrically as well as photometrically corrected to produce a *GPHOT* image. The geometric correction removes the distortion in the camera and the read process. More recently the raw image has been photometrically corrected in raw space, to yield a *PHOT* image, and the geometric correction left to a later part of the processing.

There are a variety of marks and blemishes on the detectors that may interfere with the spectra. Embedded in the camera faceplate is a grid of fiducial marks or reseaus which are used in the geometric correction. Each reseau creates an essentially black spot about 2×2 pixels on the raw image and some of these marks inevitably appear in the spectrum. The processing usually recognises them and they are flagged accordingly. There are also some other permanent blemishes, hot spots and other features to be aware of. Cosmic-ray hits produce bright features on the image but these range from the obvious spots to diffuse comet-like structures, the effects of which are not easily seen in the spectrum. These problems may be identified by viewing the whole raw or photometric image. Some images, particularly those from the LWR, may be affected by microphonic noise, which introduces a spurious varying signal of over 20 DN on a few scan lines, almost anywhere on the raw image. Depending on the resolution and where it occurs the microphonic noise may or may not interfere with the spectrum. Images may also suffer from brief periods of data dropouts. These are flagged by the processing and are comparatively rare.

The *IUE* spectra have been produced from the photometric image using the IUEDR package (Giddings et al. 1996, Rees et al. 1996a, 1996b) which offers significant advantages over IUESIPS. For HIRES spectra IUEDR merges the spectral orders to give a wavelength calibrated spectrum corrected for the echelle ripple, in FN/sec. The LORES spectra are absolutely calibrated in erg/cm^2/Å/sec. The DIPSO package (Howarth et al. 1996) has been used in the analysis for data manipulation and

presentation.

The dynamic range of *IUE*'s detectors limits the signal-to-noise ratio of the spectra to $\sim$ 20, in the optimally exposed parts of the spectrum. In general it is rather less than this but may be improved to some extent by co-adding spectra, with a small loss of resolution. However, the fixed pattern noise (FPN), which is due to errors in registering an image against the ITF grid, restricts the improvement in signal-to-noise, and it does not increase with increasing number of spectra.

In the most strongly exposed parts of the spectrum the DN values often lie on the extrapolated parts of the ITF which can lead to significantly higher than usual uncertainties in the flux. As the ITF for each pixel can be very different this extrapolation can result in large pixel-to-pixel variations in flux. The effect is most usually seen as a dramatic increase in noise on the peaks of emission lines, where under usual circumstances it might be expected to show the highest signal to noise.

6.2 Radial velocities

Reliable orbital parameters of WR+O systems are necessary for any investigation of the wind effects. *IUE* data have been shown capable of providing good radial velocities for O-star binaries and the same technique is applied later to the WR+O systems.

The radial velocities are determined using a cross-correlation technique, the bare bones of which are provided within the DIPSO package. The procedure has been used extensively to determine the orbits of O-type binaries in a series of papers running in *The Observatory* magazine (Stickland et al. 1996a) and of massive X-ray binaries (Stickland & Lloyd 1993, Stickland et al. 1996b). Its power lies in the ability to take advantage of the many weak lines which individually are poorly defined or invisible, but collectively are strongly correlated. In some sense this can also be a disadvantage because it is not always clear what is contributing to the correlation, as will be seen later.

The basic method is to correlate a stellar spectrum against a suitably chosen standard

or template spectrum. The process involves defining a mask to exclude undesirable features from the correlation and rectifying the spectra using either a polynomial or a smoothing function. Initially the cross-correlation is performed on only the interstellar lines to align the spectra at a constant velocity. Selecting the most reliable combination of stellar mask, template spectrum and rectifying process requires considerable experimentation. The template for the O-type star is selected from a bank of sharp-lined stars which cover an appropriate range of temperatures. The suitability of the template star is gauged by the degree of correlation it shows with the spectrum of the binary, and this may also be used as an indication of the spectral type of the O star, which is not always well known. The O-star mask is chosen to exclude interstellar lines, emission and P-Cygni lines.

The Wolf-Rayet template is chosen in the same way from spectra in the archive of similar type stars. The WR emission line mask can be more problematical as not all the lines show the same velocity amplitude and some lines are changed as much by wind effects as by velocity variation.

From the work on O-type binaries there is little to choose between the different methods for rectifying the spectrum. However, for the WR+O binaries the smoothing function is clearly superior, because it is more able to follow the wanderings of the spectrum, and different levels of smoothing enable the absorption and emission lines to be better differentiated.

To determine the radial velocity it is a simple matter of correlating the appropriately masked O-star- and WR-template spectra with the spectra of the binary. The result is a distribution of correlation coefficient with velocity where the peak of the distribution is taken to give the velocity of the component. Two methods of determining the peak velocity are routinely used. The first simply gives the velocity by interpolating around the top few values, while the second fits a Gaussian profile. Depending on the symmetry of the correlation profile these may or may not give the same value.

6.3 The continuum

The strength, width and number of emission and P-Cygni lines in Wolf-Rayet stars is such that, particularly in the ultraviolet, there are no stretches of uncontaminated continuum. The same situation probably prevails some way into the optical region. The *IUE* high-resolution data are not flux calibrated and also contain the effects of interstellar reddening. In the short-wavelength region this will appear as an additional slope but in the long-wavelength region the broad 2200Å feature has to be removed. Placing the continuum in the high-resolution spectra has been guided by the appearance of the spectra at low-resolution. In the short-wavelength region it is assumed that the continuum is smooth and not strongly curved and low order polynomial fits produce an acceptable continuum level. It is of course impossible to say how true this is. The sections of spectrum that closely follow the fit, together with some end points are used to define "continuum regions" for the high-resolution spectra. A combination of de-reddening and dividing by low-order polynomials fitted to the continuum regions was used to normalise the short-wavelength spectra. In the long-wavelength region the spectrum is less crowded, but there is significant curvature due to the λ2200Å feature. After some experimentation the spectra were normalised by fitting high-order ($\sim$ 9) polynomials to the "continuum regions". Although this process removes the variation in flux level due to camera degradation and use of the small aperture, it does mean that very broad changes in the spectrum may be missed.

Chapter 7

Gamma^2 Velorum

7.1 Introduction

The brightest and closest Wolf-Rayet star is the WC+O binary, γ^2 Velorum (HR 3207, HD 68273) which lies in the direction of the Gum nebula complex together with several other luminous stars, including ζ Pup. The spectral classification of the WR component is generally taken as WC8 (Smith 1968b, van der Hucht et al. 1981, see also Eenens & Williams 1994) but the nature of the companion is less clear. Progressively later types have been assigned from O6 (Smith 1955), O7.5 (Ganesh & Bappu 1967), O8 (Baschek & Scholz 1971) to O9I (Conti & Smith 1972) which until very recently was widely, but not universally, accepted. With more recent optical spectra and the measurement of a more reliable distance by HIPPARCOS of 260±35 pc, the O star is now reclassified from a supergiant to a giant and the system is given as WC8+O8III (van der Hucht et al. 1997, Schaerer et al. 1997). Despite the reclassification Schaerer et al. still find a large luminosity difference between the two components. From a combination of spectral analysis, model atmospheres and evolutionary models they find M_V(system) = −5.5 and ΔM_V between 1.4 and 1.8 mag. Similar values of the magnitude difference have consistently appeared in the literature. From interferometric measurements Hanbury Brown et al. (1970) found $\Delta M_V \sim 1.2$ but could not tell which component was the brighter. Comparing TD1-A S2/68 emission line intensities of γ^2 Vel with the single WC8 star HD 192103 (WR135) Willis & Wilson

(1976) derived Δm (UV) = 1.8. By combining the continuum measurements with the Hanbury Brown et al. (1974) angular diameters of the O star and ζ Ori (O9I), they also found Δm (UV) = 1.4, both in favour of the O star. Using emission lines ratios in the optical Conti & Smith (1972) and Brownsberger & Conti (1993) found ΔM_V = 1.4 and 1.9 respectively, and from an analysis of absorption lines Baschek & Scholz found the O star to be brighter by between 1.0 and 1.8 mag. The only inconsistent result is that of van der Hucht (1975) who, on the basis of TD1-A S59 absorption line measurements, suggested that in the region $\lambda\lambda$ 2000 – 2500 Å the two components were of equal luminosity. The reclassification of the O star as a giant is also supported indirectly by the high rotational velocity, $v \sin i$ = 220 km s^{-1}, found by Baade et al. (1990), which is typical of O giants but very rare for supergiants. Quite what impact the reclassification will have on their other conclusion, that the O star is a non-radial pulsator, remains to be seen.

The magnitude difference of Schaerer et al. gives M_v(WR) = -3.5 to -3.9 and M_V(O) ≈ -5.2, where v is the narrow band continuum system of Smith (1968a,b), and using the zero point correction $M_v = M_V + 0.1$ (Schmutz & Vacca 1991). The absolute magnitude of the O star is consistent with a classification of O8 III but the WR component is about a magnitude fainter than the mean for WC8 stars, $<M_v(\mathrm{WC8})>$ = -4.8 ± 0.4 given by van der Hucht et al. (1988).

One other consequence of the new distance to γ^2 Vel is the revision of the radio determined mass loss rate (Leitherer et al. 1997) which is now given as $\dot{M} = 2.8 \times 10^{-5}$ $M_\odot$ yr^{-1} (Schaerer et al. 1997).

Spectral variations on time scales of minutes to days have been reported, mostly for the He II λ4686 and C III/C IV λ4650 lines. Jeffers et al. (1985) provide a summary of the earlier work and find variations in the blue wing of the C III/C IV λ4650 line on a time scale of a few minutes, which they attribute to a neutron star in a 5.4 day period around the WC8 component. The radial velocity variations implied were not found by Moffat et al. (1986). Moffat (1977) did find changes in the optical emission-line profiles on a 15–19 day time scale, which were stronger in the lower ionization lines, those of C III and He I, relative to C IV and He II. The variations are apparently not correlated with orbital phase.

The most dramatic line profile variations are strongly correlated with orbital phase and were first seen in γ^2 Vel by Willis & Wilson (1976) in the UV spectra obtained with the S2/68 experiment on the TD1-A satellite. Using the S2/68 and earlier rocket UV spectra (Burton et al. 1973, 1975) Willis & Wilson found substantial changes in the emission line strengths of C IV λ1548, 1550, Si IV λ1393, 1402 and C III λ2297 which were interpreted as being due to selective absorption by the WR wind of the O-star continuum. Analysis of *Copernicus* and early *IUE* spectra (Willis et al. 1979) showed variations in a wide range of low-excitation and resonance lines of C II, C III, C IV, Si II, Si III, Si IVand He II. High excitation lines do not show any effect, as discussed in § 4.1. The continuum itself also shows no variation. Prinja et al. (1990) demonstrated that the C IV λ1548 line of the O-star wind is visible in the composite spectrum due the the higher terminal velocity of the O-star wind. In a very detailed discussion of the *Copernicus* and *IUE* spectra St-Louis et al. (1993) showed the presence of several strong O-star lines. They were able to describe most of the variations of the WR-wind lines of C II and C III, and the S IV, Si IV and C IV resonance doublets which appear in the spectra of both components and N V resonance doublet, which appears only in the O-star wind, successfully in terms of the selective absorption model. The changing visibility of the O-star lines was attributed to the effects of the collision between the WR and O-star winds. The inclination of the system is such that at inferior conjunction, i.e. O star in front of the WR star, the cavity in the WR wind caused by the O-star wind is directed towards the observer and so the O star is seen directly. However, problems appeared in the duration of the O-star's visibility and much discussion centred on the collapse of the wind on to the surface of the O star. The recent work on sudden radiative breaking by Gayley et al. (1997) suggests that this effect will be particularly important in γ^2 Vel and will significantly affect the force of the collision, probably preventing the collapse discussed by St-Louis et al. (see 3.2). A second difficulty concerns the C III] λ1909 line and the Fe IV pseudo continuum, which was identified previously in WN stars (see Eaton et al. 1985, Koenigsberger 1990). St-Louis et al. were able to demonstrate convincingly that a large region of the spectrum is affected by Fe IV absorption but had to introduce an arbitrary shift of -950 km s^{-1} on the synthesised spectrum. The variation of the C III] λ1909 line also seemed to take place too far to the blue which St-Louis et al. attributed to some

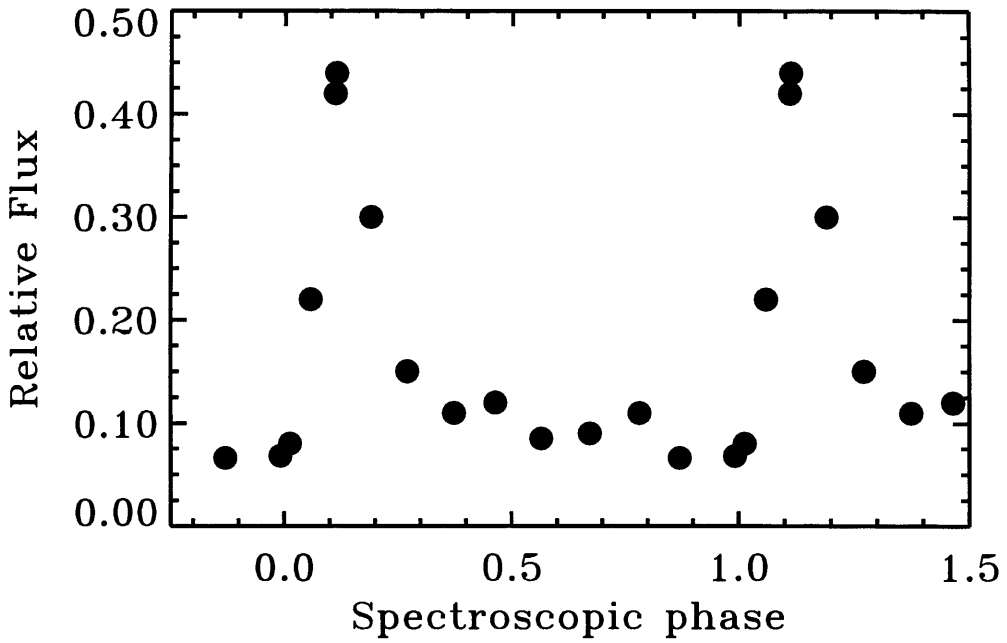

Figure 7.1: The *ROSAT* PSPC observations of γ^2 Vel taken from Willis et al. (1995) as a function of spectroscopic phase. Inferior conjunction occurs at $\phi = 0.03$. See the text for details.

effect of the wind collision. These questions will be discussed in more detail later.

The final important observation of phase-dependent variations of γ^2 Vel are those in X-rays (Figure 7.1). Willis et al. (1995) showed that the *ROSAT* PSPC flux varies by a factor of $\sim$ 4 during the orbit, and is repeatable from cycle to cycle. The maximum X-ray flux is seen at inferior conjunction, when the cavity due to the O star is directed towards the observer, and the absorption by the WR wind is least. Further observations around inferior conjunction with the *ASCA* satellite by Stevens et al. (1996) confirm these findings (see also § 2.6).

7.2 Observations

The *IUE* archive contains 112 high-resolution spectra of γ^2 Vel taken in the short-wavelength camera and 100 in the long-wavelength range. Images were taken pre-

dominantly in two periods, the first in 1978 – 1979 and the second during the final year of operations, 1996. A small number of images were taken at other times. All the early images were taken through the small aperture and the later images were taken through both the large and small apertures. The logs of short- and long-wavelength images are given in Tables 7.1 and 7.2 respectively together with the orbital phases calculated using the ephemeris of Schmutz et al. (1997, § 7.3). The spectra were extracted from the *IUE* G/PHOT images using the IUEDR routine as described earlier in § 6.1. The spectra were normalised using sections of pseudo continuum which were free of strong P-Cygni profiles and obvious emission lines, and which also appeared relatively smooth on the low-resolution spectra. The SWP spectra were first rendered relatively straight by de-reddening and dividing by a smoothed white dwarf spectrum, and finally normalised by fitting a low order polynomial to the continuum regions. The long-wavelength spectra on the other hand were simply fitted by a high order polynomial as there is more pseudo continuum. In both cases the procedure is completely automatic and the result depends only on the continuum regions chosen.

Table 7.1: IUE short-wavelength images

Image	HJD	Phase	Image	HJD	Phase
SWP 1358	2443612.7132	0.1363	SWP 3498	2443843.5137	0.0753
SWP 1359	2443612.8513	0.1381	SWP 3572	2443854.5544	0.2159
SWP 1413	2443623.7482	0.2768	SWP 3677	2443865.5604	0.3560
SWP 1425	2443625.7161	0.3019	SWP 3776	2443875.5941	0.4838
SWP 1545	2443643.5362	0.5288	SWP 3777	2443875.6531	0.4846
SWP 1546	2443643.5994	0.5296	SWP 3935	2443891.8688	0.6911
SWP 1605	2443651.5442	0.6308	SWP 4636	2443947.5904	0.4006
SWP 1606	2443651.6095	0.6316	SWP 4719	2443954.3507	0.4867
SWP 1717	2443664.3020	0.7932	SWP 5480	2444035.3004	0.5175
SWP 1718	2443664.3361	0.7937	SWP 6175	2444099.2232	0.3315
SWP 1719	2443664.3965	0.7944	SWP 6351	2444118.1468	0.5725
SWP 1761	2443670.4573	0.8716	SWP 6532	2444132.7575	0.7585
SWP 1811	2443678.5355	0.9745	SWP 6672	2444146.0001	0.9272
SWP 2070	2443711.2436	0.3910	SWP 6673	2444146.0182	0.9274
SWP 2290	2443734.9364	0.6927	SWP 6674	2444146.0363	0.9276
SWP 2291	2443734.9628	0.6930	SWP 6675	2444146.0870	0.9283
SWP 2295	2443735.2260	0.6964	SWP 6676	2444146.1043	0.9285
SWP 2388	2443745.0940	0.8220	SWP 7200	2444200.3578	0.6194
SWP 2389	2443745.1239	0.8224	SWP 7980	2444287.7268	0.7319
SWP 2504	2443757.8372	0.9843	SWP42737	2448545.3041	0.9478
SWP 2514	2443758.9365	0.9983	SWP42771	2448550.2467	0.0108
SWP 2683	2443770.1527	0.1411	SWP42783	2448552.2051	0.0357
SWP 2817	2443782.5328	0.2988	SWP42963	2448561.9985	0.1604
SWP 2964	2443795.4485	0.4632	SWP43022	2448567.1439	0.2260
SWP 3139	2443807.0476	0.6109	SWP43119	2448577.2228	0.3543
SWP 3271	2443821.3607	0.7932	SWP46918	2449030.5559	0.1270
SWP 3377	2443830.9312	0.9151	SWP53064	2449702.8442	0.6879
SWP 3378	2443830.9680	0.9155	SWP56731	2450117.9850	0.9743
SWP 3379	2443830.9944	0.9159	SWP56732	2450118.0107	0.9747
SWP 3386	2443831.6569	0.9243	SWP56774	2450121.7434	0.0222

Table 7.1: continued. IUE short-wavelength images

Image	HJD	Phase	Image	HJD	Phase
SWP56775	2450121.7892	0.0228	SWP57022	2450200.7592	0.0284
SWP56776	2450121.8420	0.0235	SWP57023	2450200.8237	0.0292
SWP56777	2450121.8823	0.0240	SWP57138	2450218.6459	0.2562
SWP56778	2450121.9233	0.0245	SWP57139	2450218.7119	0.2570
SWP56779	2450121.9677	0.0251	SWP57142	2450218.8695	0.2590
SWP56794	2450125.7094	0.0727	SWP57144	2450219.0063	0.2607
SWP56795	2450125.7559	0.0733	SWP57256	2450229.6920	0.3968
SWP56796	2450125.7990	0.0738	SWP57257	2450229.7496	0.3975
SWP56797	2450125.9129	0.0753	SWP57261	2450230.0239	0.4010
SWP56798	2450125.9552	0.0758	SWP57262	2450230.0670	0.4016
SWP56802	2450126.0122	0.0766	SWP57300	2450234.6432	0.4599
SWP56803	2450127.1538	0.0911	SWP57301	2450234.7098	0.4607
SWP56827	2450131.9115	0.1517	SWP57305	2450234.9487	0.4638
SWP56828	2450131.9601	0.1523	SWP57306	2450234.9938	0.4643
SWP56829	2450132.0101	0.1529	SWP57307	2450235.0411	0.4649
SWP56830	2450132.0587	0.1536	SWP57348	2450240.6374	0.5362
SWP56831	2450132.1177	0.1543	SWP57349	2450240.7450	0.5376
SWP56857	2450140.8489	0.2655	SWP57362	2450242.7074	0.5626
SWP56858	2450140.9198	0.2664	SWP57363	2450242.7276	0.5628
SWP56859	2450141.0024	0.2674	SWP57364	2450242.7498	0.5631
SWP56898	2450164.1347	0.5620	SWP57365	2450242.7783	0.5635
SWP56899	2450164.1611	0.5623	SWP57366	2450242.8019	0.5638
SWP56901	2450164.2194	0.5631	SWP57367	2450242.8262	0.5641
SWP56902	2450164.2465	0.5634	SWP57392	2450247.3441	0.6216
SWP56988	2450190.9609	0.9036	SWP57393	2450247.3697	0.6219
SWP56989	2450191.0568	0.9048	SWP57394	2450247.4052	0.6224

Table 7.2: IUE long-wavelength images

Image	HJD	Phase	Image	HJD	Phase
LWR 1315	2443612.7569	0.1369	LWR 4084	2443954.3479	0.4867
LWR 1316	2443612.8368	0.1379	LWR 4753	2444035.2976	0.5175
LWR 1396	2443625.6661	0.3012	LWR 5340	2444099.2197	0.3315
LWR 1497	2443643.5689	0.5292	LWR 5486	2444118.1496	0.5725
LWR 1498	2443643.6279	0.5300	LWR 5601	2444132.7526	0.7585
LWR 1543	2443651.5783	0.6312	LWR 5717	2444146.0689	0.9280
LWR 1619	2443664.3673	0.7941	LWR 6210	2444200.3599	0.6194
LWR 1651	2443670.4900	0.8720	LWR 6952	2444287.7226	0.7319
LWR 1691	2443678.5279	0.9744	LWP21498	2448545.3118	0.9479
LWR 1869	2443711.2394	0.3909	LWP21539	2448550.2432	0.0107
LWR 2073	2443734.9593	0.6930	LWP21550	2448552.2086	0.0358
LWR 2074	2443735.0017	0.6935	LWP21604	2448562.0020	0.1605
LWR 2076	2443735.2294	0.6964	LWP21650	2448567.1474	0.2260
LWR 2167	2443745.0975	0.8221	LWP21754	2448577.2290	0.3544
LWR 2298	2443758.9407	0.9984	LWP24894	2449030.5587	0.1271
LWR 2511	2443782.5363	0.2988	LWP29719	2449702.8359	0.6878
LWR 2512	2443782.5696	0.2992	LWP31933	2450117.8871	0.9731
LWR 2596	2443795.4652	0.4635	LWP31934	2450117.9309	0.9737
LWR 2708	2443807.0497	0.6110	LWP31935	2450117.9566	0.9740
LWR 2882	2443821.3655	0.7933	LWP31950	2450121.7455	0.0222
LWR 2963	2443830.9340	0.9151	LWP31951	2450121.7913	0.0228
LWR 2964	2443830.9694	0.9156	LWP31952	2450121.8441	0.0235
LWR 2973	2443831.6597	0.9244	LWP31953	2450121.8844	0.0240
LWR 3075	2443843.5172	0.0753	LWP31954	2450121.9254	0.0245
LWR 3145	2443854.5517	0.2159	LWP31955	2450121.9698	0.0251
LWR 3240	2443865.5632	0.3561	LWP31972	2450125.7150	0.0728
LWR 3510	2443891.8730	0.6911	LWP31973	2450125.7587	0.0733
LWR 4026	2443947.5835	0.4005	LWP31974	2450125.8018	0.0739

Table 7.2: continued. IUE long-wavelength images

Image	HJD	Phase	Image	HJD	Phase
LWP31975	2450125.9170	0.0753	LWP32311	2450229.7538	0.3976
LWP31976	2450125.9587	0.0759	LWP32312	2450229.9802	0.4005
LWP31982	2450127.0157	0.0893	LWP32313	2450230.0107	0.4009
LWP31983	2450127.1580	0.0911	LWP32319	2450234.5939	0.4592
LWP31984	2450127.3594	0.0937	LWP32320	2450234.6487	0.4599
LWP32002	2450131.9177	0.1518	LWP32321	2450234.7161	0.4608
LWP32003	2450131.9636	0.1523	LWP32322	2450234.9452	0.4637
LWP32004	2450132.0136	0.1530	LWP32323	2450234.9938	0.4643
LWP32005	2450132.0622	0.1536	LWP32344	2450240.6207	0.5360
LWP32006	2450132.1205	0.1543	LWP32345	2450240.6881	0.5368
LWP32027	2450140.8295	0.2652	LWP32346	2450240.7360	0.5375
LWP32028	2450140.9024	0.2662	LWP32351	2450242.5602	0.5607
LWP32029	2450140.9503	0.2668	LWP32352	2450242.5838	0.5610
LWP32030	2450141.0073	0.2675	LWP32353	2450242.6109	0.5613
LWP32137	2450190.9880	0.9040	LWP32354	2450242.6345	0.5616
LWP32138	2450191.0401	0.9046	LWP32355	2450242.6616	0.5620
LWP32225	2450200.7682	0.0285	LWP32364	2450247.1198	0.6187
LWP32301	2450218.6522	0.2562	LWP32365	2450247.1559	0.6192
LWP32302	2450218.7070	0.2569	LWP32366	2450247.1829	0.6195
LWP32303	2450219.0126	0.2608	LWP32367	2450247.2211	0.6200
LWP32309	2450229.6184	0.3959	LWP32368	2450247.2614	0.6205
LWP32310	2450229.6968	0.3969	LWP32369	2450247.3017	0.6211

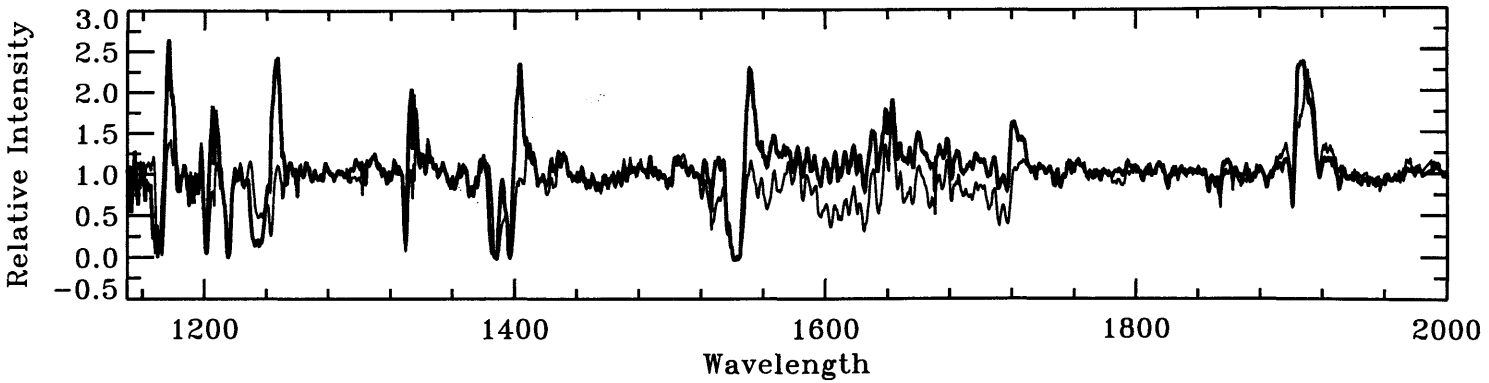

Figure 7.2: The short-wavelength *IUE* spectrum of γ^2 Vel near superior (*thin line*) and inferior conjunction (*thick line*). See the text for details.

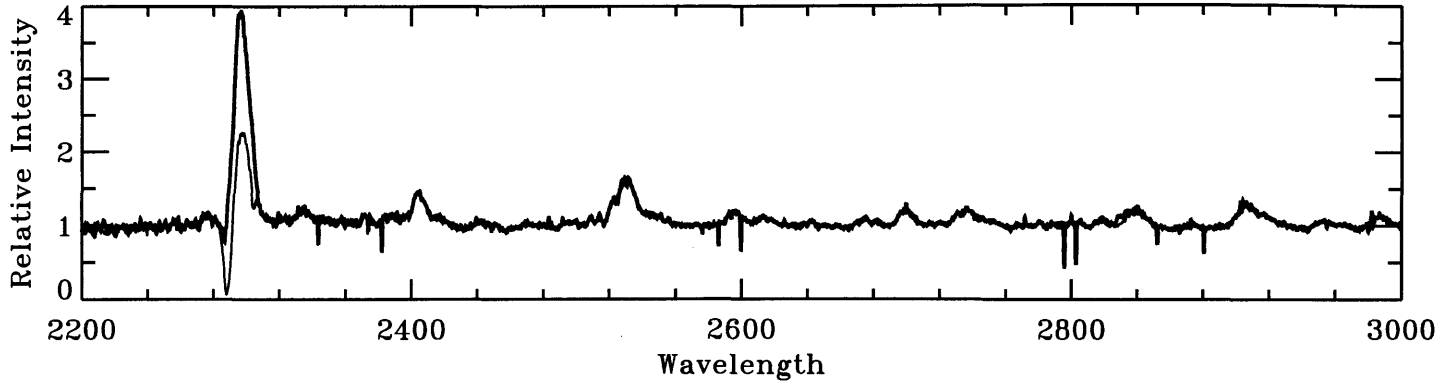

Figure 7.3: The long-wavelength *IUE* spectrum of γ^2 Vel near superior (*thin line*) and inferior conjunction (*thick line*). See the text for details.

7.3 The orbit

γ^2 Vel was first shown to be a double-lined spectroscopic binary by Sahade (1955) but Ganesh & Bappu (1967) obtained the first orbital solution, which had a period of 78.5 days and significant eccentricity. Niemela & Sahade (1980) used optical data covering a long time interval to refine the period to 78.5001 days and found a higher value of the eccentricity of $e = 0.4$. Using archival optical data Pike et al. (1983) derived a solution very similar to that of Niemela & Sahade with one important exception; the amplitude of the O star was found to be about half the previous value, $K_{\rm O} = 41$ km s^{-1} as opposed to $K_{\rm O} = 70$ km s^{-1} leading to substantially lower masses for the components. Moffat et al. (1986) re-observed the system and derived a solution with a larger amplitude for the O star, similar to that of Niemela & Sahade, and which was also more consistent with the supergiant classification. An orbit derived from early *IUE* data was published by Stickland & Lloyd (1990), and although the scatter was large, the result was contrary to Moffat et al. and favoured a lower amplitude for the O star. However, the situation has now been resolved. Schmutz et al. (1997) have derived a new solution, based on a long series of high-resolution, high signal-to-noise optical spectra combined with earlier data. The orbital elements, given in Table 7.3, support the period and velocity amplitudes given by Pike et al. and Stickland & Lloyd, and are consistent with the giant classification of the O star. Schmutz et al. also suggest that a fundamental limit on the precision of the orbital parameters of this system may have been reached. They find that some of the emission line velocities deviate significantly between the observations made in 1995 and 1996, suggesting a variable atmospheric or wind component. Also the C III/C IV λ4650 emission line solution shows a small but significant phase shift (and other associated changes in orbital elements) which is attributed to additional emission components caused by the wind-wind interaction.

7.3.1 Inclination

An upper limit to the inclination of, $i < 70°$ was set by Moffat (1977) from a series of photometric observations over 37 days around superior conjunction, which showed no

continuum eclipse. Using revised values of the the stellar radii and orbital elements Schmutz et al. have re-determined the upper limit as $i < 86°$. They have also taken the total mass of the system, $M_{\rm WR+O} = 29.5 \pm 15.9$ M$_\odot$, derived from the HIPPARCOS distance and the Hanbury Brown et al. angular separation (van der Hucht et al. 1997, Schaerer et al. 1997) and compared it with $M_{\rm WR+O} \sin^3 i$ to derive $i = 81°$. As the total mass is rather poorly constrained the uncertainty in the inclination is large, but they do obtain a lower limit, $i > 57°$. Comparing the mass of the O star, $M_{\rm O} = 29 \pm 4$M$_\odot$, derived from single star evolutionary models (Schaerer et al. 1997), with $M_{\rm O} \sin^3 i$ they find $i = 65 \pm 8°$. The inclination has also been derived from a series of polarization measurements by St-Louis et al. (1987) using the method of Brown et al. (1982). In this method the radiation is assumed to be scattered from a spherical envelope around the WR star which gives rise to phase-dependent polarization variations. The amplitude of the variations can be used to derive the inclination. (See also the discussions in § 3.1 and § 8.3.2.) St-Louis et al. found $i = 70°$ but used the orbit of Moffat et al. in their analysis. Schmutz et al. have reanalysed the polarization measurements using the new orbit, and ultimately derive a similar value for the inclination, $i = 68°$. However, the most significant point of Schmutz et al.'s detailed discussion is that the polarization measurements do not, in fact, provide a serious constraint on the inclination.

7.3.2 The IUE orbit

The radial velocities of γ^2 Vel were derived using the cross-correlation method described in § 6.2. The *IUE* short-wavelength spectrum was compared against the library of O-type stars, and found to give the strongest correlation against stars of mid-to-late O spectral type, e.g., HD 49798, sdO6; HD 91824, O7 V and HD 209975, O9.5 Ib (spectral types taken from Howarth et al. 1997). HD 9546, O8 was finally chosen as the primary template for its symmetrical and relatively sharp cross-correlation profile. After considerable experimentation with the spectral masks and other measurement parameters a number of single-line orbital solutions were derived for the O star. The solutions with the smallest residuals gave $K_{\rm O} \sim 35$ km s^{-1} and $e \sim 0.4$, with σ typically 15 km s^{-1}.

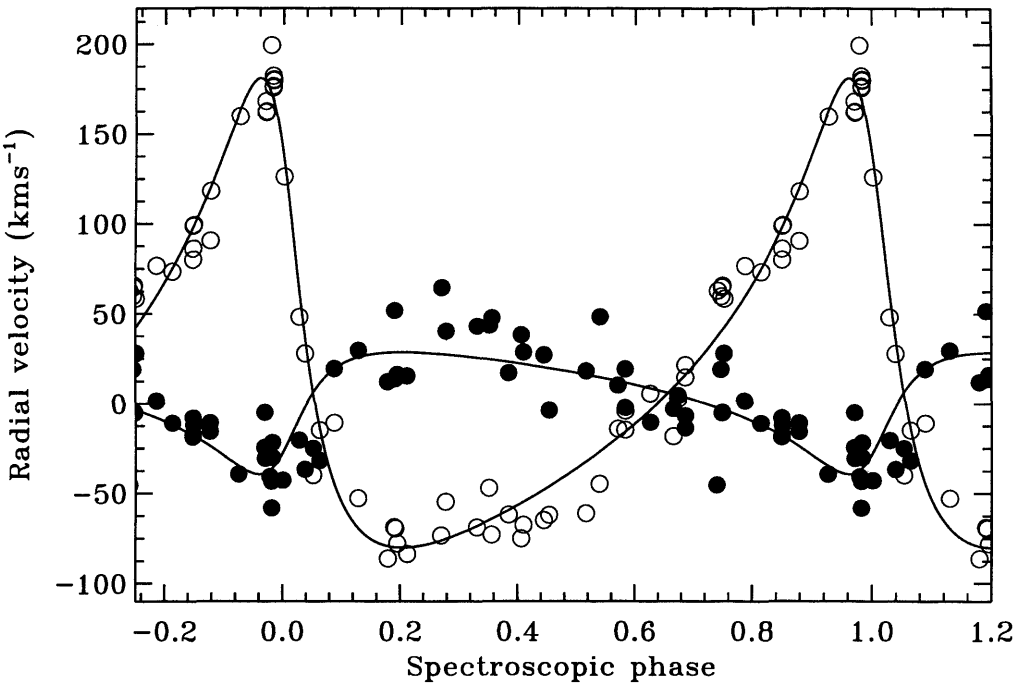

Figure 7.4: The *IUE* orbit of γ^2 Vel from a representative double-lined solution. The O star (*filled circles*) is treated as the primary. The phases are spectroscopic, measured from periastron passage. See the text for details.

The spectra of γ^2 Vel were also cross correlated against archival *IUE* spectra of single WC stars. WR57 and WR90, both WC7, gave useful correlations but the strongest was with WR135, WC8, which matched γ^2 Vel both in spectral type and terminal velocity. Again a number of solutions were derived using different masks and measuring techniques. The cross correlation function was broad but the peak gave a variation of with $K_{\rm WR} \sim 130$ km s^{-1}, $e \sim 0.5$ and with $\sigma \sim 17$ km s^{-1}. Two of the best single-line measurements were combined into a double-lined solution, which is shown in Figure 7.4. To place the velocities on a near absolute basis the measured velocities were corrected for the stellar and interstellar velocities of τ Sco, +2 and −8 km s^{-1} respectively (Stickland & Lloyd 1995), and for the interstellar velocity of γ^2 Vel of +12 km s^{-1}, derived from measurements of the Ca I K line and the Na I D lines giving 14 km s^{-1} and 11 km s^{-1} respectively (Wallerstein et al. 1980).

It is satisfying to note that the amplitudes and eccentricity are consistent with the

Table 7.3: The orbital elements of γ^2 Vel

	O	WR
P (days)	78.53±0.01	
K (km s^{-1})	38±2	122±2
e	0.326±0.01	
ω	68±4	248±4
T_0	2450120±2	
i	65±8	

Orbital elements taken from Schmutz et al. (1997)

more reliable solution of Schmutz et al. (1997) and they also support the low amplitude found for the O star in the first attempt at the *IUE* orbit by Stickland & Lloyd (1990). The agreement on $K_{\rm O}$ between this solution and that of Schmutz et al. is probably due to the heavy smoothing applied to the spectrum prior to cross correlation, which removed the slopes that troubled the previous optical measurements. The agreement on $K_{\rm WR}$ is less good, and there is some internal inconsistency in the determination of e from the two components in the *IUE* solution. It was also noted that when the more recent *IUE* data were added to the solution the errors became far worse. For the WR star this appears to be random but in the case of the O star it seems to be due in part to a general increase in velocity relative to the earlier data. Such systematic differences point to long term changes in the spectra of the system and mirrors the comments of Schmutz et al. who also noticed a difference between the data for the two years of their observations.

7.3.3 Phases

The orbit of γ^2 Vel is very eccentric and the orientation of the line of nodes leads to a complex relationship between the spectroscopic phases and the cardinal photometric points. In eccentric systems the precise definition of superior conjunction of the O star, defined as photometric phase zero, $\Phi = 0.0$ or primary minimum, is a function

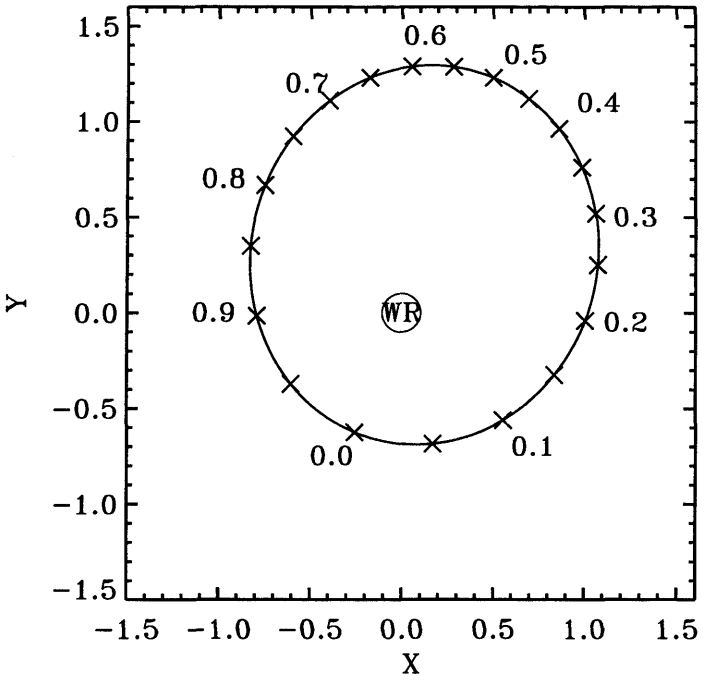

Figure 7.5: The orbital plane of γ^2 Vel showing the relative positions of the components at specific phases. The observer is in the $-Y$ direction.

of the orbital parameters and the inclination. In circular systems inferior conjunction corresponds to $\Phi = 0.5$, and the quadratures to $\Phi = 0.25$ and 0.75 but in eccentric systems this is not the case. As the photometric phases, other than $\Phi = 0.0$, convey no particular meaning it has been decided to use the spectroscopic phases in describing the variation although what happens is basically a photometric phenomenon. A plot of the orbital plane of γ^2 Vel is given in Figure 7.5 showing the motion of the O star around the WR component. It should be remembered that the phases used by St-Louis et al. in the comparison of their spectra were photometric $\Phi = 0.0$, and 0.5. Although $\Phi = 0.5$ was adopted as nominal inferior conjunction, i.e. O star in front, the line joining the two stars actually lies at $\sim 45°$ to the line of sight (see Figure 7.5).

The orbit of γ^2 Vel leads to another minor complexity which should be mentioned. At the conjunctions of the O star, that is primary and secondary minimum, the projected distance between the O star and the WR star is a minimum, but these times do not

Table 7.4: Important phases in the γ^2 Vel orbit

Event	Spectroscopic Phase ϕ	Photometric Phase Φ
Superior conjunction of O star	0.62	0.00
Quadrature	0.86	
O star at $L = 0$	0.90	
Inferior conjunction of O star	0.03	0.41
Minimum L distance	0.04	
Photometric $\Phi = 0.5$	0.12	0.50
O star at $L = 0$	0.21	
Quadrature	0.27	
Maximum L distance	0.58	

correspond exactly to the furthest and closest points of the O star along the line of sight. These points have been determined by solving for L_{max} using equation 5.2. The phases of conjunctions and quadratures (maximum projected separation of the components) have been determined using the definition of the impact parameter d, (Eqn. 5.3). The important phases are given in Table 7.4.

7.4 UV luminosity ratio

The luminosity ratio of the components has been investigated using the dilution of the emission lines by the O-star continuum. The dilution has been measured by comparing the strengths of the lines, measured in terms of equivalent widths and peak intensities, relative to those of single WC6-8 stars. Equivalent width measurements are a 'true' measure of line strength but in these stars they are particularly difficult to make, especially at high resolution. The line shapes differ from star to star depending on the effects of blending and line width, and the edges of the line are usually not clearly defined. On the other hand peak intensity is a simple and repeatable measure but it is one dimensional and does not contain any width information. Both measures are susceptible to errors in the continuum level but as the same rectifying process was

used for all spectra this problem should be minimised.

The ratio of equivalent widths $R_{\rm W}$ and peak intensities $R_{\rm I}$ are calculated in the sense $R_{\rm W} = W_{\rm star}/W_{\gamma{\rm Vel}}$ and $R_{\rm I} = I_{\rm star}/I_{\gamma{\rm Vel}}$ so the luminosity ratio

$$L_{\rm O}/L_{\rm WR} = R - 1$$

and the magnitude difference

$$\mathrm{m(O)} - \mathrm{m(WR)} = -2.5\log(R-1)$$

The ratio of equivalent widths shown in Figure 7.6 cover the range 0.4 – > 8 with considerable variation between different lines and for different stars. Apart from C III λ2297 the lines from the long-wavelength region, $\lambda > 2000$ Å, are particularly weak and give unreliable values, although those from WR135 (WC8) are the most consistent. The stronger lines showing the largest scatter are C IV λ1550, O IV λ1342 and He II λ1640. Part of this variation must be due to errors of measurement but

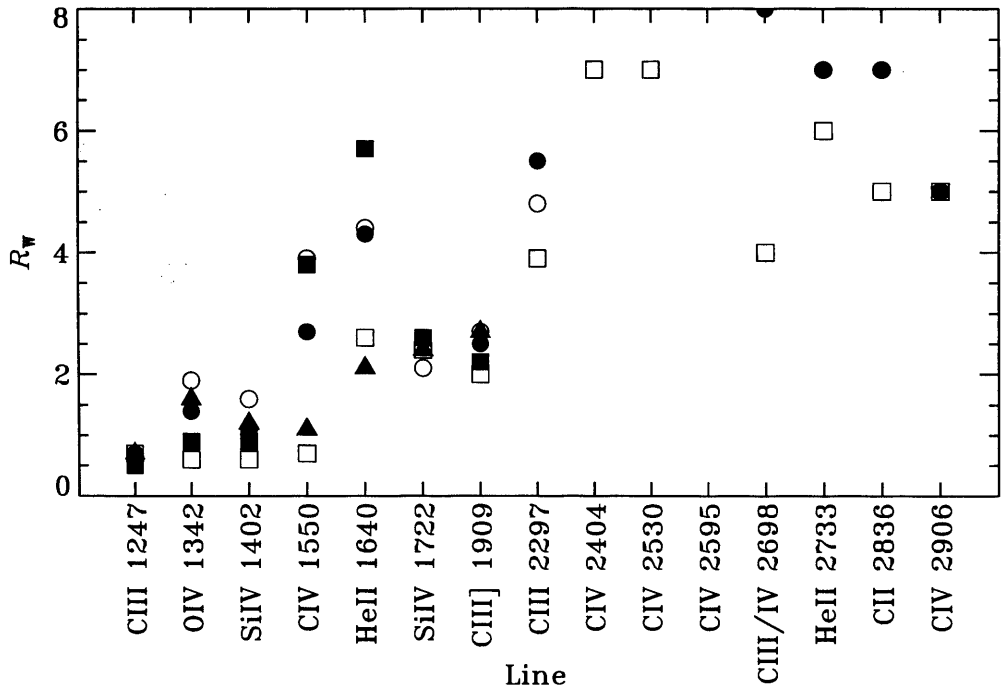

Figure 7.6: The ratio of the equivalent widths of major lines in WR14 WC6 (*filled square*), WR23 WC6 (*open circle*), WR57 WC7 (*filled triangle*), WR90 WC7 (*filled circle*) and WR135 WC8 (*open square*), relative to γ^2 Vel. See the text for details.

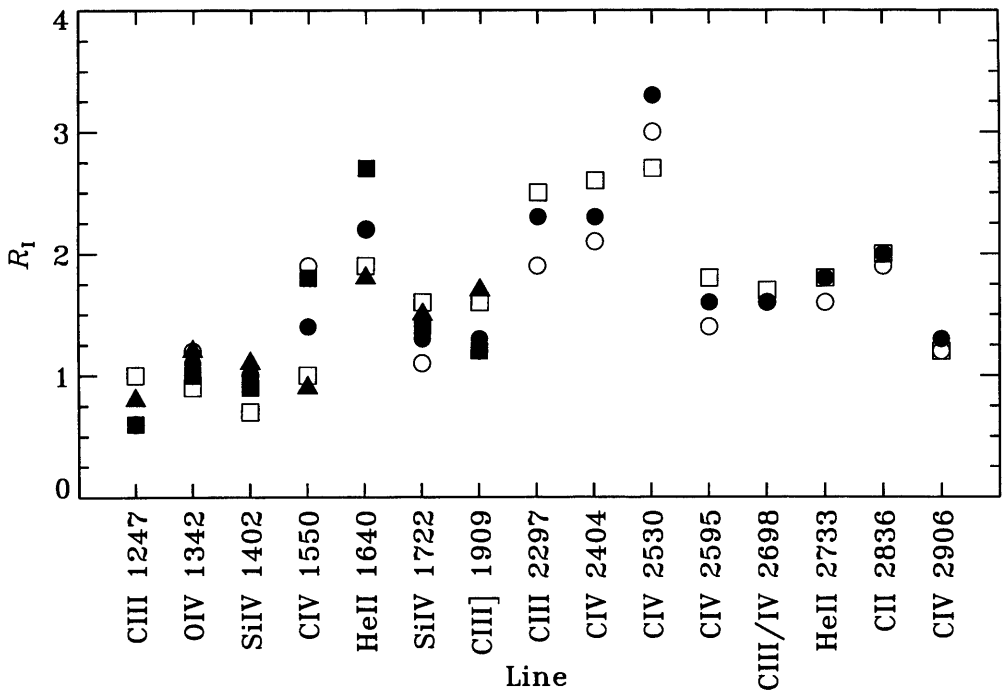

Figure 7.7: The ratio of the peak intensities of major lines in WR14 WC6 (*filled square*), WR23 WC6 (*open circle*), WR57 WC7 (*filled triangle*), WR90 WC7 (*filled circle*) and WR135 WC8 (*open square*), relative to γ^2 Vel. See the text for details.

the range is so large it is probably dominated by natural variation between stars. The value of C IV λ1550 is also contaminated by the contribution from the O-star emission line and the C III λ1247 line is blended with the N V λ1243 emission from the O star, which is why it appears anomalously strong. The O star is not expected to make a significant contribution to any of the other lines. The remaining lines from the short-wavelength region and C III λ2297 show much better internal consistency, but generally poor agreement. The O IV λ1342 and Si IV λ1402 lines average $R_W \sim 1$ implying that the O star continuum contributes nothing, which cannot be correct. The Si IV λ1722, C III] λ1909 and C III λ2297 show good internal consistency but disagree by a factor of ~ 2, and suggest $L_O/L_{WR} \sim 1 - 4$, or $\Delta m \sim 0 - 1.5$ mag.

In contrast to the equivalent width measurements the ratio of peak intensities, shown in Figure 7.7, have much less variation. The general pattern of the ratios is similar to Figure 7.6 and the same comments apply. The R_I values for the weak lines in the

long-wavelength region are far less variable than the equivalent width measurements but is is not clear that these are any more meaningful. The lines generally show better internal consistency; the largest being C IV λ1550 with a range of a factor of 2, and are on average lower than $R_{\rm W}$. The mean value of $R_{\rm I} \sim 2$, even for the strongest lines, suggests that the components are about equal, which is at odds with previous determinations. However, these single numbers conceal significant variation.

7.5 Terminal velocity

Variations in the line profiles cause changes in the measured terminal velocity. During the first half of the orbit, $0.62 < \phi < 0.92$, as the O star moves from the back to the front of the system, many lines show some variability which may or may not be reflected in v_∞. Around inferior conjunction, $0.00 < \phi < 0.15$, the strong P-Cygni absorptions of the O star appear and generally dominate the blue edge of the profile. During the second half of the orbit, $0.22 < \phi < 0.52$, several of the weaker absorptions show a slight shift to less negative velocities. Following Prinja et al. (1990) the terminal velocity has been determined from the blue limit at zero intensity of saturated lines, $v_{\rm black}$, and from the blue edge of the deepest part of the line in flat-bottomed unsaturated lines. For the round-bottomed unsaturated lines the velocity of the deepest part of absorption has been used. In the case of C IV λ1548 the line shows an additional feature on the blue edge which is visible over a wide range of phases (see Figure 7.9). Between superior and inferior conjunction this feature deepens and is eventually lost in the bulk of the saturated P-Cygni absorption. The Si IV λ1393 line shows similar behaviour but it does not appear so early and does not form a sharp lip, so is impossible to measure until it becomes saturated. The N V λ1238 line of the O star is clearly visible at all phases but the profile is complex and variable.

The velocities, measured at two phases (ϕ = 0.62 and 0.03) around superior and inferior conjunction, corrected to the systemic velocity are given in Table 7.5. In general the velocities are in fair agreement with those of Prinja et al., except for C II λ1335 where a different rest wavelength has been used. The value used here for the blend is taken from Morton (1991). The terminal velocity of the WR component is

Table 7.5: Measured terminal velocities in γ^2 Vel from IUE

Line	ϕ=0.62	edge	ϕ=0.03	edge
C IIIλ1175	−1578		−1782[1]	
N Vλ1238			−1963[2]	
C IIIλ1247	−1119		−1239	
C IIλ1335	−1281		−1482[2,3]	
Si IVλ1393	−1493		−1988[2]	
Si IVλ1402	−1465		−1315[4]	
C IVλ1548	−1526	−2146	−1545[1]	−2146
C III] λ1909	−1259		−1290	
C IIIλ2297	−1170		−1340	

1 multiple components

2 measured at $\phi = 0.08$

3 sharp feature on blue edge of line

4 reduced by emission

taken from the C III λ1175, Si IV λ1393, 1402 and C IV λ1548 lines at $\phi = 0.62$, which give v_∞(WR) = 1520±50 km s^{-1}. It compares with terminal velocities of 1520±200 km s^{-1} from the [Ne II] 12.8-μm line (Barlow et al. 1988), 1450±190 km s^{-1} (Eenens & Williams 1994) derived from He I lines observed at 1- and 2-μm, 1551 km s^{-1} from the UV lines (St-Louis et al. 1993), and $v_{\rm black}$(C IV) = 1415 from Prinja et al. (1990). The velocities of the other lines are generally smaller and more scattered but when they are included the terminal velocity is reduced to 1390±170 km s^{-1}. The higher figure is also more consistent with the velocity of the sharp C II λ1335 feature at $\phi \sim 0.08$. The O-star velocities are most clearly defined at $\phi \sim 0.08$ and they are measured as noted in the table. Using the velocities from the N V λ1238, Si IV λ1393 and C IV λ1548 lines gives v_∞(O) = 2030±100 km s^{-1} which is rather less than the values given by Prinja et al. and St-Louis et al. (1993), although this lower velocity is more in keeping with the values of single O8 III stars (Prinja et al. 1990, Howarth et al. 1997).

Prinja et al. find a velocity of −2370 km s^{-1} for the feature on the blue wing of the

C IV absorption on a spectrum they believed was taken near inferior conjunction. The spectrum was first shown and phase calculated by Kondo et al. (1982) but appears to be based on some misunderstanding of spectroscopic T_0. The spectrum was taken at ϕ = 0.92 near quadrature, and close to maximum negative velocity of the O star, which may explain the large difference. In Figure 7.9 the velocity of this feature clearly changes between quadrature and inferior conjunction. St-Louis et al. find v_∞(O) similar to Prinja et al. but their measurements are taken from difference spectra and there is some suggestion that they correspond to v_{edge}.

7.6 System parameters

For the purposes of modelling, some parameters will be assumed but others will be used for guidance, or to inform later discussion. The parameters describing the shock zone are a complex combination of orbital and stellar parameters. The mean orbital velocity,

$v_{\rm orb} = (K_{\rm O}+K_{\rm WR})/\sin i$ = 170 km s^{-1}

with $K_{\rm O}$ and $K_{\rm WR}$ taken as 38 and 122 km s^{-1} respectively, and $i = 70°$. The terminal velocity is taken as v_∞(WR) = 1450 km s^{-1} (Eenens & Williams 1994) and the mass loss rate, $\dot{M}_{\rm WR} = 3 \times 10^{-5}$ M$_\odot$ yr^{-1}, is taken from Schaerer et al. (1997). Combined with the terminal velocity of the WR wind, the offset angle of the cone, by equation 5.6, $\delta = 7°$. For O8 stars Lamers & Leitherer (1993) give mass-loss rates of (0.5 - 1.7)$\times$10^{-6}M$_\odot$ yr^{-1} and v_∞ = 2000 - 2500 km s^{-1}. Howarth & Prinja (1989) find $\dot{M}$ $\sim$ 1$\times$10^{-6}M$_\odot$ yr^{-1} for late O-type stars and Howarth et al. (1997) find $v_\infty \sim$ 2200 km s^{-1} for O8 III stars. Adopting v_∞(O) = 2030 km s^{-1} derived earlier, and $\dot{M}_{\rm O}$ = 1 $\times$ 10^{-6}M$_\odot$ yr^{-1} for the O star, equation 3.1 yields a momentum ratio, $\mathcal{P}$ = 21. By equation 5.4 the stagnation point, x_0 = 0.82, and by equation 5.5, the opening angle of the cone, $\theta = 40°$.

As the orbit is eccentric both the separation between the two components and the orbital velocity will change, approximately by a factor of 2, which will change some aspects of the shock zone. In practice as far as the modelling is concerned these

differences are small and have little impact on most of the profiles. The largest changes affect the visibility of the O star, which is dependent on i and θ, of which the latter is probably the least reliable parameter. Following the earlier discussion (§ 7.1) it is assumed that the shock zone is present at all phases in approximately the same position relative to the two components and that the O-star wind does not collapse.

7.7 Line variations

In common with the previous analyses of this system it is found that the lines which show the largest variation are the resonance and low excitation lines, and not the high excitation lines. Also, it is found that the reproducibility of the features, even on spectra that were taken some years apart, is extremely good, supporting the conclusion of St-Louis et al. (1993). Each line showing selective absorption is described in detail in this section and in the next the results of the profile modelling are shown. The plots showing the variations contain, typically 4 spectra, merged together at each phase. In a relatively large system such as γ^2 Vel the WR wind is able to reach close to the terminal velocity within the orbit of the two components. For lines formed within the system selective absorption can take place across the whole velocity range of the line. Lines formed outside the orbit of the stars will show variation only in the P-Cygni absorption. The selective absorption by the wind can, at most, remove only the contribution of the O-star which for the most part is effectively continuum. However in the strong lines of the O star the effect will be more complicated. Saturated wind-absorption lines may on the one hand remove all the continuum and O-star emission but on the other make no difference if the line is already absorbed by the O-star wind. Given the luminosity ratio $L_{\rm O}/L_{\rm WR} \sim 4$ the wind might be expected to absorb ~ 0.8 of the combined pseudo continuum, or possibly as much as twice this in the strong O-star emission lines of N V and C IV.

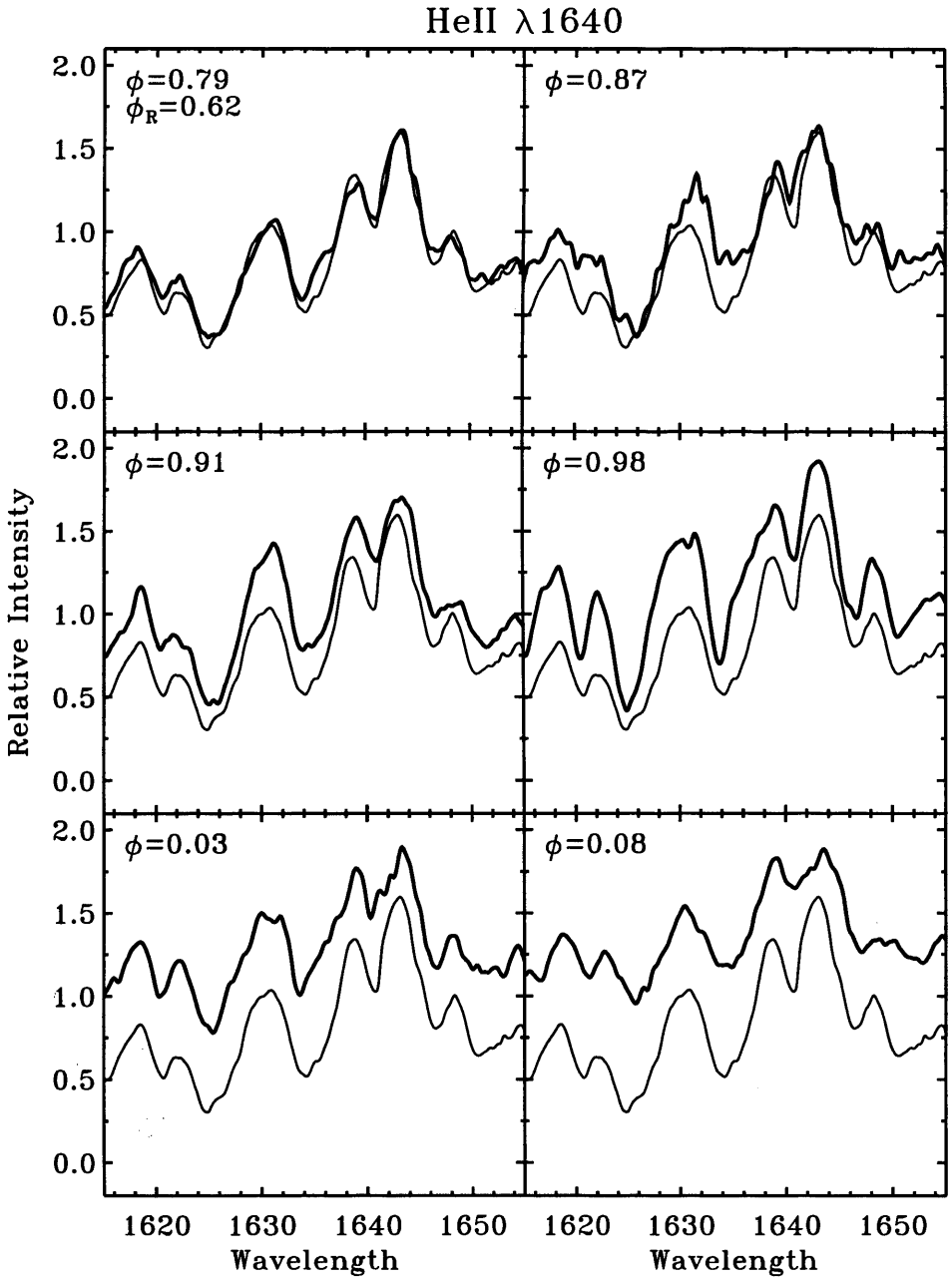

Figure 7.8: The complex region around He II λ1640. Twelve orbital phases are shown, six in this figure and six in the next. The sequence begins at superior conjunction of the O star, i.e. behind the WR star, which is used as a reference phase, $\phi_R = 0.62$, and this profile is shown in all the panels (*thin line*). The profiles at other phases (*thick lines*) are plotted in each panel over the reference profile. The phases used are spectroscopic phases (see § 7.3.3 and Table 7.4). To aid comparison the spectra have been slightly smoothed ($\sigma = 0.2$ Å) and the gaps have been filled. See text for details.

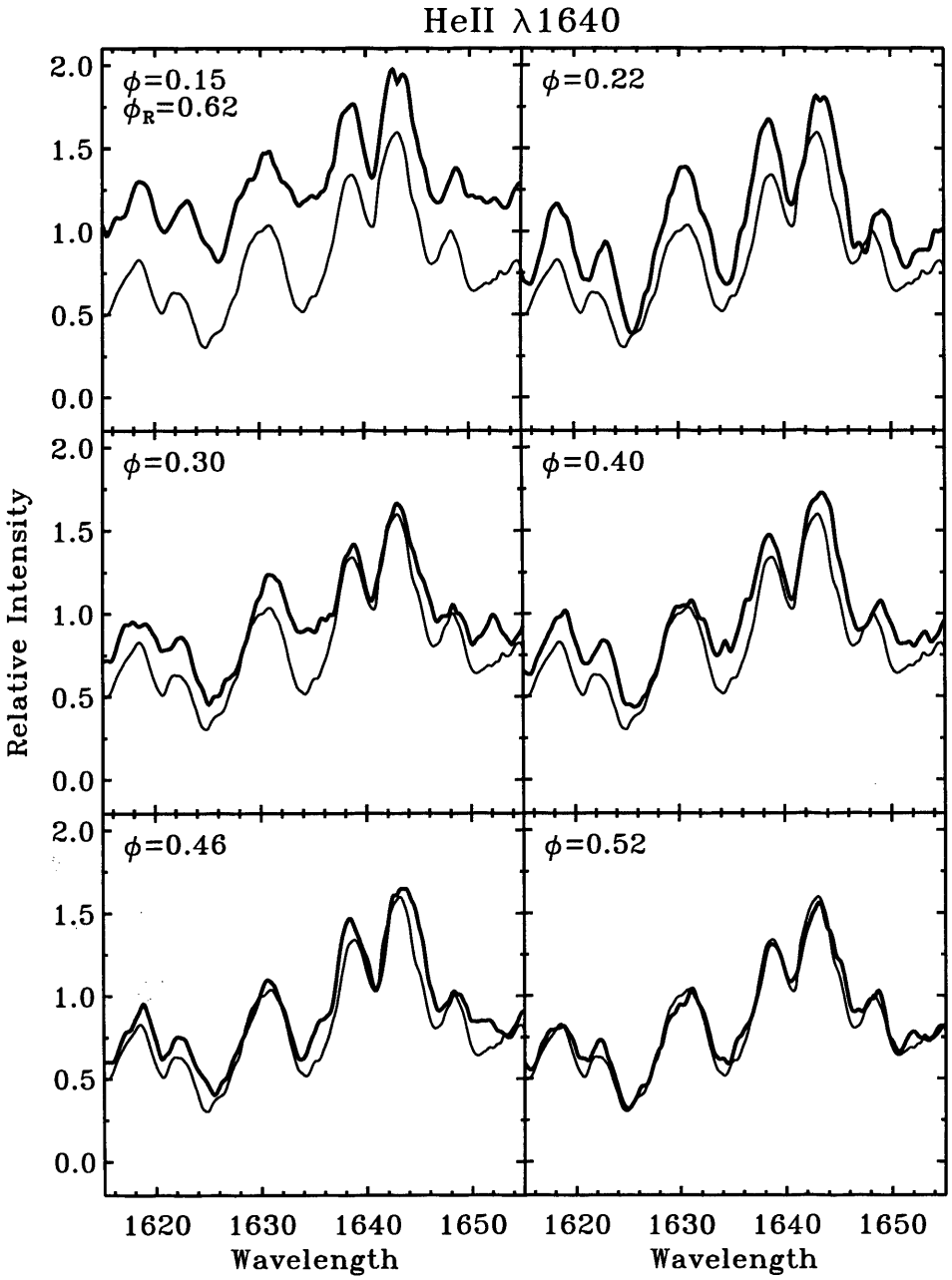

Figure 7.8: continued. The complex region around He II λ1640 showing the six later phases. See the text for details.

7.7.1 He II λ1640

The region around the He II λ1640 line is very complicated and possibly contains lines due to C III and C IV (Hamann et al. 1992) as well as O III, O IV, Si IV and Fe IV(Willis et al. 1986). When modelling this region Hamann et al. included the C III λ1625 and λ1645 lines although it is not clear that they are particularly strong contributors. The line is very different to the single strong emission and P-Cygni absorption seen in WN stars and shows a double-peaked structure due either to a superimposed absorption or other contributing emission lines. The feature at $\sim$ 1630 Å is not fixed in wavelength between different single WC stars but is bounded by absorptions depending on the terminal velocity of the wind. It is therefore unlikely to be a single line but is probably composed of different sections of pseudo continuum and emission.

The starting point for the variation is taken as superior conjunction of the O star, when it should suffer (close to) maximum absorption. The variation (Figure 7.8) begins slowly ($\sim \phi = 0.79$) with a filling in of the absorption components and by quadrature ($\phi = 0.86$) the emission lines have begun to increase. During the second quadrant the emission continues to increase and the P-Cygni absorption narrows from the red edge. During the passage through inferior conjunction ($\phi = 0.98$ to 0.09) the absorption lines fill in dramatically, reaching a minimum $\sim \phi = 0.07$, but then quickly deepen. By quadrature ($\phi = 0.27$) the Fe IV pseudo continuum has dropped significantly although the peaks of the emission $\sim$ λ1640 show only a small change. Around quadrature the P-Cygni absorption fills in slightly and the red edge eats into the emission showing the reverse of its earlier behaviour. During the last quadrant the emission shows further small reductions but the absorption continues to deepen to $\phi = 0.56$. Superimposed on this general trend are significant but complex variations in both the emission peak and P-Cygni absorption. Around superior conjunction ($\phi = 0.56$ to 0.73) there are only very minor variations.

As the He II λ1640 line is superimposed on the Fe IV pseudo continuum it is difficult to disentangle the variations of the two. However, the variation in the red P-Cygni absorption edge up to $\phi \sim 0.98$ is qualitatively what might be expected of selective absorption and occurs before the main change in the level of the pseudo continuum.

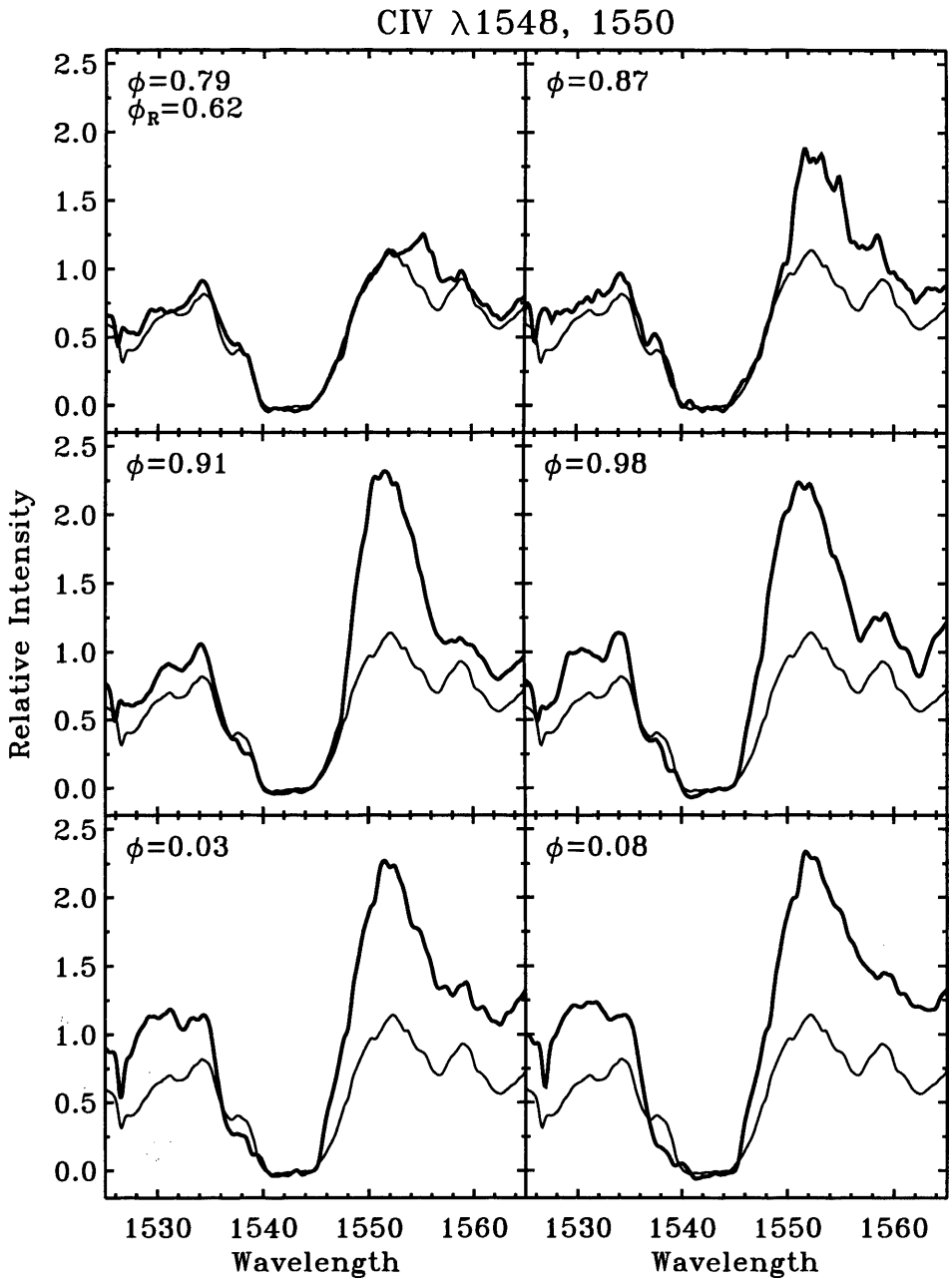

Figure 7.9: The region around the C IV λ1548, 1550 P-Cygni profile. The weak C IV interstellar lines can be seen as notches at the rest wavelength in the profiles of the strong emission lines. Other details are as Figure 7.8.

The maximum change in intensity is $\sim$ 0.7 of the pseudo continuum in the P-Cygni absorption but only about half of that in the emission peak.

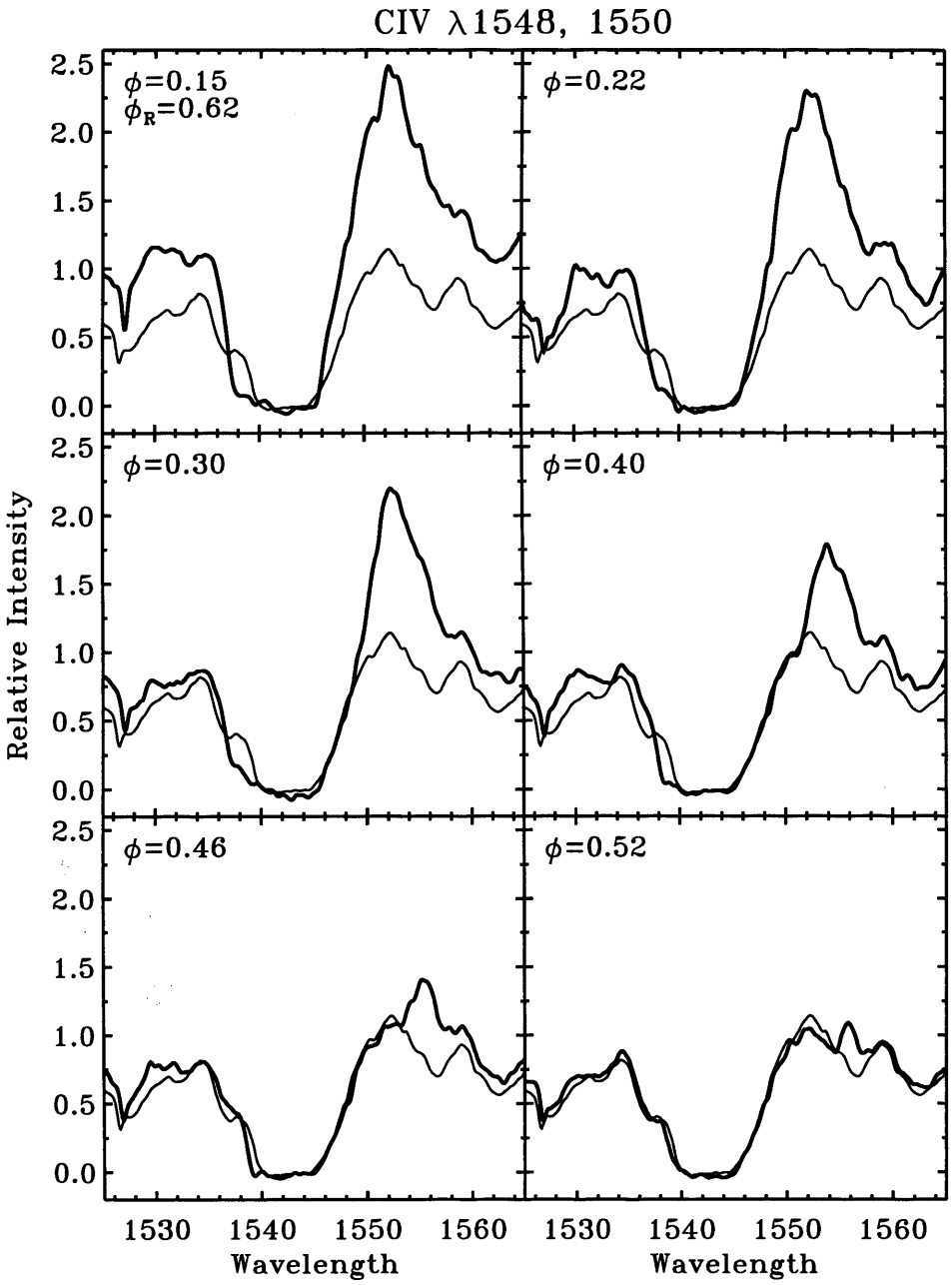

Figure 7.9: continued. The region around the C IV λ1548, 1550 P-Cygni profile showing the six later phases. Other details are as Figure 7.8.

7.7.2 C IV λ1548, 1550

The region around the C IV λ1548, 1550 doublet (Figure 7.9) is rather less confused than around He II λ1640 but it does lie just within the Fe IV pseudo continuum. At superior conjunction the emission line is barely visible above the continuum but the P-Cygni absorption is saturated and shows a stepped structure on the blue wing. The emission line shows a clear and progressive increase through the first quadrant and reaches maximum intensity at $\phi \sim 0.91$, just after quadrature. The intensity remains almost constant, with only minor variations, until $\phi \sim 0.30$, when it shows a strong decline. The maximum change in intensity is ~ 1.3 of the pseudo continuum. During the passage through inferior conjunction, although the intensity of the emission changes little, the width shows a progressive increase as the emission eats into the P-Cygni absorption, reaching a maximum around inferior conjunction, before slowly receding. The other significant variation takes place on the blue wing of the P-Cygni absorption. At superior conjunction the line shows a stepped structure which becomes progressively deeper reaching a maximum at $\phi \sim 0.15$ when the P-Cygni absorption is approximately rectangular. During the later phases the line returns, rather unevenly, to its original shape, but the feature is still visible to $\phi \sim 0.40$. The O8III companion is also expected show the C IV λ1548, 1550 doublet in emission with a possibly saturated P-Cygni absorption, and the variations on the blue wing of the line are consistent with its increasing visibility.

7.7.3 Si IV λ1393, 1402

The behaviour of the Si IV λ1393, 1402 doublet (Figure 7.10) is broadly similar to C IV λ1548, 1550, although there are significant differences of detail. The separation of the two components and the terminal velocity of the WR wind are such that the λ1393 emission lies close to the λ1402 P-Cygni absorption edge, which produces a saddle region between the two P-Cygni absorption components.

At superior conjunction the emission line is barely visible above the continuum but unlike C IV there is no feature on the blue wing of the P-Cygni absorption. The emission at λ1393 and λ1402 shows a clear and progressive increase through the

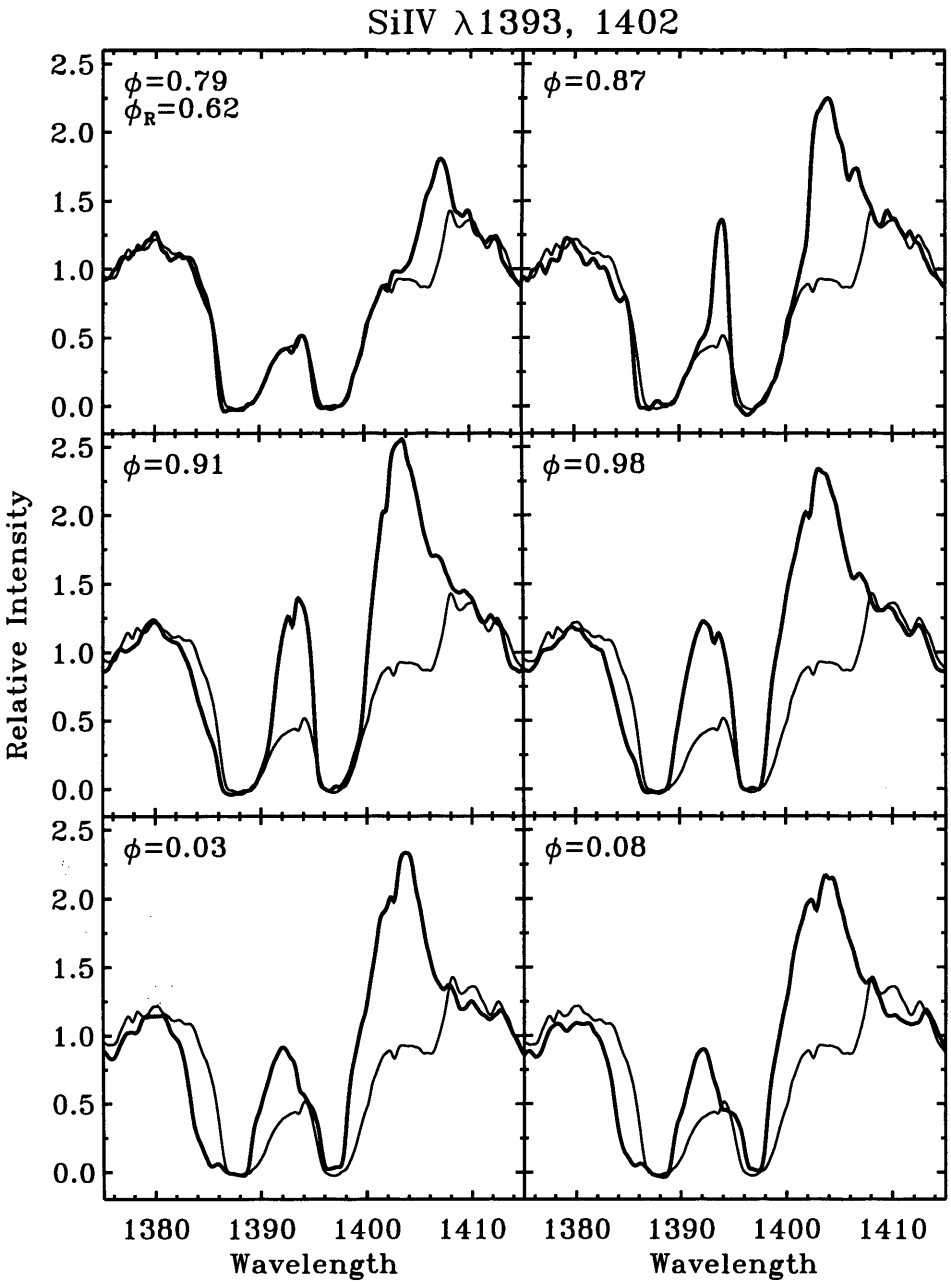

Figure 7.10: The Si IV λ1393, 1402 P-Cygni profile. See text for details. Other details are as Figure 7.8.

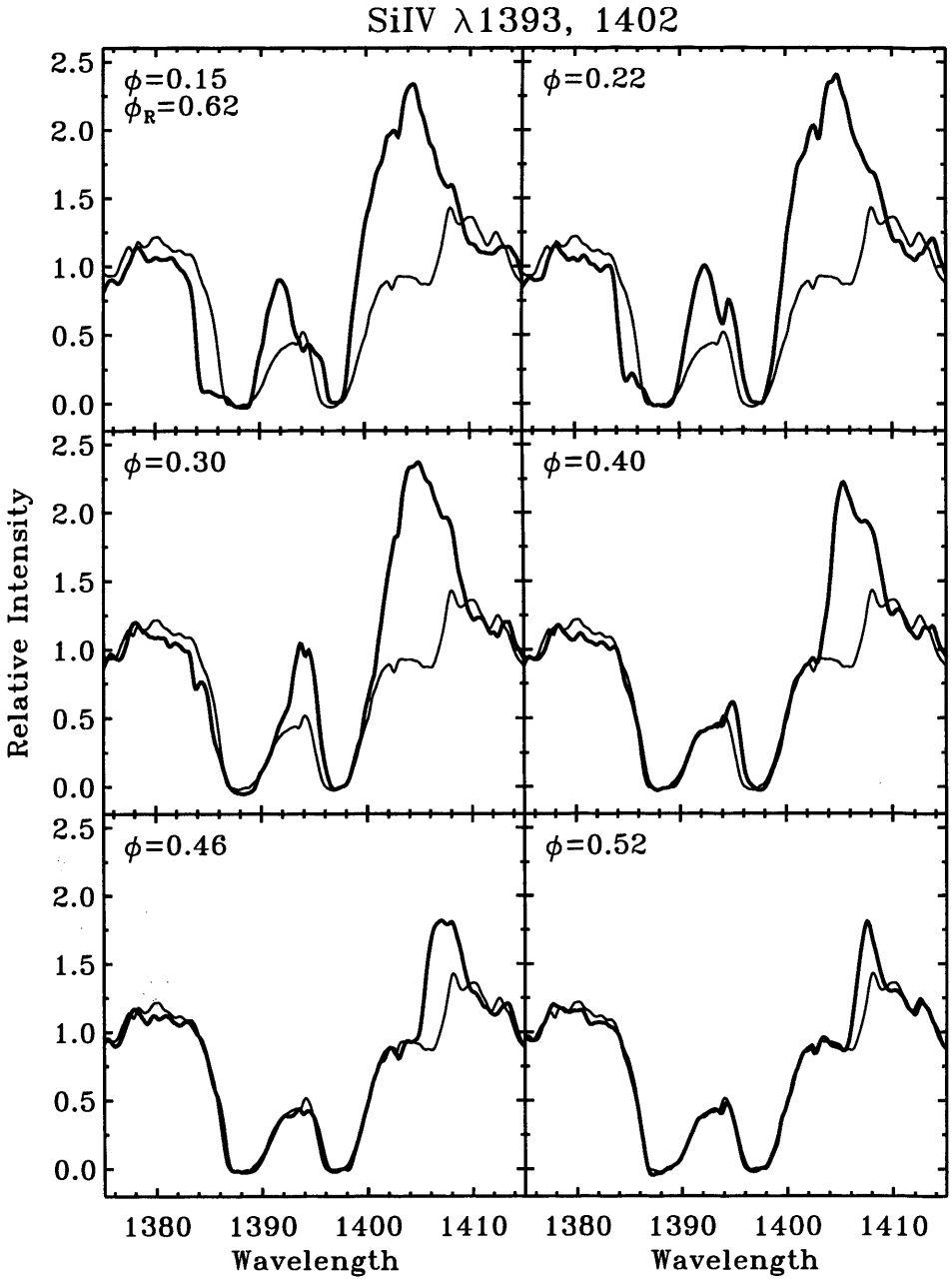

Figure 7.10: continued. The Si IV λ1393, 1402 P-Cygni profile showing the six later phases. See text for details. Other details are as Figure 7.8.

first quadrant and reaches maximum intensity at $\phi \sim 0.91$, similar to C IV, but then shows significant variation around inferior conjunction before finally falling away after $\phi \sim 0.40$. The narrowing of the P-Cygni absorption also follows the behaviour seen in C IV. The maximum change in intensity is ~ 1.6 of the pseudo continuum.

The blue wing of the P-Cygni absorption becomes extended and progressively deepens during the first half of the orbit, reaching a maximum at $\phi \sim 0.15$. The line then very quickly returns to its original profile. The O8III companion is also expected show the Si IV λ1393, 1402 doublet in absorption and is interpreted as being responsible for the variations on the blue wing of the line. The variations are weaker than those of C IV because the Si IV lines are not saturated, however, the fact that they are visible at all implies a strong wind line, and the possibility of some emission.

7.7.4 C III λ1247

The C III λ1247 line (Figure 7.11) is blended with the N Vλ1239, 1243 doublet which is a strong feature of the O-star spectrum. The C IV λ1230 UV multiplet 11.14 is present in emission in single WC stars but it is clearly not a strong contributor here. At superior conjunction the C III λ1247 line shows no emission and the P-Cygni absorption is unusually sharp (cf., C IV λ1548, 1550, Figure 7.9 and Si IV λ1393, 1402, Figure 7.10) which gives rise to the discordant terminal velocity of this line. There is also a strong absorption at $\sim$ 1234 Å which is interpreted as the P-Cygni component of the N V λ1239, 1243 line from the O star. The emission component, which is not visible as such, has filled in the C III absorption. During the orbital cycle the behaviour of the C III λ1247 emission variation is similar to what has been seen in the other lines; there is a progressive rise and fall in intensity of ~ 1.6 of the pseudo continuum. The blue edge of the N V P-Cygni profile also shows a similar variation to that seen in C IV and Si IV, but is rather more extreme. At $\phi \sim 0.91$ the terminal velocity increases dramatically and briefly, around inferior conjunction, the strength of the line nearly doubles, almost reaching saturation. At $\phi \sim 0.15$ the line weakens and develops a strong absorption edge, reminescient of the Si IV line (Figure 7.10). During the remainder of the orbit the absorption quickly returns to its original strength and

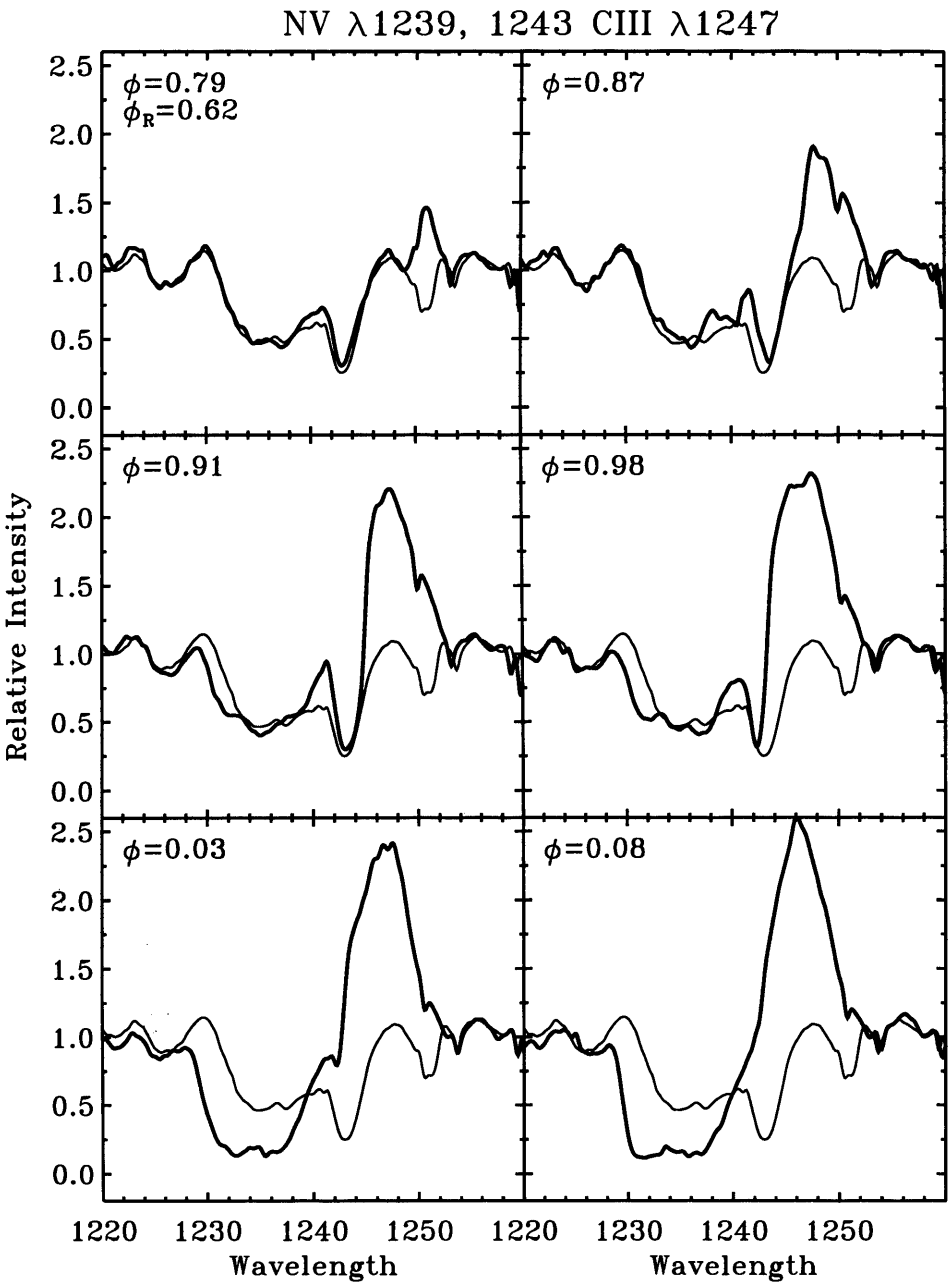

Figure 7.11: The region around the C III λ1247 P-Cygni profile with N V λ1239, 1243. The sharp absorptions are the S II λλ1250, 1253, 1259 and Si II λ1260 interstellar lines. Other details are as Figure 7.8.

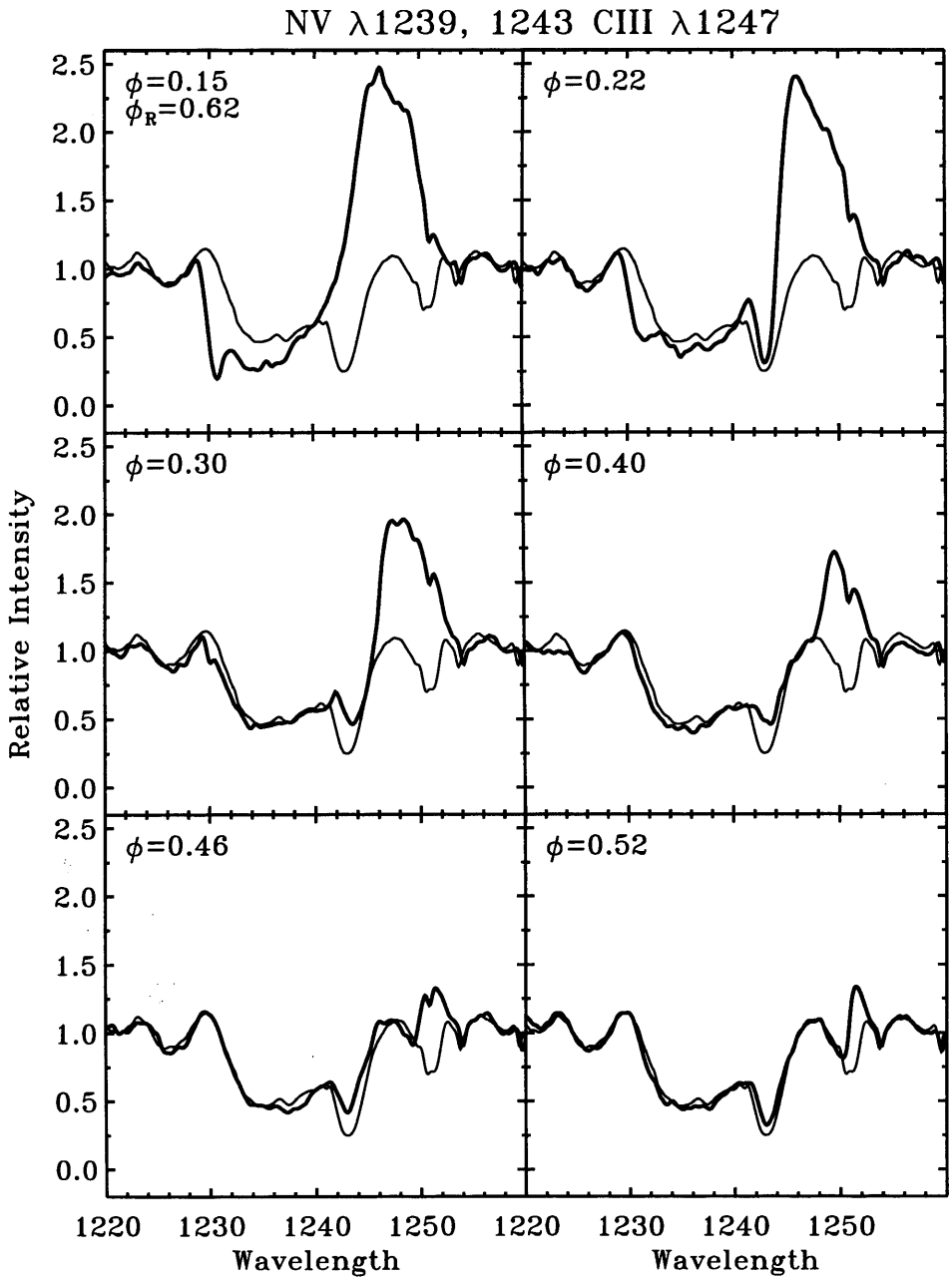

Figure 7.11: continued. The region around the C III λ1247 showing the six later phases. Other details are as Figure 7.8.

velocity. The C III λ1247 P-Cygni absorption is caught between two emissions and as expected weakenes towards inferior conjunction. However, during the passage through inferior conjunction ($\phi \sim 0.98$ to $\phi \sim 0.22$) this absorption vanishes while the strength of the C III emission changes only slightly. Either the N V emission has increased substantially, suppressing the absorption, which seems unlikely, or the absorption has decreased. It seems most probable that the line of sight at $\phi \sim 0.08$ passes along the cavity of the O-star wind which accounts for the change in terminal velocity and increase in strength of the N V absorption and also for the absence of the C III absorption. There is one final comment about the C III absorption which concerns the variation at late phases. At $\phi \sim 0.22$ the absorption return almost to its previous strength but then weakens and shows other minor variations, through quadrature almost to superior conjunction. The origin of these variations is not clear, but are probably related to the shock zone.

7.7.5 C III] λ1909

The semi-forbidden C III] λ1909 line is expected to be formed only in the wind of the WR star so there should be no confusion from the O-star wind. Other lines found in this region (Figure 7.12) include the C III λ1923 line, which is only weakly visible, and Willis et al. (1986) suggest the Fe III UV multiplet 34 lines $\lambda\lambda$1895, 1914, 1926 as possible contributors. One of the main problems with this line on the *IUE* spectra is that the peak of the emission often lies close to saturation, which results in poor signal to noise and spurious features (cf., 6.1). Despite the merging of several spectra at each phase features in the peak of the emission are unreliable.

In contrast to the resonance lines lines discussed earlier the C III] λ1909 emission is well developed at superior conjunction, and the P-Cygni absorption is relatively weak. During the first quadrant the, initially triangular, emission fills out from about the rest wavelength, unlike the other lines where it begins at the red edge, and develops an approximately rectangular profile. Around inferior conjunction the red edge of the profile briefly weakens and recovers, and the later phases are essentially a reflection of the early phases as the line returns to its original profile. The maximum change

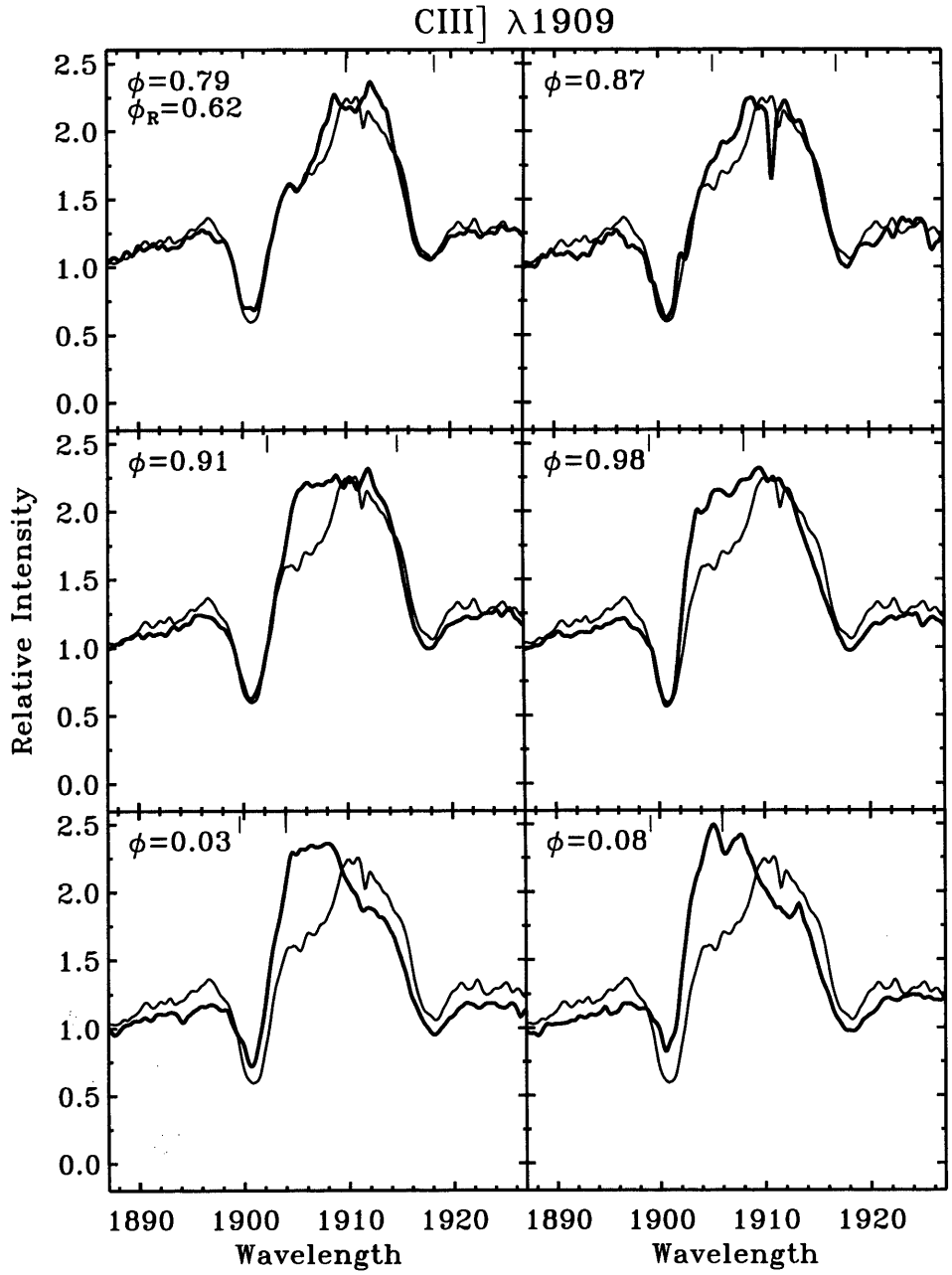

Figure 7.12: The C III λ1909 P-Cygni profile. Further details are as Figure 7.8.

in intensity of the emission is $\sim$ 0.8 of the pseudo continuum, considerably less than the other emission lines in this star.

The P-Cygni absorption remains essentially constant almost until inferior conjunction ($\phi \sim 0.98$) when it progressively weakens by a factor of about 2, by $\phi \sim 0.15$. At $\phi \sim 0.22$ the absorption quickly regains its original strength but the blue edge of the

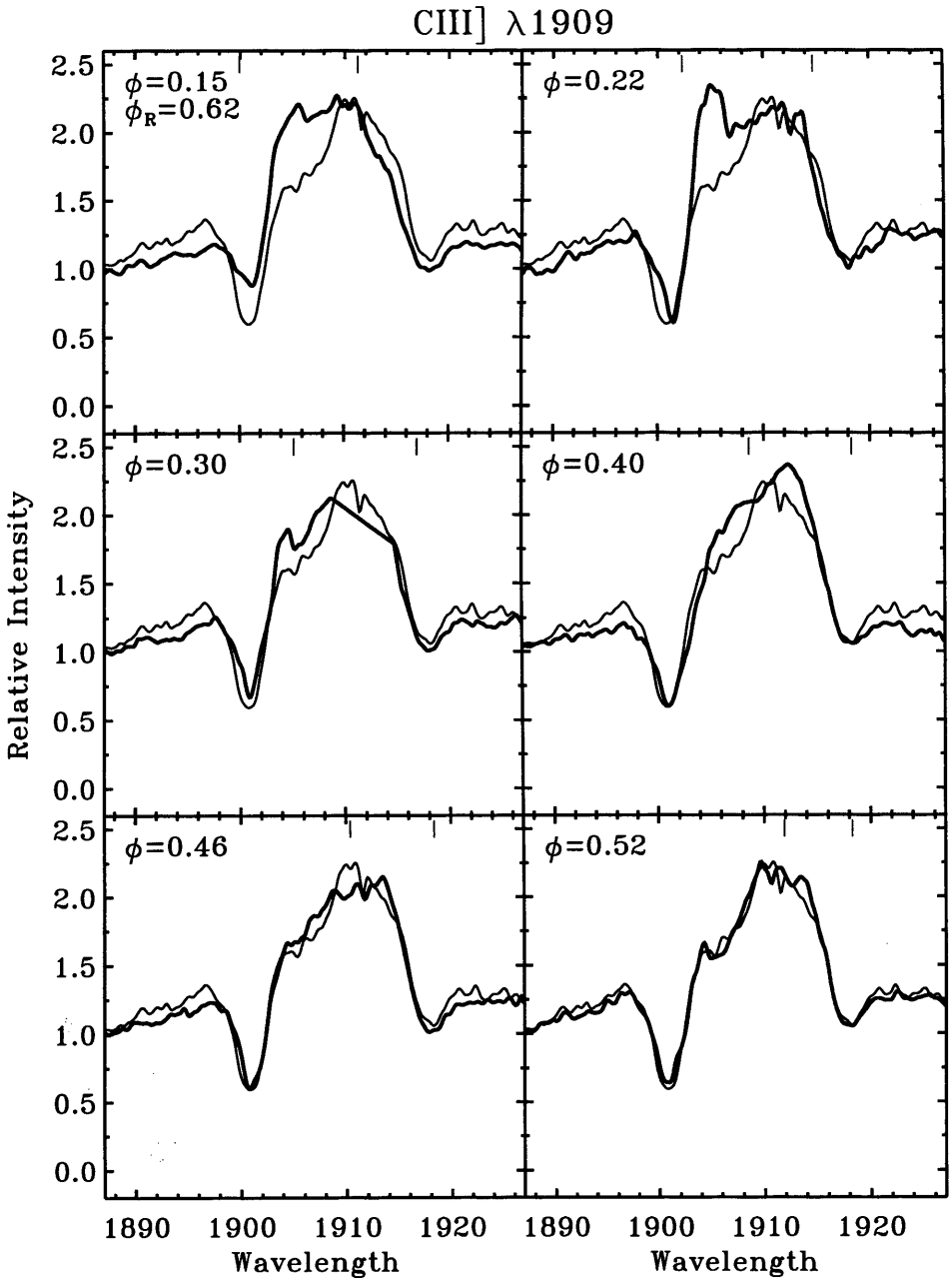

Figure 7.12: continued. The C III λ1909 P-Cygni profile. Further details are as Figure 7.8.

line is very weak, implying a lower terminal velocity. After quadrature the absorption quickly returns to its original profile and remains constant for the remainder of the orbit.

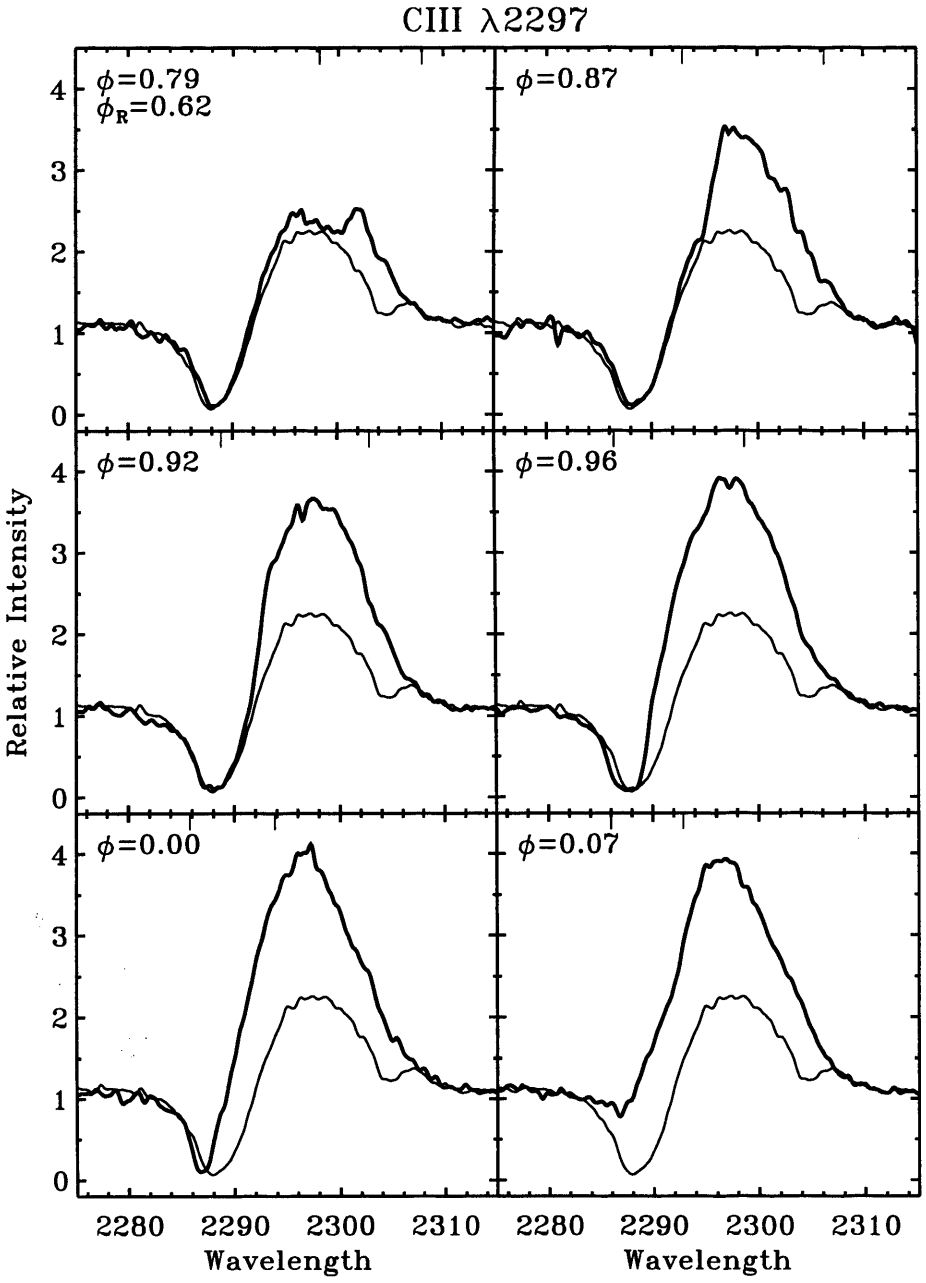

Figure 7.13: The C III λ2297 P-Cygni profile. The orbital phases are similar to those of the *IUE* short-wavelength spectra but not identical. The short vertical bars at the top of each panel show the maximum velocity of the material streaming in the shock zone. Further information is given in the text and other details are as Figure 7.8.

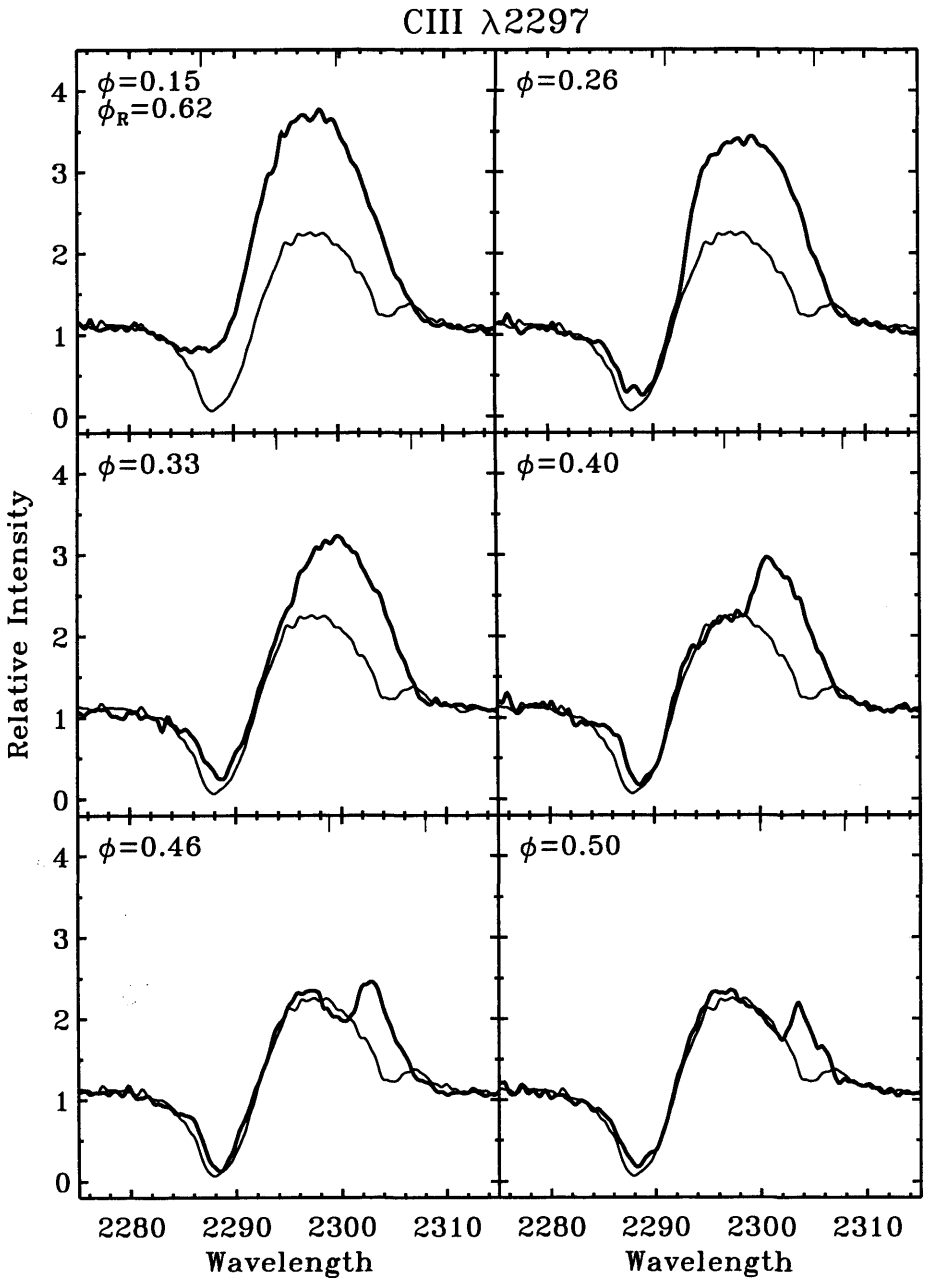

Figure 7.13: continued. The C III λ2297 P-Cygni profile showing the six later phases. Further information is given in the text and other details are as Figure 7.8.

7.7.6 C III λ2297

The C III λ2297 line (Figure 7.13) lies in a spectral region where the sensitivity of the *IUE* detectors increases substantially from blue to red, and also where interstellar absorption takes its highest toll, although that is not a particular problem for γ^2 Vel. The line of the continuum through the profile is quite strongly curved and the rectified profile is sensitive to details of the nearby continuum.

The C III λ2297 line has the strongest emission in the *IUE* range and shows substantial variations across the whole profile. At superior conjunction the emission is well formed and the P-Cygni absorption is close to saturation. In single WC stars the absorption is strongly saturated. During the first quadrant the emission increases slowly from the red edge of the profile, but then increases dramatically around quadrature. The emission continues to increase until it reaches a maximum near inferior conjunction, where it has filled in approximately half the width of the absorption. After inferior conjunction the remaining absorption component disappears briefly and the emission weakens in a reversal of its behaviour during the first half of the orbit. During the later phases the absorption shows a persistent shift to the red, as seen in some other lines. The amplitude of the variation is not constant across the line but depends on wavelength. Near the red edge the variation is relatively constant at about the level of the pseudo continuum but at the line centre it reaches nearly twice that value. Clearly such a large variation cannot be due simply the the removal of the O-star continuum.

7.7.7 C III λ1175

The line at C III λ1175 is a complex blend of some six C III lines which share the same lower level as the C III λ2297 line. The line lies at the blue limit of the *IUE* short-wavelength range where the signal to noise drops rapidly and the rectification can be unreliable. During the orbital cycle the variation broadly follows the behaviour seen in the other lines although there are striking differences between this and the C III λ2297 line. The peak intensity of the emission is reached at $\phi \sim 0.91$, near quadrature, and it weakens before reaching another maximum near the third quadrature. Around

inferior conjunction the blue edge of the absorption is pushed to higher velocities but the line does not show the variation in strength of C III λ2297. The maximum variation is $\sim$ 1.7 times the level of the pseudo continuum which is similar to that of C III λ2297.

7.7.8 C II λ1335 and O IV λ1338, 1342

The region around λ1340 Å (Figure 7.14) contains the C II λ1335 line, which is responsible for most of the absorption, the C II λ1335 interstellar lines and the O IV λ1338, 1342 P-Cygni profile. The emission appears to be due to a combination of C II λ1335 and O IVλ1338, 1342, although Hillier (1989) and Hamann et al. (1992) suggest that C II λ1335 is seen only in absorption. However, the emission is significantly to the blue of the same line in HD 152270 (see § 8.7.8).

The emission shows an irregular progression broadly following what has been seen before in the other emission lines. However, there is significant reduction in the intensity of the red edge of the line around inferior conjunction, which is not seen in other emission lines, with the exception of C III] λ1909. The apparent blue-ward shift of the emission is clearly seen relative to the C II λ1335 interstellar lines. The maximum variation is $\sim$ 1.1 of the pseudo continuum.

The absorption is dominated by C II λ1335 although there is probably some contribution from O IV. At superior conjunction, where the absorption is strongest, the line shows a slight asymmetry but is not obviously broader than C III] λ1909. The line shows the in-filling from the red associated with the increased emission, and around inferior conjunction, at $\phi \sim 0.12$ the absorption weakens by nearly half and the blue edge moves in. The behaviour is very similar to that of C III] λ1909 at the same phases. From $\phi \sim 0.08$ to $\phi \sim 0.15$ C II λ1335 shows a clear doubling of the line, with the sharp high-velocity component lying at about the terminal velocity, and then moving in by $\sim$ 100 km s^{-1}. The line quickly fills in and returns to its original strength, but then shows additional minor variations after quadrature in exactly the same way as C III] λ1909.

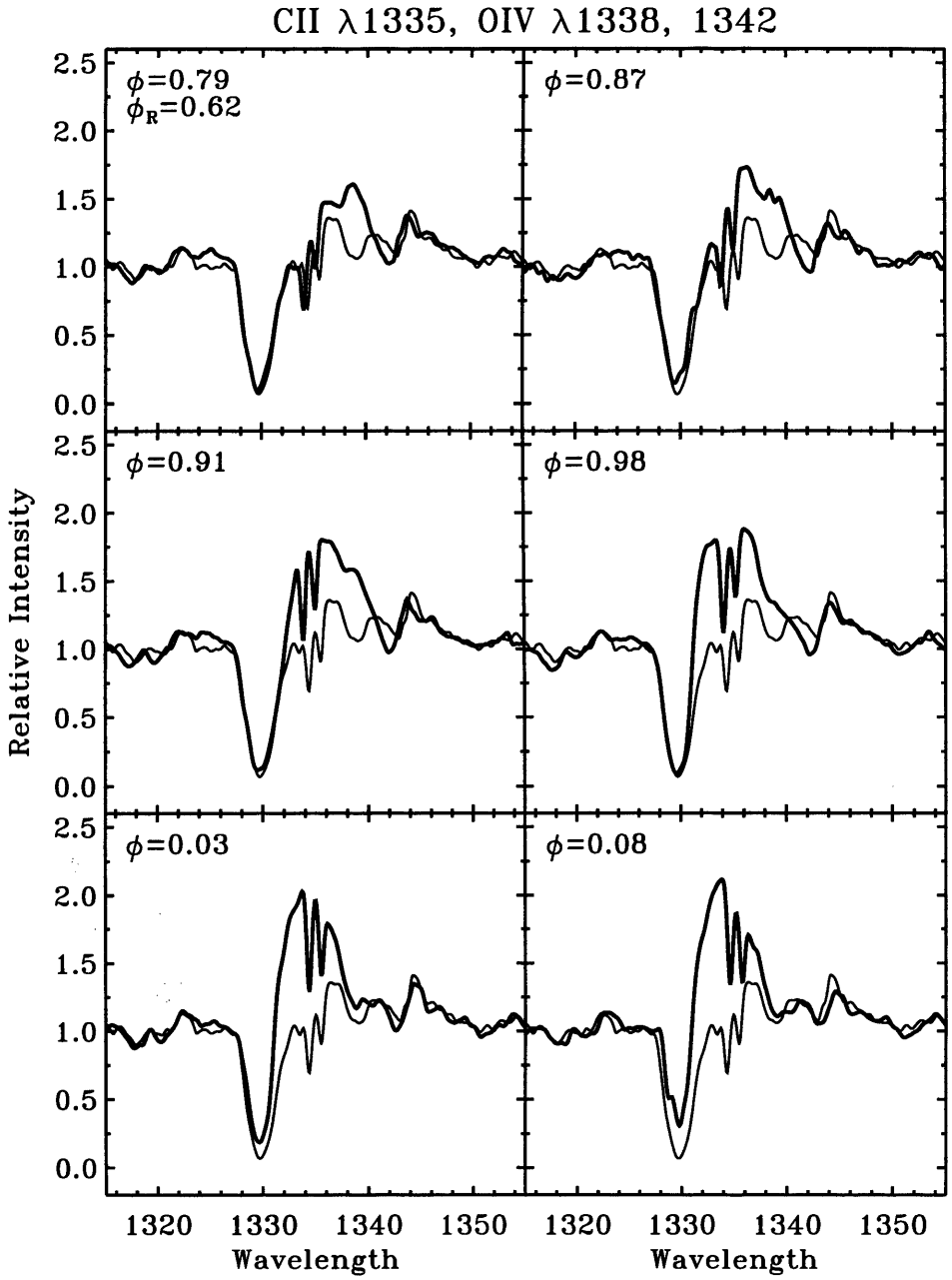

Figure 7.14: The C II λ1335 seen in absorption with its interstellar lines, and the weak P-Cygni profile, nominally of the O IV λ1338, 1342 doublet. Other details are as Figure 7.8.

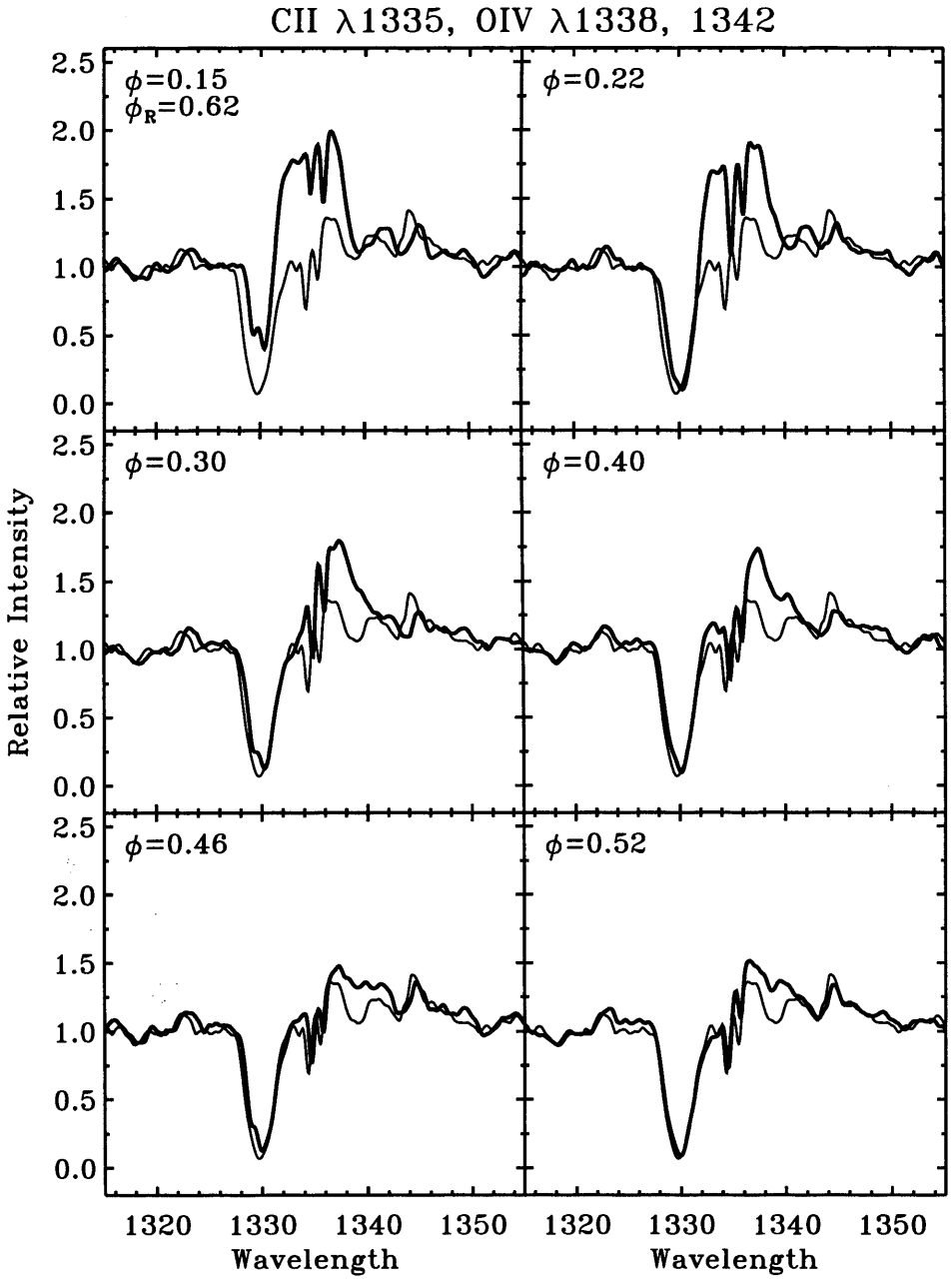

Figure 7.14: continued. The C II λ1335 and O IV λ1338, 1342 lines showing the six later phases. Other details are as Figure 7.8.

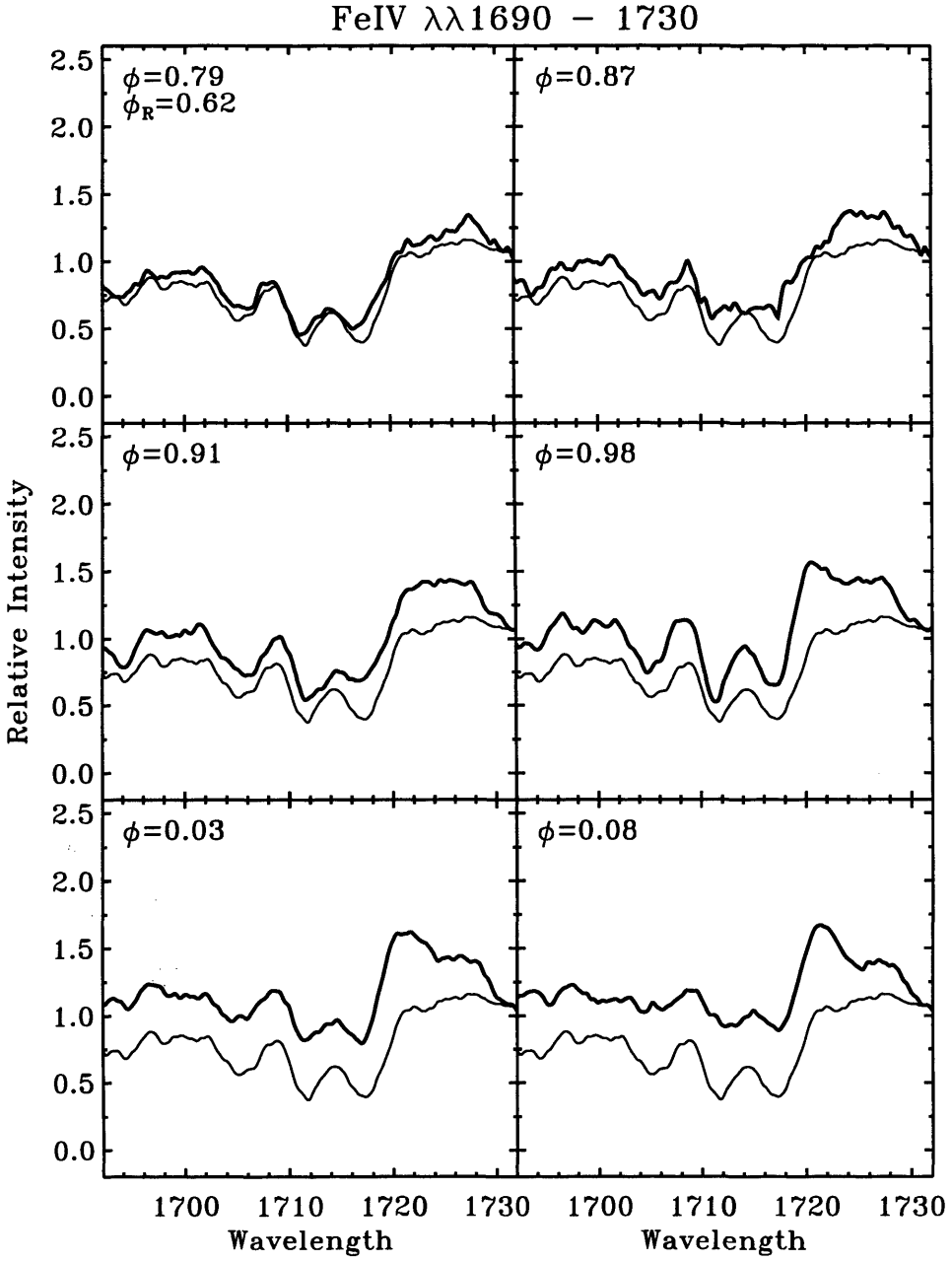

Figure 7.15: The λ1690 – 1730 region of the Fe IV pseudo continuum. Other details are as Figure 7.8.

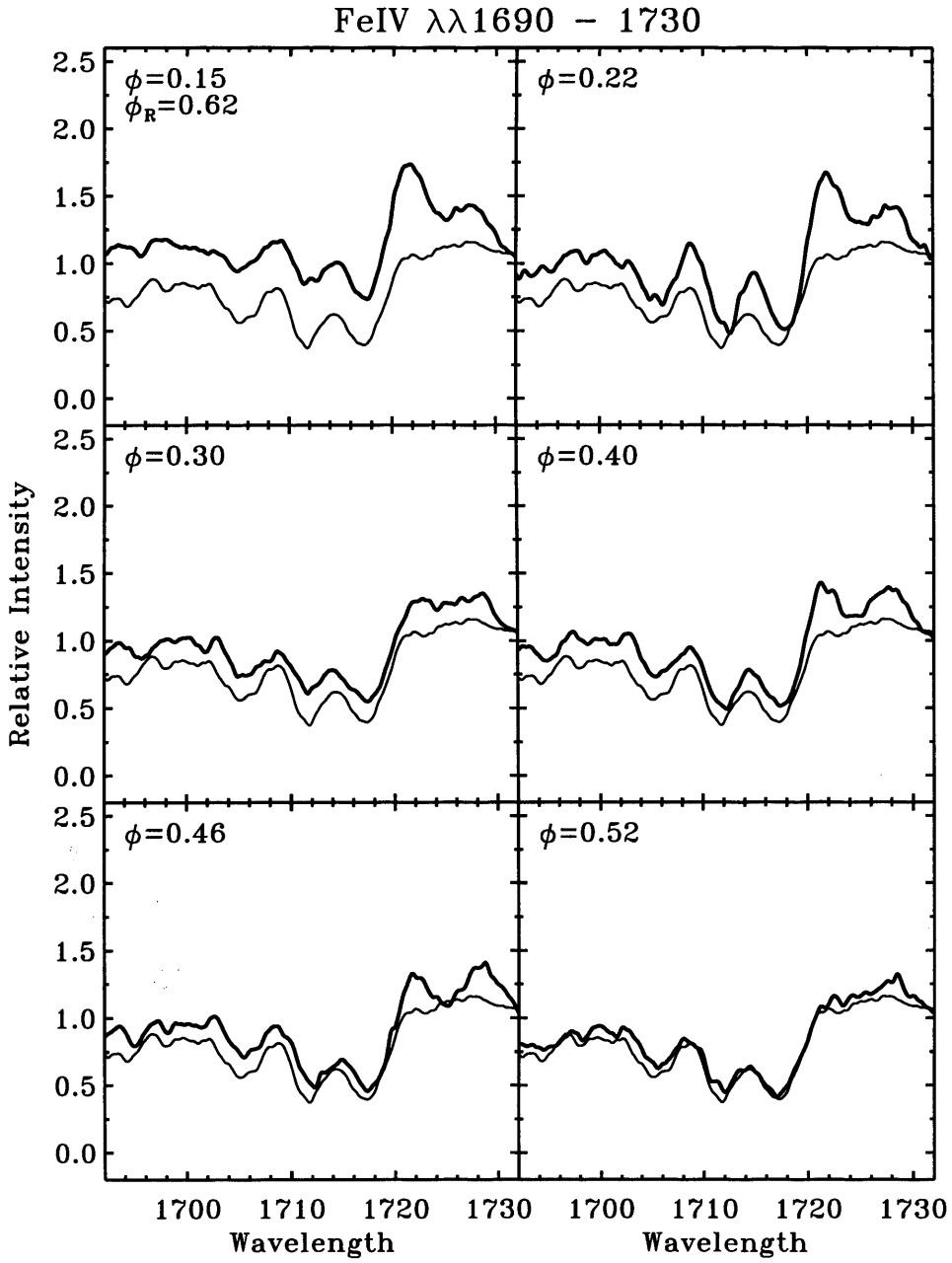

Figure 7.15: continued. The λ1690 – 1730 region of the Fe IV pseudo continuum showing the six later phases. Other details are as Figure 7.8.

7.7.9 Fe IV pseudo continuum

The Fe IV pseudo continuum covers the region from about 1400 – 1900 Å. The most significant variation takes place in the region from 1500 – 1700 Å and is easily visible in Figure 7.2. Outside of this the variation is small, 5–10%, and has been lost in the normalisation process, but can be seen in the difference spectra (e.g., St-Louis et al. 1993).

The region around λ1720Å (Figure 7.15) contains several groups of lines due to Si IV, S III, Al III and Fe IV. There is a broad emission complex trailing off to the red usually attributed to Si IV λ1722, 1725 but which probably has other contributors. This region also marks the red end of the Fe IV pseudo continuum. During the orbital cycle weak emission develops in a similar way to that seen previously, and it is probably consistent with the major component being Si IV λ1722, 1725. However, the emission reaches maximum somewhat after inferior conjunction and shows further activity at late phases, after quadrature. The emission activity is superimposed on the variation of the pseudo continuum, which initially increases slowly and then more rapidly towards inferior conjunction. The maximum change in intensity of the emission is ~ 0.7 of the pseudo continuum, of which ~ 0.3 is accounted for by the Fe IV pseudo continuum variation.

The main absorption lines show a complex pattern of variations, strengthening before and after inferior conjunction, during which time they weaken. The pattern follows the behaviour of C III] λ1909 and C II λ1335 but the variation is less extreme. After inferior conjunction, at $\phi \sim 0.22$, the lines show a small shift to the red of $\sim$ 1Å, which is also seen in C II λ1335 and C III] λ1909.

The N IV λ1718 line is not expected to be visible in the WR wind but it is expected to be a strong feature of the O-star photospheric spectrum. At $\phi = 0.87$ and 0.27 the O star will have its maximum negative and positive velocities but the profile at λ1718Å does not show any clear variation consistent with orbital motion.

7.8 Profile modelling

In order to model the absorption it is necessary to have a description of the ionization balance of the wind. The model can take an ad hoc radial distribution of the absorbing ion or something a little more realistic, based an assumed temperature structure. In the modelling the second approach is used but it requires lines from an ion in a number of ionization stages. Unfortunately the C III λ2297 and C IV λ1548, 1550 lines are saturated out to the terminal velocity and provide no useful constraints. The two lines that have been used are the C II λ1335 and C III] λ1909 lines, and while C III] λ1909 is not an ideal choice, blending and the weakness of other lines leaves little alternative.

The model was originally conceived to study changes in absorption, but for these lines there is practically no variation. Therefore it is necessary to model the absorption profile itself while ensuring that the difference in absorption between the phases in question is also correct. The ionization balance is determined by adjusting the abundance and temperature structure of the wind, and simultaneously matching the observed line profiles and their differences. In practice this leads to quite strong convergence on a solution, even when the variation is small. The ionization balance derived in this way is then used to model other lines.

The C II λ1335 line is expected to be formed at the extreme limit of the wind and is probably seen only in absorption (Hillier 1989 and Figure 7.14). In γ^2 Vel this line is just saturated and appears practically identical to the line in single WC stars. Being nearly saturated this line is not very sensitive to the carbon abundance, however, even in the outer parts of the wind C II is a minority species which makes it sensitive to the ionization balance of the wind. It is assumed that there is no emission and that the line is equally absorbed against both the WR and O-star continua. The strength of this line effectively determines the balance of C^+/C^{2+}.

The C III] λ1909 P-Cygni absorption in single WC stars is typically $\sim$ 0.5 of the pseudo continuum and in γ^2 Vel it is slightly weaker at $\sim$ 0.4. The strength of this line effectively determines the C^{2+}/C^{3+} balance because the lack of any significant variation in the absorption limits the inner extent of C^{2+}. A more detailed discussion

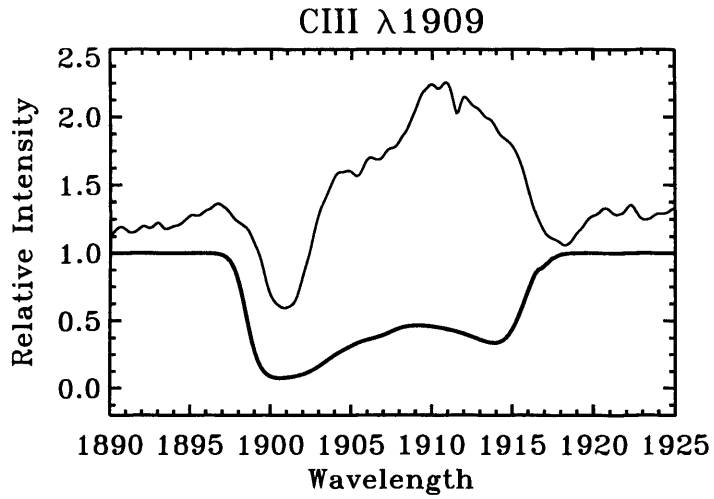

Figure 7.16: The C III λ1909 line at $\phi = 0.62$ (*thin line*) with a representative absorption profile which has been calculated to match to the terminal velocity (*thick line*). If this ionization balance is correct then during the orbit the absorption at low velocities will be removed leading to variation across the whole profile.

of this point is given below in § 7.8.1. When fitting these two lines it proved impossible to match the velocity of the core of the absorption without causing too much variation at low velocities in the C III] λ1909 line. The adopted ionization balance is based on the line strengths while matching the velocity as much as possible. The carbon abundance is principally based on the C III] λ1909 line so it is at the mercy of any non-LTE or other peculiarities of this transition. However, gross uncertainties should be prevented by use of the C II λ1335 line. The optimum value of the carbon abundance is C/He $\sim$ 0.1, within a factor of about 2, from the fitting. The size of the system means that the lines of sight sample material at close to the terminal velocity. A value of $\beta = 1$ was adopted for the velocity law although the results are largely independent of this value.

7.8.1 C III] λ1909

The lack of any significant variation in the P-Cygni absorption between superior conjunction and close to inferior conjunction ($\phi \sim 0.98$) demonstrates that there is no difference in column density between these two phases, which implies that the absorp-

tion takes place beyond the orbit of the two stars. The variation in the emission line superficially resembles selective absorption, but it is clearly different to the behaviour of the other strong emission lines. The model is unable to produce the variation at low velocities, i.e. within the emission line, without affecting the absorption profile. The profile at $\phi = 0.91$ (Figure 7.12) shows the problem most clearly. Also the model predicts variation across the whole line width, starting from the red edge, which is not what is seen (see Figure 7.16).

Around inferior conjunction the line of sight to the O star passes into the cavity caused by the O-star wind and the column density drops. In theory the wind absorption of the O-star should be removed and the profile revert to that of the diluted, single WR star. The real situation is much more complex. Firstly, the change in strength is about a factor of 2 which suggests that the two stars have approximately equal luminosities. The luminosity ratio (§ 7.1) would indicate a larger change. Secondly, there are complex profile variations in which the core of the absorption moves slightly to the red. If the general interpretation is correct then at some point the bulk of the line of sight must pass from the WR wind, through the shock zone and into the cavity. The only obvious transition is into the cavity, presumably from the shock zone. The transition from the WR wind to the shock zone probably occurs after quadrature but it must be very smooth because there are no substantial changes in velocity or line strength. After inferior conjunction the absorption returns to its original strength, at $\phi \sim 0.22$, but the profile is disturbed and continues to change until after quadrature. It seems likely that these changes are associated with the transition, of the line of sight, from the trailing edge of the shock zone to the WR wind. The model suggests only simple changes in the profile and is quite unable to match what is observed. The fit to the profile at $\phi = 0.62$ and 0.98 is practically identical and it only begins to break down at inferior conjunction, when the line is expected to weaken by $\sim 80\%$, due to the large luminosity ratio. However, one prediction of the model is that the absorption in the shock zone is shifted slightly to less negative velocities, and this is part of what is seen (see Figure 7.17) which shows the profiles at $\phi = 0.62$ and 0.15.

The discussion has centred on the variation caused by the selective absorption by the WR wind of the O-star continuum. However, depending on the circumstances of

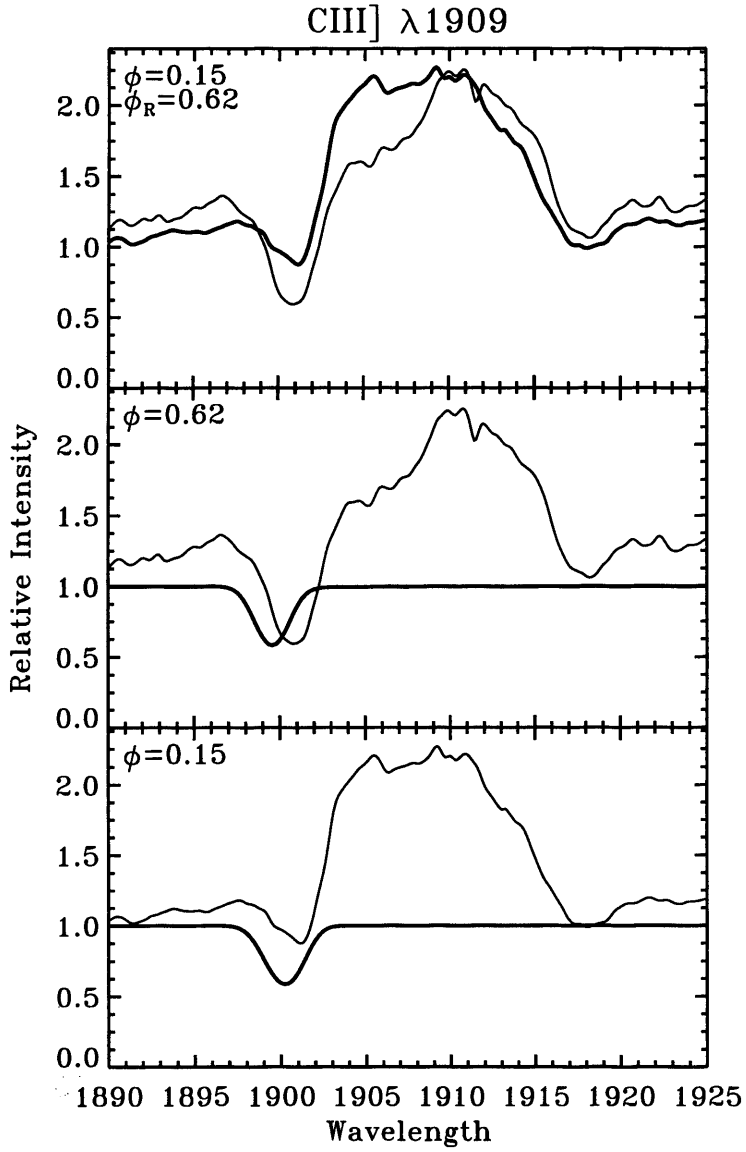

Figure 7.17: The C III] λ1909 line calculated profile. The top panel shows the observed profiles at $\phi = 0.62$ (*thin line*) and $\phi = 0.15$ (*thick line*). The lower two panels show the observed (*thin line*) and calculated (*thick line*) profiles at $\phi = 0.62$ (*middle*) and $\phi = 0.15$ (*bottom*). In none of the calculated profiles is it possible to match the velocity of the core of the absorption by simply adjusting the ionization balance of the wind, while maintaining no variation at low velocities. At $\phi = 0.15$ the model shows a slight shift in velocity relative to other phases, which is when the system is viewed along the edge of the shock zone. See the text for further details.

the orbit it quite possible that, around inferior conjunction, the WR 'continuum' is also seen through the material of the shock zone, as opposed to the undisturbed WR wind. The passage of the WR star across the boundary between the WR wind and shock zone will clearly complicate the profile.

Returning finally to the behaviour of the emission line it can been seen in Figure 7.12 that around inferior conjunction the red edge of the profile weakens. At this phase the selective absorption should have no effect; any changes at these velocities should occur near superior conjunction. On the figures tick marks show the maximum and minimum projected terminal velocities of the material streaming along the shock zone. In the model discussed recently by Lührs (1997), excess emission from the material in the shock zone, heated by the wind collision, should peak at these velocities, although there should also be significant emission at lower velocities. It is clear from the profiles that there are no significant emission peaks at the velocities indicated, however, there is a strong correlation with phase. When both peaks are to the red the emission profile tends to the red (around superior conjunction) and when both peaks are to the blue the emission profile tends to the blue (around inferior conjunction). Around quadratures, when the components are widely separated, the profile takes on a rectangular appearance. The bulk, if not all, of the variation in the emission line is qualitatively consistent with excess emission from the shock zone and not consistent with selective absorption.

7.8.2 C II λ1335

The model is unable to provide a good fit to the observed C II λ1335 profile but the discrepancy in velocity is not as large as for C III] λ1909. The calculated profiles at $\phi = 0.62$ and 0.98 are indistinguishable, which matches the lack of variation in the observed profiles (see Figure 7.14). The model does, to some extent, follow the clear velocity shift between $\phi = 0.08$ and $\phi = 0.15$ when the system is viewed along the edge of the shock zone. Figure 7.18 shows the fit to the C II λ1335 line at $\phi = 0.62$ and 0.15. However, the model does not predict the sharp high-velocity feature and the doubling of the line after inferior conjunction. It is possible that this is a weak

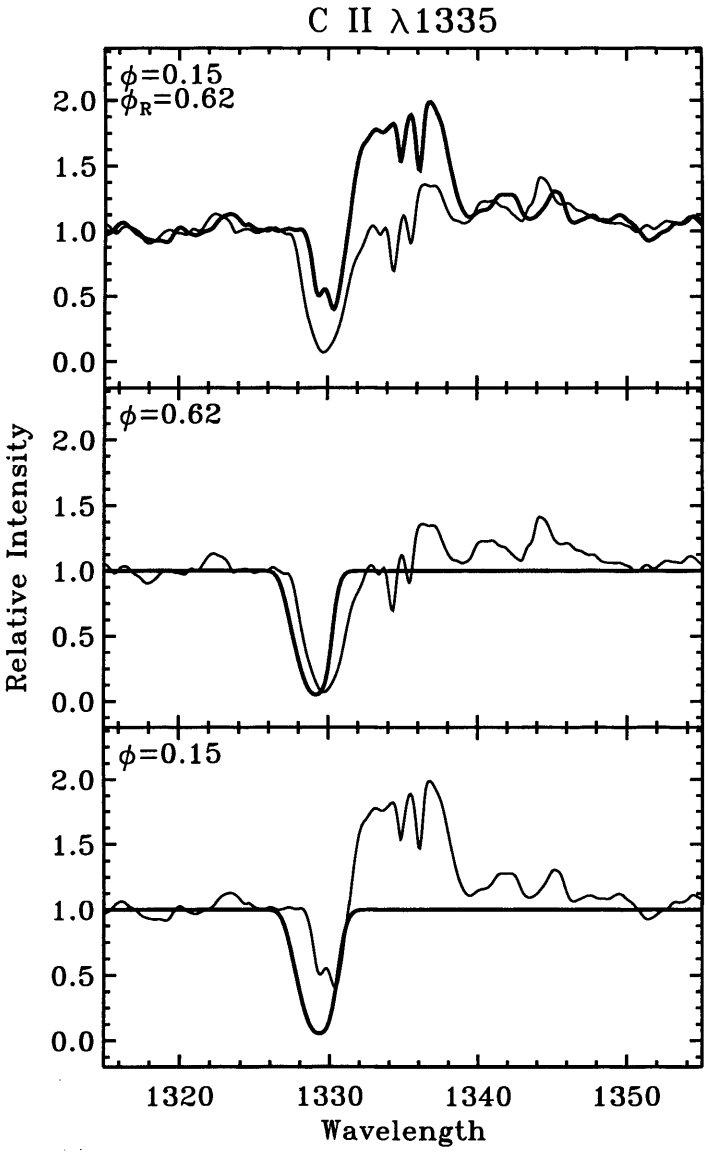

Figure 7.18: The C II λ1335 line calculated profile. The top panel shows the observed profiles at $\phi = 0.62$ (*thin line*) and $\phi = 0.15$ (*thick line*). The lower two panels show the observed (*thin line*) and calculated (*thick line*) profiles at $\phi = 0.62$ (*middle*) and $\phi = 0.15$ (*bottom*).

feature related to the extremities of the shock zone which only becomes visible when a significant part of the wind absorption is removed. The decrease in line strength of the C II λ1335 line is about a factor of 2, similar to C III] λ1909, and is rather less that expected for the luminosity ratio. Also, if the absorption of the O star is removed then the WR wind absorption should still be visible on the blue edge of the profile,

although this will be weak.

7.8.3 The saturated P-Cygni lines

For the saturated P-Cygni lines such as C IV λ1548, 1550, C III $\lambda\lambda$1175, 1247, 2297 and Si IV λ1393, 1402, the model suggests that the wind absorption is saturated across the whole width of the profile. As the O star emerges from behind the WR star the whole contribution of the O-star is progressively added to the profile from the red edge of the emission, ultimately to some way into the P-Cygni absorption. While the general character of the variation follows this pattern, in all these lines the magnitude of the variation is considerably larger than can be accounted for by selective absorption alone. The observed variation is typically 1.5 times the pseudo continuum of which the O star contributes $\sim$ 0.8 depending on the luminosity ratio. Many of the lines affected do not have strong O-star emission so this cannot be a factor, indeed the variations of C III λ 1175 and 2297 are among the largest.

Modelling the saturated lines in order to reveal further information about the wind is difficult because of the uncertainly in the luminosity ratio and the changing and largely unknown effects of the O star lines. The Si IV λ1393, 1402 doublet is particularly difficult to model due to the separation of the components. Small changes in the abundance or the ionization balance can have a dramatic affect on the inter-line region. Nevertheless models with a solar Si/He abundance (using the compilation of Allen 1973) are generally consistent with the observations.

7.8.4 Fe IV pseudo continuum

In contrast to the saturated lines the Fe IV pseudo continuum shows only modest variation and can be simply modelled. Two regions are shown. The first is the $\lambda\lambda$ 1500 - 1740 Å region in which 500 Fe IV lines with $gf \geq 0.02$ from the Kurucz list held in machine readable form by CCP7 have been used. This restricted set contains $\sim$ 65% of the lines available. The calculated profiles at $\phi = 0.62$ and 0.15 are shown in Figure 7.19 using the assumed ionization balance derived from fitting the C II λ 1335 and C III] λ 1909 lines and adopting a solar Fe/He abundance. Ignoring the area

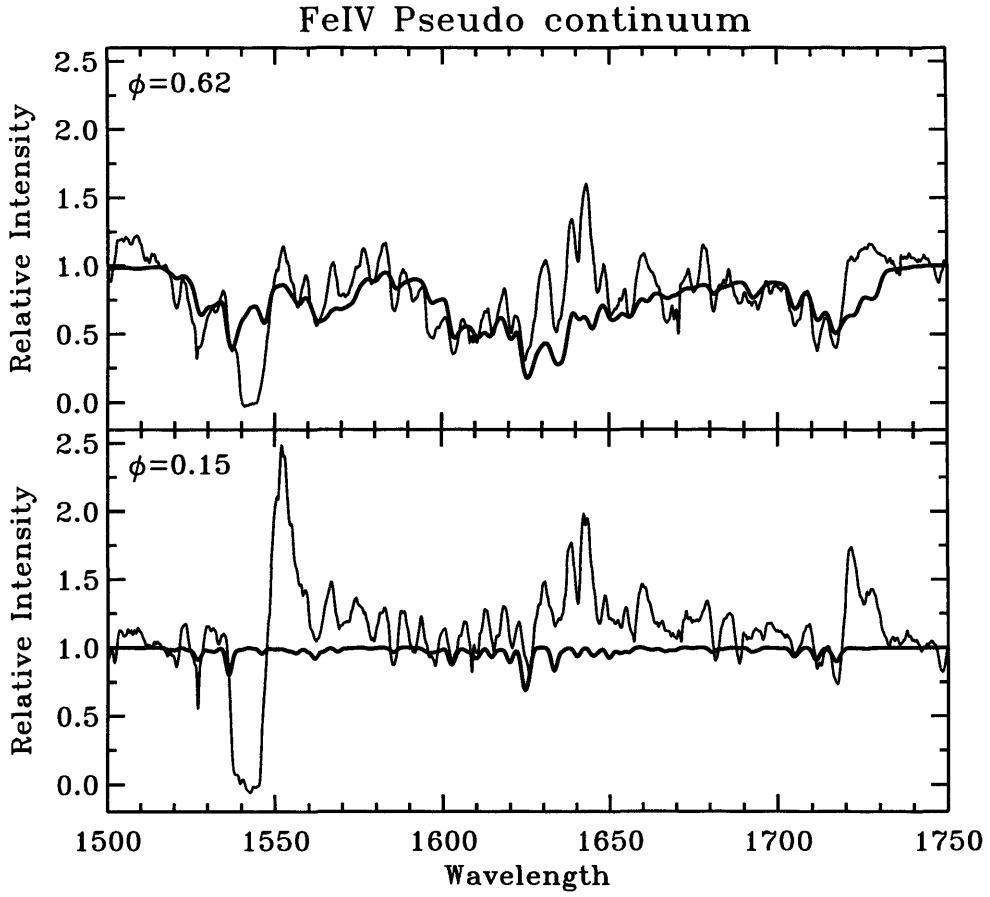

Figure 7.19: The Fe IV pseudo continuum at two phases, $\phi = 0.62$ (*top*) and $\phi = 0.15$ (*bottom*) showing the observed profiles (*thin line*) and calculated profiles (*thick line*) using the assumed ionization balance and a solar Fe/He abundance. See the text for further details.

of the C IV λ1548, 1550 and He II 1640 lines it can be seen that many of the individual features as well as the more general change in shape of the pseudo continuum is very well matched by the synthesised profile. Four of the strongest lines are clearly blended with C IV λ1548, 1550 and He II 1640 and another strong feature is superimposed on the Si II λ1526 line.

The second region $\lambda\lambda$1695 – 1735 is shown in more detail in Figure 7.20. The emission lines at $\sim$ 1720 Å are often attributed to the Si IV 1722, 1727 (e.g., Smith & Willis 1982, Auer et al. 1988). Modelling the lines reveals that the absorption components are not due to Si IV. They are too weak, being only $\sim$ 10% of the continuum, and fall at the wrong wavelengths, at $\sim$ 1710 and 1715 Å. The three principal absorption

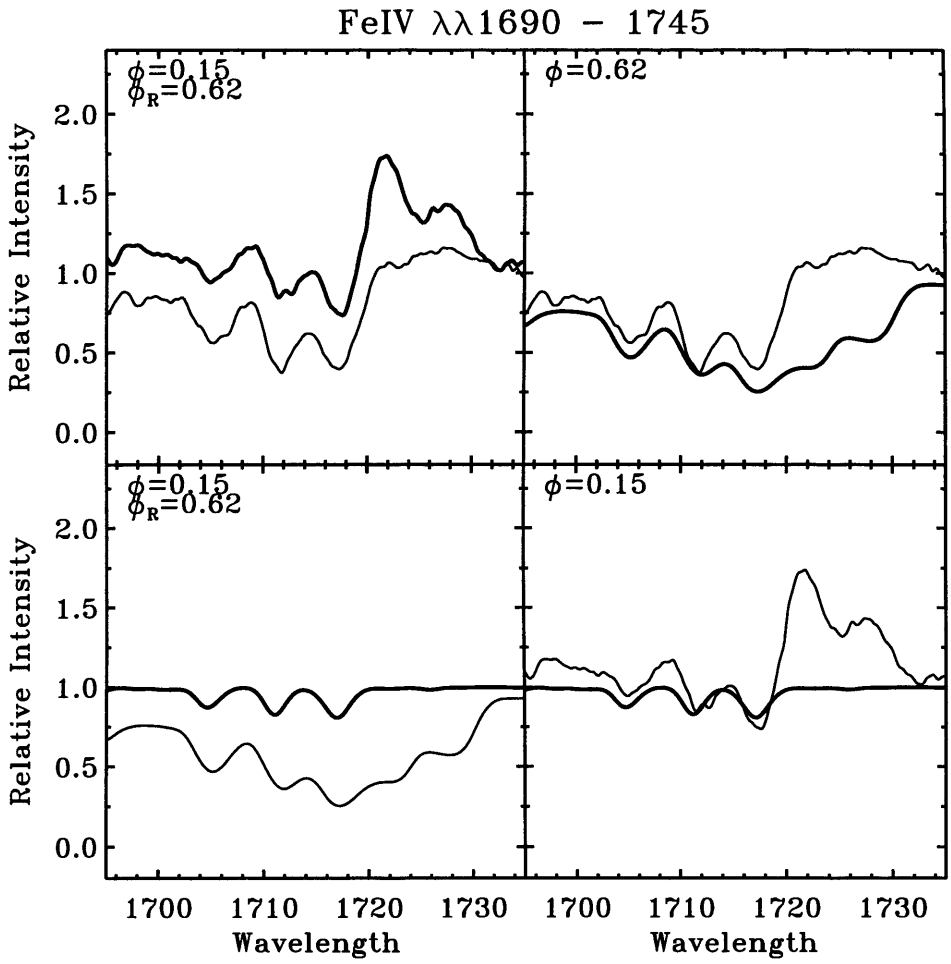

Figure 7.20: The Fe IV pseudo continuum calculated profile at λ1690 – 1730. The left-hand panels show the observed (*top*) and calculated (*bottom*) profiles at $\phi = 0.62$ (*thin line*) and $\phi = 0.15$ (*thick line*). The right-hand panels show the observed (*thin line*) and calculated (*thick line*) profiles at $\phi = 0.62$ (*top*) and $\phi = 0.15$ (*bottom*). See the text for further details.

components and indeed several other features close to the blue, are clearly identified with Fe IV lines. The calculated profiles were generated using some 150 lines in the 1690 – 1745 Å region. An Fe/He ratio of twice solar is used for these plots which fit the observed features well in both wavelength and relative strength. The change in the continuum level between the two phases is well matched by the model although part of the variation is obscured by the change in the emission line. The relative strengths of the three main feature are not perfect but it is possible that there are errors in the f-values of the weak lines or other contributing features. The observed continuum is also 5–10% too high as a result of the normalisation process.

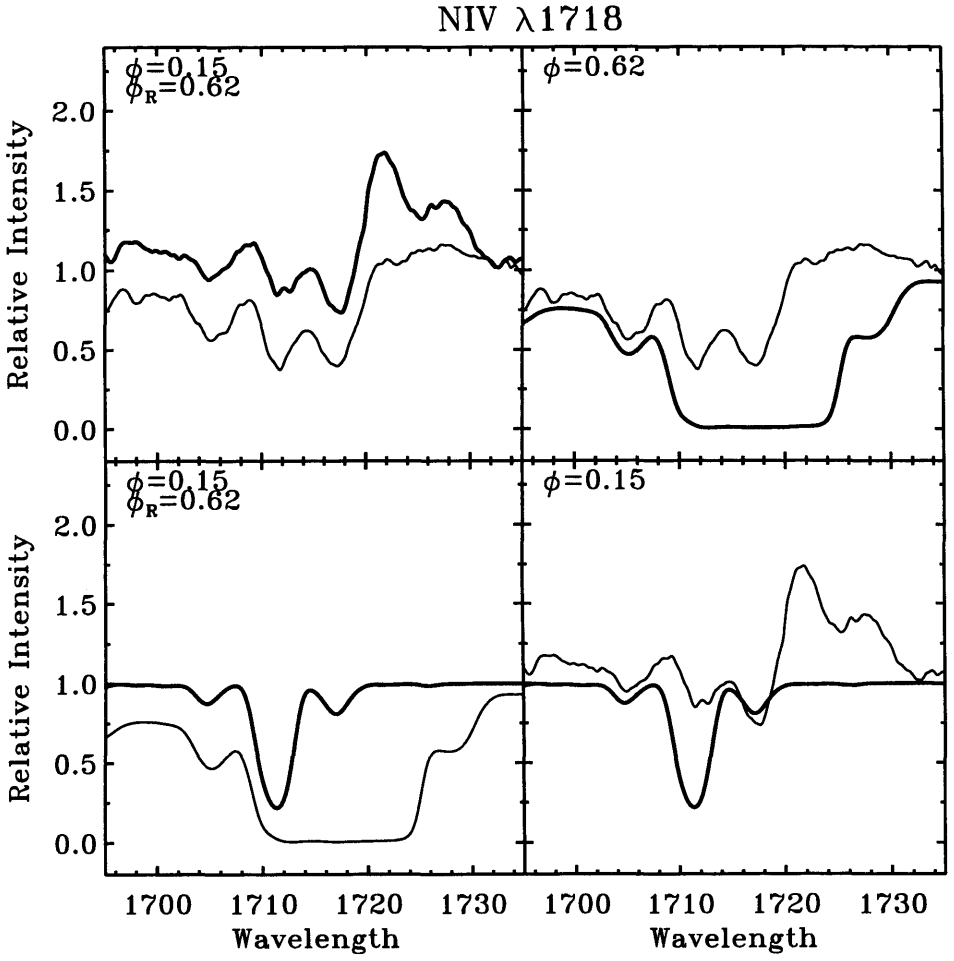

Figure 7.21: The λ1690 – 1730 region showing the calculated absorption profile including the N IV λ1718 line. The left-hand panels show the observed (*top*) and calculated (*bottom*) profiles at $\phi = 0.62$ (*thin line*) and $\phi = 0.15$ (*thick line*). The right-hand panels show the observed (*thin line*) and calculated (*thick line*) profiles at $\phi = 0.62$ (*top*) and $\phi = 0.15$ (*bottom*). The same region without the N IV line is shown in Figure 7.20. See the text for further details.

7.8.5 Limit on N IV λ1718

By modelling this region of the spectrum, including the N IV λ1718 line with the Fe IV lines as in § 7.8.4, it is possible to place some limit on the nitrogen abundance. Figure 7.21 shows the results with N/He = 10^{-4} by number. At $\phi = 0.62$ the line in the wind is saturated, so by implication it would also be saturated in the spectrum of the WR component alone. The red edge of the profile is very uncertain because

the N IV line, if present, would contribute some emission, and there is also emission from other lines. However, the important point is that the difference between the two calculated spectra suggests a large variation in the region $\lambda\lambda 1710 - 1720$ Å which is not observed. The profile at $\phi = 0.15$ suggests that the line present at $\lambda 1711$ Å should be 3–4 times stronger than observed with this level of nitrogen. Reducing the N/He ratio by a factor of 10 removes almost all of this variation so it is reasonable to take N/He $< 10^{-4}$ as a conservative limit.

7.9 Discussion

The large change in the saturated lines of more than the combined continuum, is a particular problem for selective absorption and was recognised by St-Louis et al. (1993). To explain this anomaly they considered back scattering of the O-star continuum off the WR wind but found this incapable of producing such a large effect. St-Louis et al. also pointed to evidence to suggest that the flux visible at inferior conjunction is not unabsorbed, as they had assumed. Indeed from the nature of the variation described above and the models the wind clearly absorbs the O star, towards the terminal velocity, when it is in front of the system. However, this effect still cannot explain the large variation near the peak of the emission.

The other strong emission line, C III] $\lambda 1909$ also shows some variation but in this case the line intensity changes little. The profile does sway from positive to negative velocities with orbital phase but this variation is not consistent with selective absorption. Such changes are broadly consistent with the model of excess emission from the shock zone (see Lührs 1997). The O IV $\lambda 1342$ line behaves in a similar way and the reason it is visible in these two lines is because the masking effects of selective absorption are small or absent. It therefore seems likely that excess emission is also present in the saturated lines but is more difficult to see because of the effects of selective absorption. In addition the two effects are probably entwined. As the excess emission rotates with the shock zone it will itself undergo selective absorption by the WR wind, and self absorption at specific phases, in exactly the same way as the O-star wind emission. The effect will be greatest for the saturated wind lines which is

precisely what is observed. The implication of this discussion is that the strength of the emission from the shock zone is large, in this case probably equal to the intensity of the O star in the lines. One final point concerns the anomalous wavelength of the O IV λ1342 emission. If the luminosity ratio is large then this emission would be quite weak, which raises the possibility that this feature is instead, C II λ1335 emission from the shock zone.

The emission line ratios discussed in § 7.4 can now be seen in a new light. The lines in γ^2 Vel appear so much stronger than in single stars and are so inconsistent because they are inflated by emission from the shock zone. The lines showing the smallest ratios are again those with saturated wind absorptions and only the weak lines provide any unbiased (but unreliable) estimate of the luminosity ratio.

During the first half of the orbit features are seen to develop on the blue wings of the C IV λ1548 and Si IV λ1393 absorptions which are consistent with absorption by the O-star wind. The C IV line is expected to be the stronger, probably saturated and is clearly identifiable at superior conjunction. These features deepen and develop progressively until they saturate (see Figures 7.9 and 7.10) which is when the cavity in the wind is directed towards the observer, and the O star is seen directly. However, there are some problems with this scenario. Firstly the Si IV λ1393 line is not saturated in O8 giants; this usually only occurs in luminosity class II((f)) or class I. Secondly the N V λ1239, 1243 lines which are found only in the O-star spectrum do not show the same progressive change. Instead the blue wing of the N V absorption first becomes extended suggesting an increase in the terminal velocity, and only strengthens when the cavity swings into the line of sight and the O star is seen directly. The apparent difference in behaviour can be reconciled by considering the variations in terms of an increasing column at high velocities. When the cavity is pointed away from the observer the column in the O-star wind is truncated by the shock zone. As the cavity swings round more towards the observer the column increases and the O-star line strengthens. The strength of these lines suggests that the O star is not viewed through the undisturbed O-star wind but is actually seen through the O-star side of the shock zone, where the density of the O-star wind will be increased by some factor due to the compression by the WR wind.

Prinja et al. (1990) used the depth of the C IV λ1548 feature due to the O star to estimate the UV luminosity ratio and estimated Δm $\sim$ 0.7 in favour of the O star. Unfortunately the phase they chose (taken from Kondo et al. 1982) was not inferior conjunction but rather nearer quadrature (see 7.5). At inferior conjunction the N V line appears saturated but it is not at zero intensity. Similarly the C IV and Si IV lines at $v < v_\infty$(WR) do not reach zero intensity. If the intensity of these features indicates the saturated O-star continuum then this leads to a luminosity ratio $L_{\rm O}/L_{\rm WR}\sim$ 5 which is consistent with the previously derived values.

One point which does not seem to have been raised previously is the weakness of the emission lines at superior conjunction. At this phase the O star is absorbed but the emission from the WR wind should still be visible. However, if the luminosity ratio is large then the WR-wind lines may be so diluted that they only reach 10–20% above the continuum. The intensity of the strongest line at superior conjunction, C III λ2297, also implies $L_{\rm O}/L_{\rm WR}\sim$ 4.

With such a high luminosity ratio is difficult to interpret the modest variation of the C III] λ1909 and C II λ1335 lines at inferior conjunction when there is expected to be no WR-wind absorption. It suggests that there is residual selective absorption by the wind, which implies that some part of the wind still lies across the line of sight. One way of producing this is by curvature of the cavity. Such an effect would also explain the small but well observed variations well after inferior conjunction and the asymmetry of the X-ray flux variations. The observations clearly show maximum strength of the O-star lines at $\phi \sim 0.1$, which is coincident with the maximum X-ray flux.

The second difficulty with the C III] λ1909 and C II λ1335 lines is the failure of the model to correctly match their terminal velocities. The observed velocity of these lines appears too small (see § 7.5) which may be due to excess absorption at low velocities or a lack of absorption near v_∞. As was shown when modelling these lines (§ 7.8.1) it is difficult to create more absorption at low velocities without causing variation across the whole of the profile. However, if the shock zone has become wrapped around the whole system at large radii it is possible that where the C III] λ1909 and C II λ1335 lines are formed the ions are prevented from reaching v_∞. The

saturated absorptions on the other hand have sufficient column density to absorb at $\sim v_\infty$ at smaller radii.

In their discussion of the Fe IV pseudo continuum St-Louis et al. found the absorption narrower than expected and also had to apply a velocity shift to their generated spectrum. They had assumed that the absorption is centred on the rest wavelength and taken the width from the saturated wind absorption lines. As was shown in § 5.7 and above, the velocity and width of the absorption are determined by where the line is formed. In the profile fitting (§ 7.8.4) both the the velocity and width of the Fe IV pseudo-continuum lines are fitted naturally by the model of the basis of the adopted ionization balance alone. St-Louis et al. also found that the C III] λ1909 line behaved in a similar way but in this case the reason is due to the swaying of the emission peak as a result of excess emission.

7.10 Conclusions

A detailed discussion of the phase-dependent line profile variations of γ^2 Vel has been presented together with a review of the orbit and luminosity ratio of the components. The first conclusion is that selective absorption is able to explain the variation of the major emission and absorption lines, and in the case of the Fe IV pseudo continuum, the detailed variation of many minor lines as well. The model is successful in quantitatively synthesising the profiles of the lines based on a simply derived ionization structure which provides for radial stratification of the wind. The ionization structure is similar to that determined from detailed NLTE calculations (Hillier 1989, Hamann et al. 1992). The model also allows abundance determinations to be made which suggest C/He $\sim$ 0.1 (by number), similar to other recent determinations (Eenens & Williams 1992) with Si and Fe about solar. Modelling has also enabled an upper limit of N/He $< 1.0^{-4}$ to be determined from the N IV λ1718 line. The size of the γ^2 Vel system has prevented any discussion of the wind velocity law.

The analysis has also revealed that emission from the shock zone is a major contributor to the emission lines and has a large impact on the observed variation. The behaviour of the C III] λ1909 line is not consistent with selective absorption but is

broadly compatible with the excess emission produced by the shock zone as given by Lührs (1997). Similar emission is probably also responsible for the variation and strengths of He II λ 1640, C IV λ1548, 1550, Si IV λ1393, 1402 and λ1722, 1725, O IV λ1342 and C III λ1175 and 2297. The excess emission also explains the anomalous line ratios at inferior conjunction (§ 7.4). The important point of difference between the Lührs model and the idea presented here is that the excess emission from the shock zone also undergoes selective absorption.

The luminosity ratio of the components is found to be large, $L_{\rm O}/L_{\rm WR}\sim$ 5, from the N V, C IV and Si IV absorptions and the C III λ2297 emission.

There is some evidence suggesting asymmetry in phase of the profile variations, which is consistent with the X-ray variations, and anomalous wind absorption which may point to curvature of the shock zone.

Chapter 8

HD 152270

HD 152270 (WR79) is one the brightest Wolf-Rayet binaries, with $V = 6.60$. In the WR catalogue (van der Hucht et al. 1981) the star is classified as WC7+O5-8 with a period of 8.89 days. It has been observed extensively in the optical, spectroscopically and polarimetrically, less so in the IR and UV. Phase-dependent variations have been studied on *IUE* short-wavelength, low-resolution spectra by Auer et al. (1988) who found weak variations in the equivalent width of only the C III] λ1909 line. Recently Lührs (1997) has investigated the behaviour of the C III λ5696 line which shows relatively sharp emission features moving across the top of the line. These features are interpreted as additional emission due to material in the shock zone, as discussed in § 4.2.

8.1 HD 152270 as a member NGC 6231

HD 152270 lies within the open cluster NGC 6231 which forms the nucleus of the Sco OB1 association. The cluster also contains some dozen O stars and the WN7 star WR78. Comparison with evolutionary models gives an age for the cluster of 5.6 Myr (Meynet et al. 1993, cf., Santos & Bica 1993) which has a slight abundance deficit of 0.1 – 0.3 dex relative to solar (Kilian et al. 1994). On the basis of proper motion studies of the Sco OB1 association (Braes 1967) and radial velocities of cluster stars, HD 152270 is a member of the cluster. Struve (1944a) found a mean velocity of -29

km s^{-1} from 13 stars which agrees well with the systemic velocity of HD 152270, −30 km s^{-1}, derived later (§ 8.3.1).

NGC 6231 has been the subject of many photometric, abundance and evolutionary studies. The distance modulus and reddening have been estimated as $(V - M_V)_0$ = 11.25, E_{B-V} = 0.42 (Seggewiss 1968), $(V - M_V)_0$ = 11.00±0.25 (van Genderen et al. 1984) and from Stromgren photometry $(V - M_V)_0$ = 11.21±0.06 (Balona & Shobbrook 1984), $(V - M_V)_0$ = 11.08±0.05, A_V = 1.43 (Balona et al. 1995). Adopting $(V - M_V)_0$ = 11.1, A_V = 1.4, and a visual magnitude V = 6.60 for HD 152270, gives an absolute magnitude for the system, M_V = −5.9, with an error of perhaps ± 0.1 mag.

HD 152270 has been classified as WC7+O5-8 (Smith 1968b) and WC7+O5 (Hiltner & Schild 1966). At somewhat higher resolution Seggewiss (1974) gives WC6-7 for the Wolf-Rayet component and finds that the O star is clearly earlier than λ Cep (O6f) and HD 206267 (O6). The absolute visual magnitude of WC7 stars, M_{WC7} = −4.8±0.3 (van der Hucht et al. 1988) which yields M_O = −5.4 for the O5 companion. Similar values are adopted for O5 stars by Hucht et al. (1988) giving a luminosity ratio, L_O/L_{WR} = 1.7 or ΔV = 0.6 mag. Smith & Maeder (1988) give ΔV < 1.0 and Seggewiss (1974) finds ΔV ≈ 1.1 mag, while van der Hucht et al. (1988) find both components have the same magnitude.

8.2 Observations

The *IUE* archive contains 37 high-resolution spectra of HD 152270, 21 and 16 taken in the short- and long-wavelength ranges respectively. Images were taken over the whole lifetime of *IUE* but they are concentrated in the years 1984, 1987, 1995 and 1996, mostly taken in collaboration with Dr D.J. Stickland. Only two early images were taken through the small aperture, all the other were taken through the large aperture. The logs of short- and long-wavelength images are given in Tables 8.1 and 8.2 respectively together with the orbital phases calculated using the ephemeris derived later in § 8.3.1. The spectra were extracted from the *IUE* G/PHOT images using the IUEDR routine as described earlier in § 6.1

Table 8.1: IUE short-wavelength images

Image	HJD	Phase	Image	HJD	Phase
SWP 2512	2443758.8016	0.4428	SWP55263	2449911.3532	0.3938
SWP15129	2444877.8696	0.2996	SWP55272	2449912.3608	0.5071
SWP16088	2444991.4011	0.0680	SWP55284	2449913.3573	0.6192
SWP31298	2446983.3910	0.0985	SWP55302	2449915.3523	0.8436
SWP31306	2446984.5528	0.2292	SWP56934	2450179.1020	0.5064
SWP31428	2447005.4203	0.5760	SWP56940	2450180.1382	0.6229
SWP31628	2447031.3099	0.4877	SWP56944	2450181.0793	0.7287
SWP31635	2447032.2626	0.5949	SWP56949	2450182.0955	0.8430
SWP45124	2448816.5976	0.2714	SWP56963	2450185.0962	0.1805
SWP45203	2448825.3527	0.2560	SWP56969	2450186.0533	0.2881
SWP55251	2449910.3824	0.2846			

The phases given are photometric

Table 8.2: IUE long-wavelength images

Image	HJD	Phase	Image	HJD	Phase
LWR 2296	2443758.8266	0.4456	LWP32113	2450179.1208	0.5085
LWP11154	2446983.4098	0.1006	LWP32115	2450180.0993	0.6185
LWP11157	2446984.5715	0.2313	LWP32117	2450180.9938	0.7191
LWP11291	2447005.3828	0.5718	LWP32118	2450181.0584	0.7264
LWP11469	2447031.3265	0.4896	LWP32119	2450181.1043	0.7316
LWP11474	2447032.2008	0.5879	LWP32121	2450182.0724	0.8404
LWP23488	2448816.5782	0.2692	LWP32126	2450185.0705	0.1776
LWP23560	2448825.3325	0.2537	LWP32128	2450186.0227	0.2847

The phases given are photometric

8.3 The orbit

The first orbital determination of this system was by Struve (1944b) who derived a period of 8.82 days and found amplitudes of $K_{\rm WR} = 168$ and $K_{\rm O} = 45$ km s^{-1} for the WR and O star respectively. The scatter around the velocity curves was large, particularly for the O star. The most recently published orbit was derived

by Seggewiss (1974) who refined the period to 8.893 days and found similar velocity amplitudes to Struve, $K_{\rm WR}$ = 141 and $K_{\rm O}$ = 51 km s^{-1} for the WR and O star respectively.

Recently Lührs (1997), has combined some new optical measurements of the C III λ 5695 line with those of Seggewiss and Struve to derive a new velocity curve for the WR component, and suggests two possible periods, 8.2373 or 8.8910 days. For the preferred, longer period, which is consistent with Seggewiss' period, Lührs finds $K_{\rm WR}$ = 133 km s^{-1}.

8.3.1 The IUE orbit

HD 152270 was compared against the library of O-type stars, and found to give the strongest correlation against stars of early-to-mid O spectral type, e.g., HD 164794,

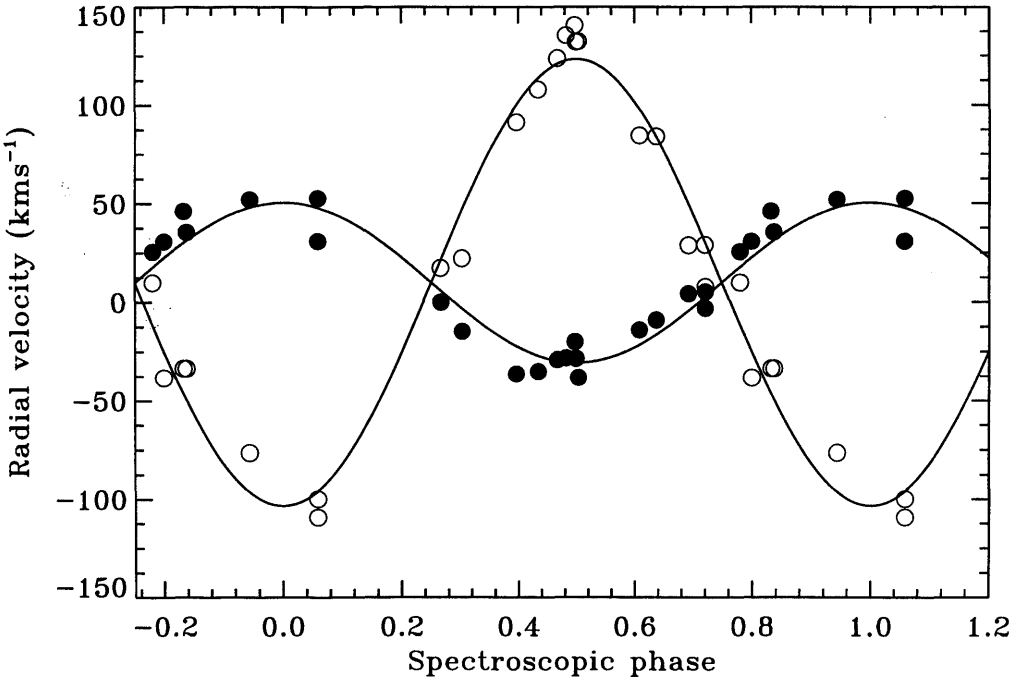

Figure 8.1: The *IUE* orbit of HD 152270 from a representative double-lined solution. The O star (*filled circles*) is treated as the primary. The phases are spectroscopic, relative to maximum positive velocity of the primary. See the text for details.

Table 8.3: The IUE orbital elements of HD 152270.

	Single O	Single WR	Double
P (days)	8.8916±0.0002	8.8913±0.0002	8.8913±0.0002
$K_{\rm O}$ (km s^{-1})	41±2		40±2
$K_{\rm WR}$ (km s^{-1})		113±5	113±3
e assumed	0.0		
ω assumed	0.0		
T_0 2440000+	9914.56±0.08	9910.44±0.08	9914.84±0.08
σ (km s^{-1})	5	14	12

In the double-line solution the velocities of the WR component were adjusted to align the γ velocity with that of the O star.

O4 V((f)); HD 93843, O5 III(f)var and HD 93222, O7 III((f)) (see § 6.2). HD 91824, O7 V((n)) was finally chosen as the primary template for its symmetrical and relatively sharp cross-correlation profile. After considerable experimentation with the spectral masks and other measurement parameters a number of single-line orbital solutions were derived for the O star. Using mostly HD 91824, but also some of the other standards, the solutions gave $K_{\rm O}$ = 40 - 50 km s^{-1} with σ = 5 - 10 km s^{-1}. From the best solutions the adopted ephemeris for the O star is

$$T_{\phi=0} = 2448431.846 + 8.8916E$$

which is used to derive the photometric phases used later. The spectroscopic orbital elements are given in Table 8.3.

The spectra of HD 152270 were also cross correlated against archival *IUE* spectra of single WC stars. WR57 and WR90, both WC7, gave useful correlations but the strongest was WR135, WC8. The reason for the difference probably has little to do with matching spectral types, but simply because WR135 has sharper lines. The cross correlation function was broad and asymmetrical but the peak gave a variation of $\sim$ 113 km s^{-1} with the same period as the O star. Two of the best single-line measurements were combined into a double-lined solution, which is shown in Figure

8.1. In view of the difference in $K_{\rm WR}$ between the optical and *IUE* orbital solutions the ephemeris for the O star was used the phase the spectra.

To place the velocities on a near absolute basis the measured velocities were corrected for the stellar and interstellar velocities of τ Sco, +2 and $-8\,{\rm km\,s^{-1}}$ respectively (Stickland & Lloyd 1995), and for the interstellar velocity of HD 152270. The interstellar velocities towards HD 152270 are complex. The rough mean of the Ca II K line is $-15\,{\rm km\,s^{-1}}$ (Crawford 1989). The saturated Na I D lines have a mean at $-5\,{\rm km\,s^{-1}}$ (Crawford 1992) while the weaker Na I λ 3302 line and the molecular lines of CH, CH^+ and CN have a velocity of $2.2\,{\rm km\,s^{-1}}$ (Crawford 1992, 1995). Adopting a value a $-15\,{\rm km\,s^{-1}}$ gives a value for the systemic velocity, $\gamma = -30\,{\rm km\,s^{-1}}$. There is also evidence of high-velocity shocked interstellar gas (Crawford 1992, Nichols & Fesen 1994).

8.3.2 Inclination

Using the method of phase-dependent polarization variations developed by Brown et al. (1978)(see § 7.3.1), Luna (1982) derived two possible values of the inclination, the preferred one, $i = 35 \pm 8°$, and a lesser alternative which used all the available data, $i = 42 \pm 10°$. As part of an extensive programme of polarimetry of WR binaries St-Louis et al. (1987) using the same method, derived a value of $i = 45 \pm 3°$. The two main assumptions of the Brown et al. model are that the scattering envelope, the WR wind, is spherical and that the companion's wind is negligible. Clearly the wind of the O star is smaller that that of the WR star but it is hardly negligible and the wind collision produces a highly non-spherical shock zone. Moffat & Piirola (1993) attempted to test the sphericity of the scattering envelope by measuring the polarization in the optical emission lines of HD 152270 and HD 97152. If the lines are scattered in a spherical wind then the net polarization will be zero, and this is what Moffat & Piirola found.

Recently Lamontagne et al. (1996) have developed a method of measuring the inclination based on the continuum 'atmospheric' eclipse of the O star by the WR wind. The variation is caused by the change in the electron scattering optical depth which can be

modelled if the relevant system parameters are known. For HD 152270 Lamontagne et al. derive an inclination, $i = 33.6 \pm 2.3°$. However, it should be pointed out that there is a systematic difference between the inclinations derived by the photometric and polarization methods with the photometric method giving consistently smaller inclinations. Harries & Hilditch (1997) discuss this question in some detail in the context of the short-period, WN+O binary CQ Cep. They suggest that the difference may be due to neglected line-flux variations in the atmospheric eclipse model, or alternatively that the errors in the polarimetry bias the inclinations to higher values (Aspin et al. 1981). The recent work on γ^2 Vel is of little help on this question. Schmutz et al. (1997) found that the errors on the polarization are such that the inclination is unconstrained, and γ^2 Vel, despite being a relatively high-inclination system, was not discussed by Lamontagne et al. (1996).

8.4 UV luminosity ratio

The luminosity ratio of the components of HD 152270 has been investigated using the dilution of the emission lines by the O-star continuum relative to those of single WC6-8 stars, in exactly the same way as for γ^2 Vel (see § 7.4).

The ratio of equivalent widths $R_{\rm W}$ and peak intensities $R_{\rm I}$ are calculated in the sense $R_{\rm W} = W_{\rm star}/W_{\rm HD152270}$ and $R_{\rm I} = I_{\rm star}/I_{\rm HD152270}$. The ratio of equivalent widths shown in Figure 8.2 cover the range 0.5 – 4 with considerable variation between different lines and for different stars. Lines from the long-wavelength region, $\lambda > 2000$ Å, give values systematically higher than those from the short-wavelength region. These lines are generally weak, ~ 1.5 times the continuum, so they possibly reflect an error in the level of the continuum. However, this would have to be large as a factor of ~ 2 would be required to bring them into line with the other values. The lines showing the largest scatter are C IV λ1550, O IV λ1342 and He II λ1640 but to what extent this is affected by natural variation between stars and difficulties of measurement is not clear. The other lines from the short-wavelength region and C III λ2297 show much better internal consistency, but generally poor agreement. However, the most significant feature of this diagram is the number of values that fall below unity. These

measurements imply that in spite of any dilution by the O-star continuum some of the emission lines in the binary are a factor of ~ 2 stronger than in single WR stars. In the case on C IV λ1550 there is natural variation between stars of a factor of ~ 5, so if HD 152270 were at the top end of the range the measurement could be explained. On the other hand the C III λ1247, Si IV λ1402 and λ1722 lines show good internal agreement and also suggest that the lines in HD 152270 are uncommonly strong. The general distribution is not dissimilar to that of γ^2 Vel (Figure 7.6).

In contrast to the equivalent width measurements the ratio of peak intensities, shown in Figure 8.3, occupy a relatively restricted range from 1 – 2. The difference between the short- and long-wavelength regions is far less marked than for the equivalent widths. The lines also show better internal consistency, the largest being C IV λ1550 with a range of a factor of 2. Although the ratios of peak intensities do not reach the low values found in the equivalent widths, several of the strong lines cluster around

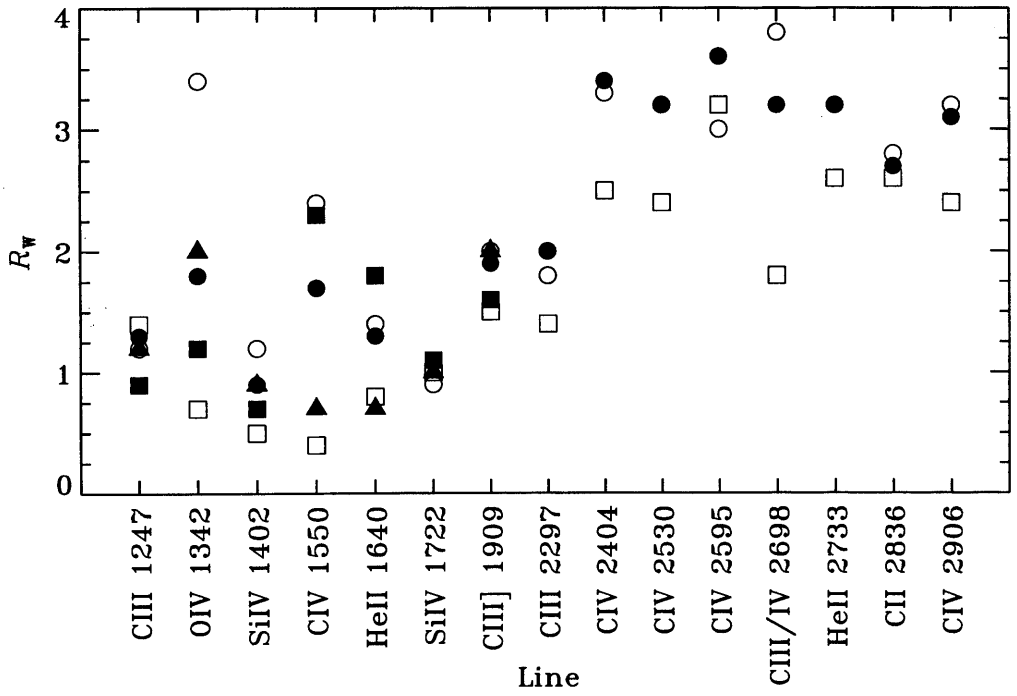

Figure 8.2: The ratio of the equivalent widths of major lines in WR14 WC6 (*filled square*), WR23 WC6 (*open circle*), WR57 WC7 (*filled triangle*), WR90 WC7 (*filled circle*) and WR135 WC8 (*open square*), relative to HD 152270. See the text for details.

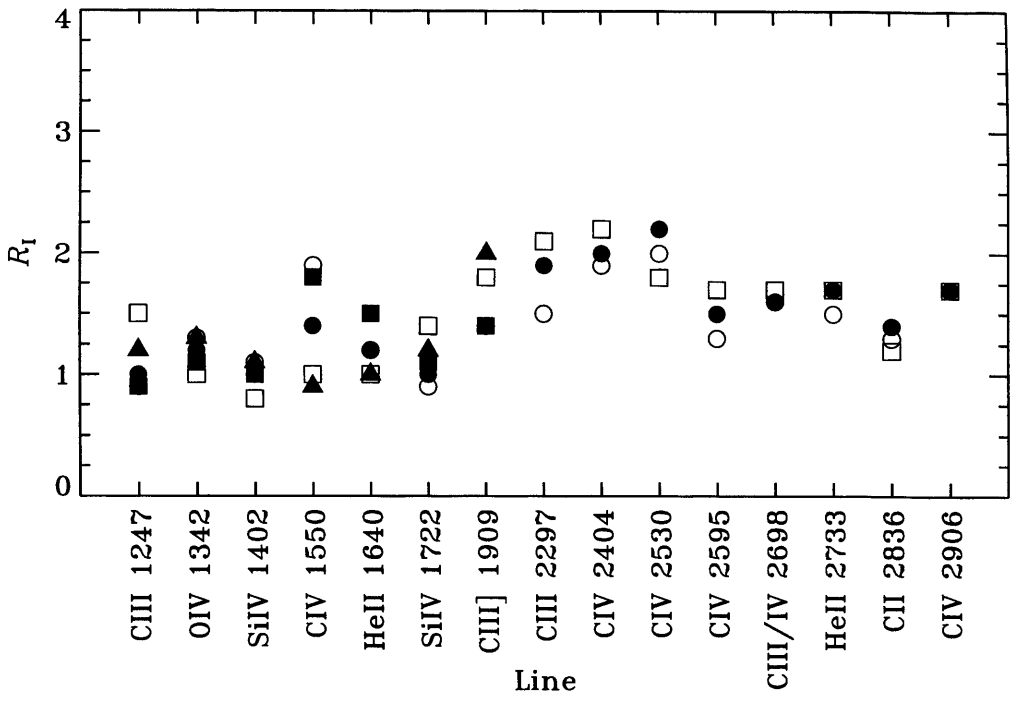

Figure 8.3: The ratio of the peak intensities of major lines in WR14 WC6 (*filled square*), WR23 WC6 (*open circle*), WR57 WC7 (*filled triangle*), WR90 WC7 (*filled circle*) and WR135 WC8 (*open square*), relative to HD 152270. See the text for details.

$R_I = 1$, implying a negligible contribution on the part of the O star. The mean values of $R_W \sim 2$ and $R_I \sim 1.5$ suggests that the O star contributes only 1/2 – 1 times the luminosity of the WR star, on the lower limit of the luminosity ratio from the optical in § 8.1.

8.5 Terminal velocity

The terminal velocity has been determined from the blue limit at zero intensity of saturated lines, v_{black}, and the deepest part of strong, unsaturated lines. The velocities corrected to the systemic velocity are given in Table 8.4 and the mean value is very similar to the value derived by Prinja et al. (1990). The C IV λ1548 and Si IV λ1393 lines also show a discontinuity or change of slope on the blue edge of the line, which has been interpreted by Prinja et al. as evidence of the O star. The terminal velocity

Table 8.4: Measured terminal velocities in HD 152270 from IUE

C III λ1175	C III λ1247	C II λ1334	Si IV λ1393	Si IV λ1402	C IV λ1548	C III λ1909	Mean
−2026	−2141	−1913	−2262	−2218	−2346	−2206	−2159 ±147

derived, 2900 km s^{-1} is similar to other O stars of this type. However, unlike the situation in γ^2 Vel these features show no real change with phase, so it is not clear that they do indicate to spectrum of the O star. Also, the Si IV λ1393 line would have to be an unusually strong wind line to be visible. There is significant variation at the position of the N V λ1239, 1243 resonance doublet, which is also expected to be visible in the O-star spectrum, but no clear indication of the terminal velocity (see § 8.7.4).

8.6 System parameters

To model the shock zone various system parameters need to be defined. The orbital velocity,

$v_{\rm orb} = (K_{\rm O}+K_{\rm WR})/\sin i = 280$ km s^{-1}

with $K_{\rm O}$ and $K_{\rm WR}$ taken as 45 and 150 km s^{-1} respectively, and $i = 45°$. Combined with the terminal velocity of the WR wind, $v_\infty = 2160$ km s^{-1}, the offset angle of the cone, by equation 5.6, $\delta = 7°$. The mass-loss rate of the WR star is given by Prinja et al. (1990) as 1×10^{-4} M$_\odot$ yr^{-1} and revised to 9×10^{-5} M$_\odot$ yr^{-1} by Willis (1991).

The spectral classification of the O star is not precisely determined but from the discussion in § 8.1 it is probably O5V. Certainly it is not particularly luminous. For O5 – O7 stars Lamers & Leitherer (1993) give mass-loss rates of $(0.5 - 1.7)\times10^{-6}$M$_\odot$ yr^{-1} and $v_\infty = 2300 - 2900$ km s^{-1}. Similarly Prinja et al. find a wide range of mass-loss rates, $\dot{M} = (0.1 - 5)\times10^{-6}M_\odot$ yr^{-1} for O stars and Howarth et al. (1997) find $v_\infty = 2890$ km s^{-1} for O5V stars. Adopting $v_\infty = 2160$, and $\dot{M} = 9 \times 10^{-5}$ for the WR star and $v_\infty = 2890$ km s^{-1}, and $\dot{M} = 1 \times 10^{-6}M_\odot$ yr^{-1} for the O star, equation 3.1 yields

a momentum ratio, $\mathcal{P} = 75$. By equation 5.4 the stagnation point, $x_0 = 0.90$, and by equation 5.5, the opening angle of the cone, $\theta = 27°$.

8.7 Line variations

As in γ^2 Vel the lines which show the largest variation are the resonance and low-excitation lines and not the high-excitation lines. In a short-period system such as HD 152270 very little, if any, of the undisturbed WR wind will be seen at positive velocities. The volume close to the two stars will be occupied by the O-star wind, the shock zone, and the WR wind will only reach a small fraction of the terminal velocity. As a result any selective absorption will take place to the blue of the rest wavelength, in emission lines and in the P-Cygni absorption. In the emission peak selective absorption by the wind can, at most, remove only the contribution of the O-star, which for the continuum is estimated at 1/2 – 2/3 of the combined pseudo-continuum luminosity. Also, no significant variation is expected near the terminal velocity. In the plots there are usually an average of 3 spectra merged together are each phase, of which only six have sufficiently good coverage. The phases used are photometric, derived from the ephemeris given earlier (§ 8.3.1).

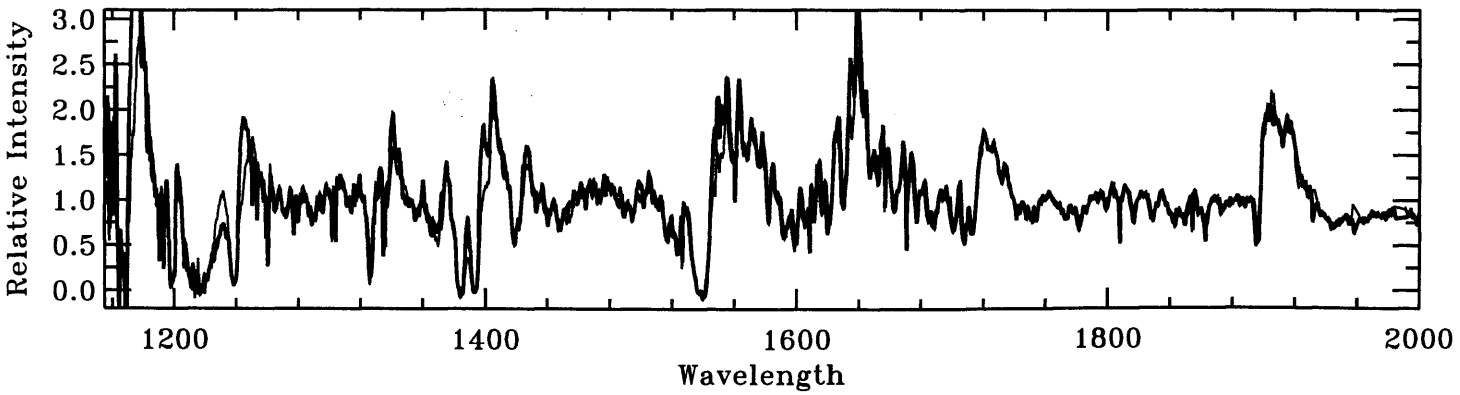

Figure 8.4: The IUE short wavelength region at $\phi = 0.08$ (*thin line*) and $\phi = 0.51$ (*thick line*). See text for details.

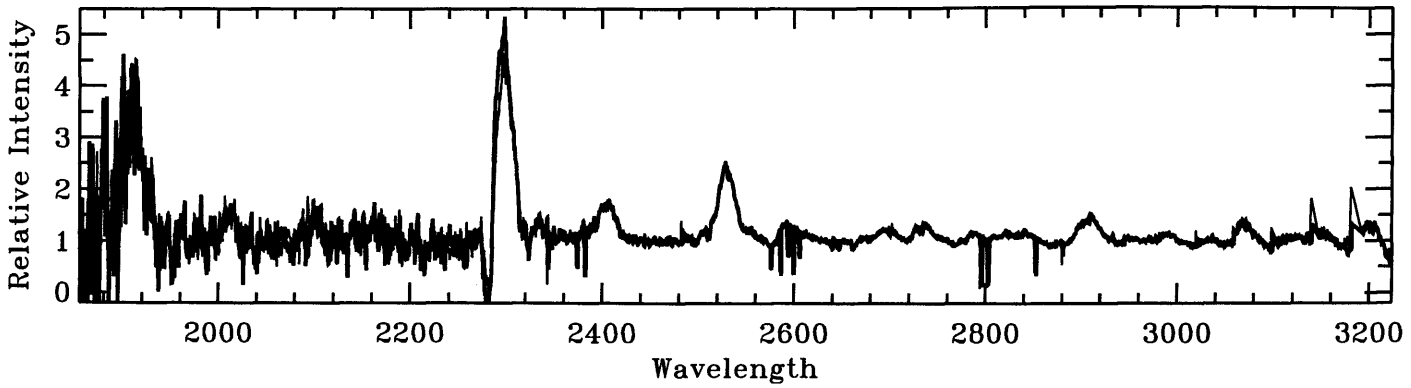

Figure 8.5: The IUE long-wavelength region at $\phi = 0.14$ (*thin line*) and $\phi = 0.58$ (*thick line*). See text for details.

8.7.1 He II λ1640

The region around the He II λ1640 line also contains C III and C IV lines at the same wavelength and the C III λ1625 and λ1645 lines (Hamann et al. 1992). Despite its complicated structure the line shows a clear progressive increase in emission from ϕ = 0.0 – 0.5 and decay during the second half of the orbit (Figure 8.6). During ϕ = 0.5 – 1.0 the whole profile shows a slight shift to the red which persists to ϕ = 0.84, even after the emission has returned to approximately its original level. The maximum change in intensity is $\sim$ 0.7 of the pseudo continuum, and applies to a large part of the λ1640 profile. The extent of the variation reflects the large number of components of the line, however, the early changes, prior to ϕ = 0.27, which occur to the red of the principal line are not immediately explained. The level of the variation corresponds to the complete removal of the O-star continuum for a luminosity ratio $L_{\rm O}/L_{\rm WR} = 2$.

8.7.2 C IV λ1548, 1550

The C IV λ1548, 1550 doublet (Figure 8.7) shows the same even, progressive change in emission as He II λ1640, although the profile is confused by the interstellar lines. The maximum change in intensity is $\sim$ 0.6 of the pseudo continuum. During the later phases the saturated P-Cygni and the absorption at $\sim$ λ1560 also show the small shift to the red. The O5 companion is also expected show the C IV λ1548, 1550 doublet in emission with a possibly saturated P-Cygni absorption, which will complicate the interpretation of the variations.

8.7.3 Si IV λ1393, 1402

The two components of the Si IV λ1393, 1402 doublet (Figure 8.8) show a rather different behaviour. The blue component of the emission is the first to change and by ϕ = 0.27 has increased by $\sim$ 50% while the red component shows little variation. At $\phi \sim$ 0.5 both components have reached their peak intensities, showing changes of $\sim$ 0.7 and 0.3 of the pseudo continuum, for the blue and red components respectively. Changes during the second half of the orbit reflect those of the first. The intensity saddle

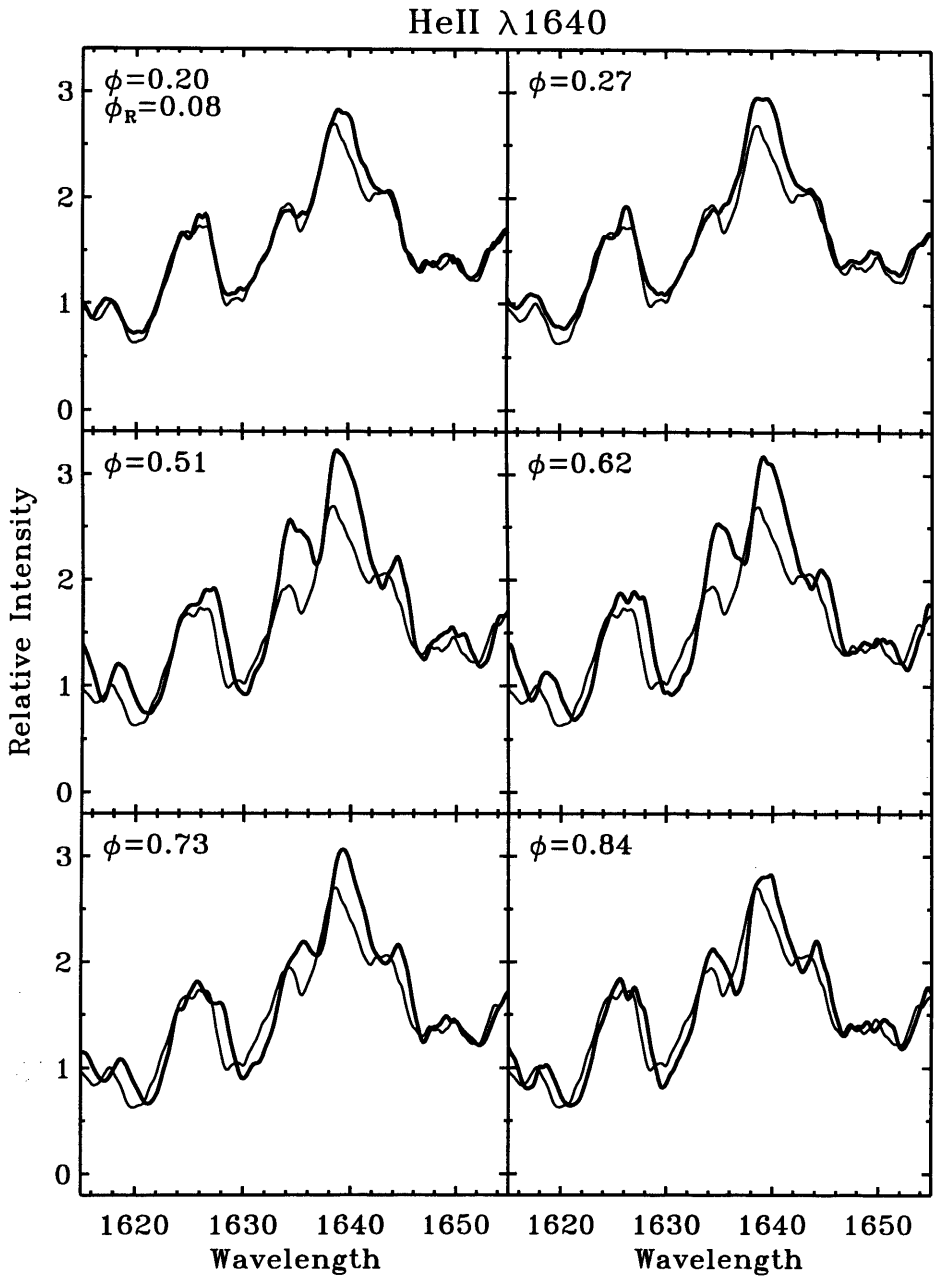

Figure 8.6: The He II λ1640 emission line blended with lines of C III and C IV. Six orbital phases are shown (*thick line*) relative to the reference phase, ϕ_R 0.08 (*thin line*). The phases used are photometric with $\phi = 0$ corresponding to superior conjunction of the O star, i.e. behind the WR star. To aid comparison the spectra have been slightly smoothed (σ = 0.2 Å) and the gaps have been filled. See text for details.

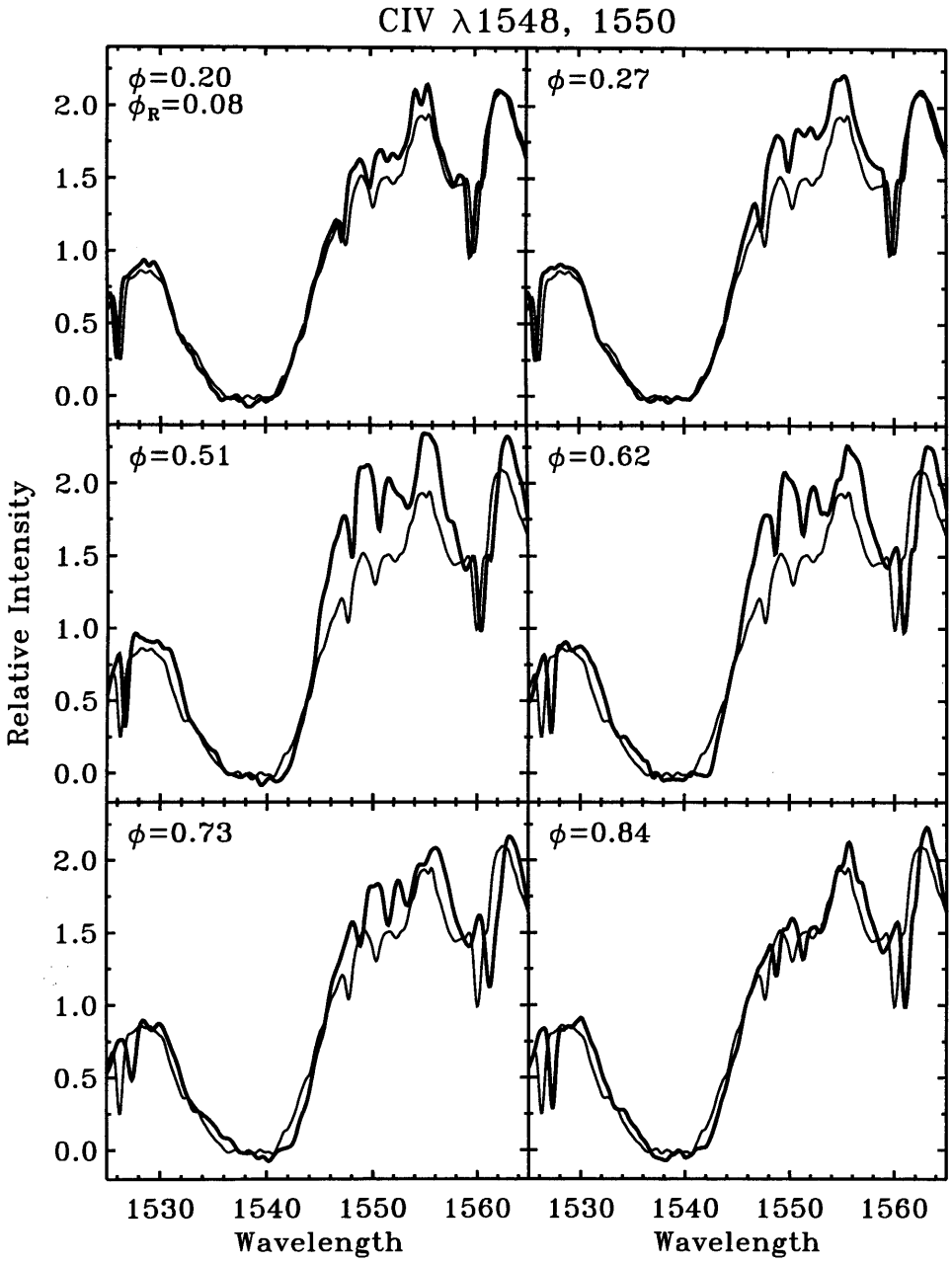

Figure 8.7: The region around the C IV λ1548, 1550 P-Cygni profile. The line is cut into by the C IV interstellar lines of C IV and C I λ1560. Other details are as Figure 8.6.

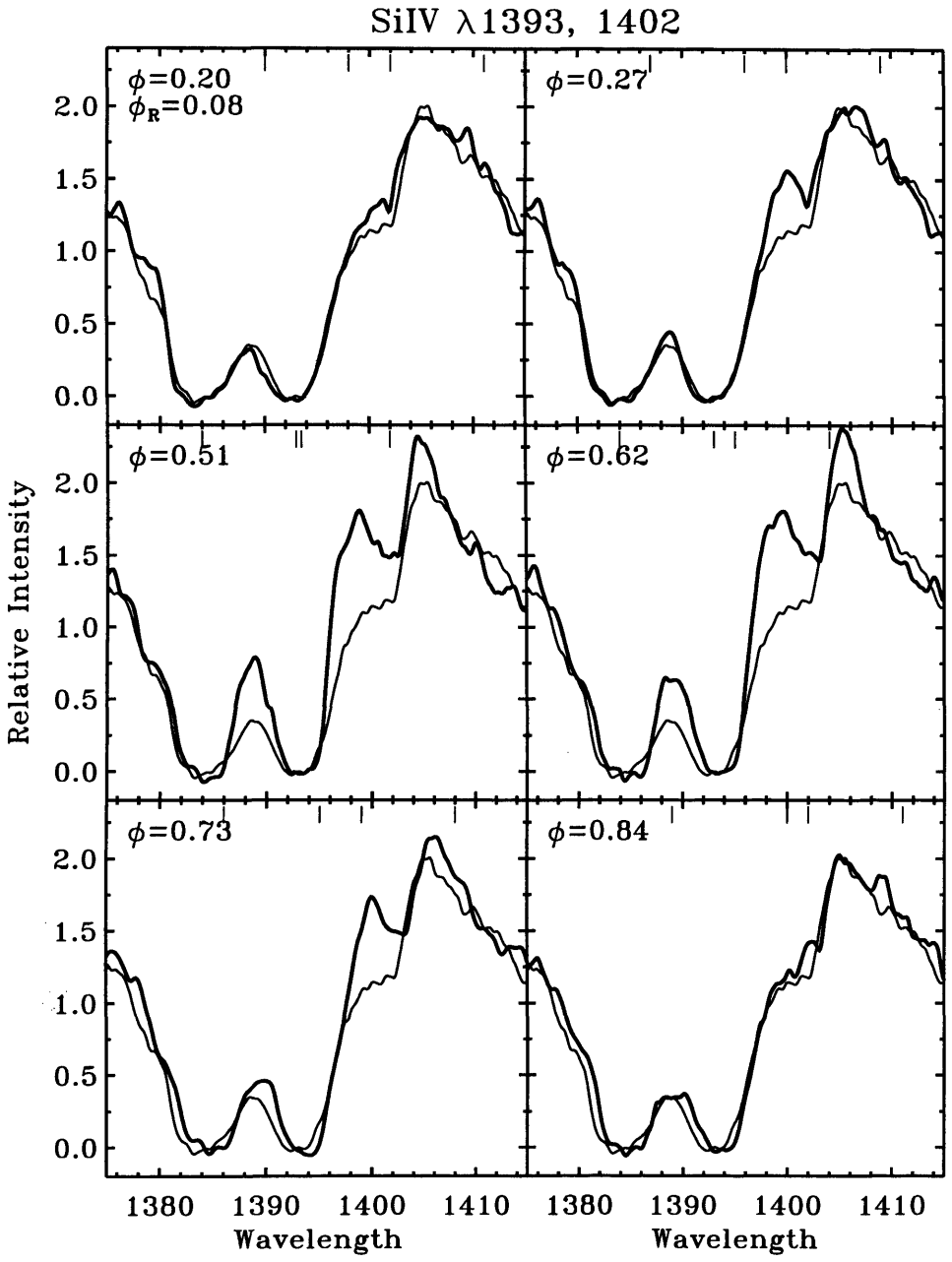

Figure 8.8: The Si IV λ1393, 1402 P-Cygni profile. The short vertical bars at the top of each panel show the expected wavelengths of the peaks of the excess emission from the shock zone. See text for details. Other details are as Figure 8.6.

between the two components of the P-Cygni absorption also follows the variation of the emission, and the P-Cygni absorption also shows the small shift to the red of $\sim$ 1Å during the second half of the orbit.

The blue component of the emission is expected to show the most variation because it is absorbed by the red component in the wind. Conversely the red component of the emission is not expected to show much variation, because it lies on the absorption edge, and certainly not between $\phi = 0.27$ and 0.51, where it shows the largest change. This additional emission does not show the progressive change in velocity that would be expected of the moving features found by Lührs (1997) in the C III λ5696 line, but simply seems to emerge at about the rest wavelength.

The Si IV λ1393, 1402 doublet is also expected to appear in absorption in the O star but is usually weak enough that it may be safely ignored. In single early O stars it is certainly weaker than the N IV λ1718 line which is only barely visible (see later discussion in § 8.7.10).

8.7.4 C III λ1247

The C III λ1247 line (Figure 8.9) is blended with the N V λ1239, 1243 resonance doublet which is a strong feature of the O-star spectrum. The C IV λ1230 UV multiplet 11.14 is present in single WC stars but it is not clear what influence it has here. The profile is further complicated by the close proximity of the H-Lyα line which affects the extreme blue edge of the profile. The behaviour of the emission variation is similar to what has been seen in the other lines; there is a progressive rise and fall in intensity of $\sim$ 0.8 of the pseudo continuum around the orbit. However, there is no shift in the absorption during the second half of the cycle. The blue edge of the P-Cygni profile shows a variation almost identical to, but in complete anti-phase to the emission line variation. The wavelength and general behaviour is what might be expected of the increasing visibility of the N V λ1239, 1243 lines, but the variation is superficially quite unlike that seen in γ^2 Vel. Assuming a terminal velocity of 2900 km s^{-1} these variations extend well beyond the edge of the line, ultimately reaching into the core of Lyα, suggesting that the line is saturated to $v_\infty > 3500$ km s^{-1}. Fur-

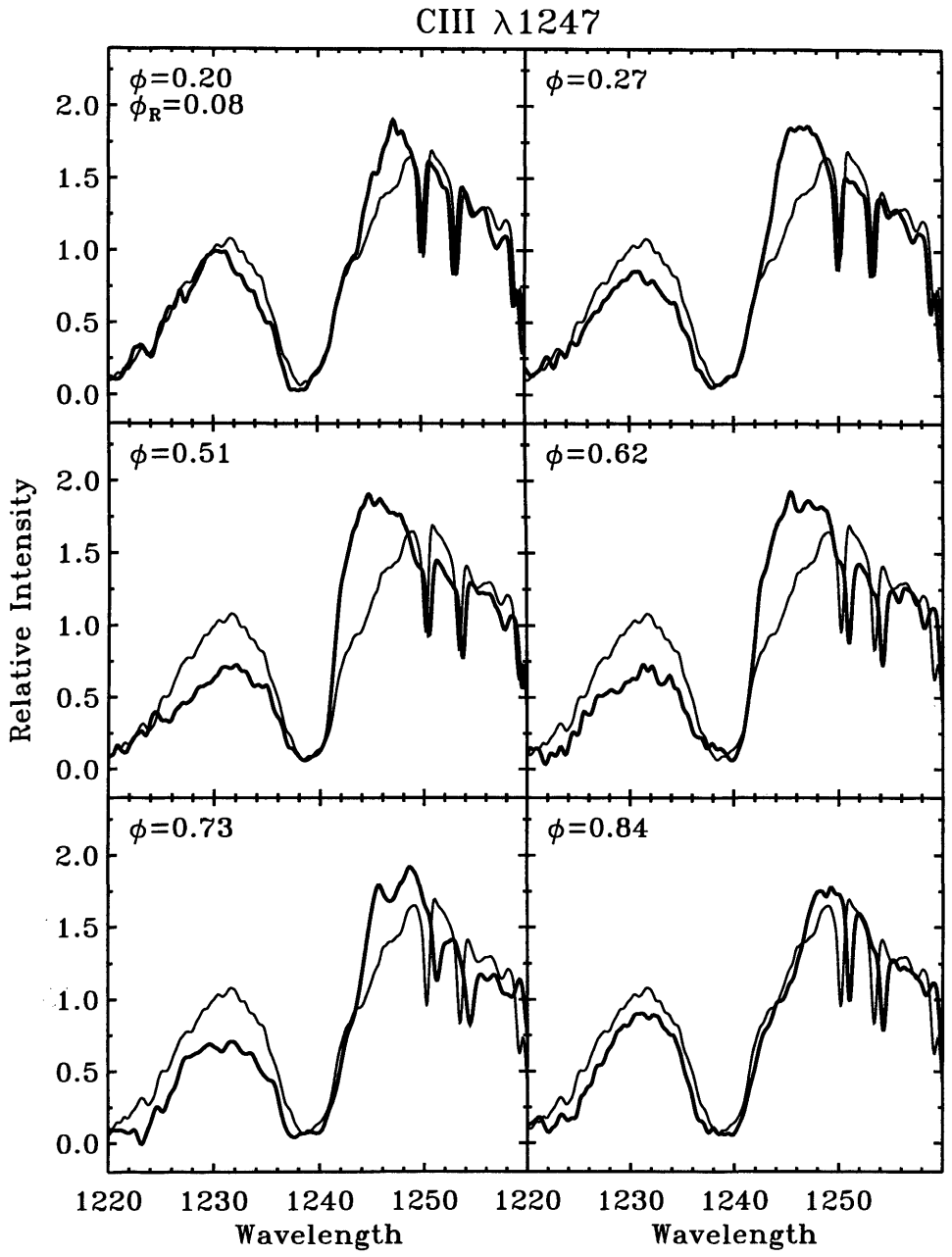

Figure 8.9: The region around the C III λ1247 P-Cygni profile with the red wing of Lyα. The sharp absorptions are the S II λλ1250, 1253, 1259 and Si II λ1260 interstellar lines. Other details are as Figure 8.6.

thermore, this region remains weak during the second half of the orbit when the O star is returning to the back of the system. In one sense the variations are (almost) consistent with Lyα, as this may be expected increase the absorption as the O star passes to the front of the system. However, the development of the profile and the lack of any corresponding variation shortward of Lyα (cf., Figure 8.12) argue against this interpretation.

8.7.5 C III] λ1909

The semi-forbidden C III] λ1909 line in HD 152270 is considerably broader than in γ^2 Vel and is blended with the C III λ1923 line (Figure 8.10). A similar structure is also seen in other, single WC stars with high terminal velocities, and Willis et al. (1986) offered the Fe III UV multiplet 34 lines $\lambda\lambda$1895, 1914, 1926 as possible contributors. When modelling the line Hamann et al. (1992) naturally produced the lumpy structure and the central absorption with just C III] λ1909 and C III λ1923. The profile shows complex variations in both the red wing and peak of the emission line, and in the P-Cygni absorption. However, these are weak, reaching only $\sim$ 20% of the pseudo continuum, and irregular. The variation of the emission around the cycle takes the form of a general flattening of the profile with the emission peaks being suppressed. Parts of the peak are particularly noisy, as the line is close to saturation on some of the *IUE* spectra (cf., 6.1), so parts of this variation are uncertain. From $\phi \sim 0.44$ to $\phi = 0.6$ the absorption at $\sim$ 1912Å, in the peak of the emission, sharpens and moves slightly to the red. By $\phi = 0.73$ this feature is not clearly identifiable and the profile has a flat-topped appearance. The variation on the red edge of the emission, at $\sim$ λ1922Å, follows a similar pattern to the emission components of other lines and may represent the selective absorption of the C III λ1923 line. The general variation of the emission line is less than in γ^2 Vel and considerably less than the other emission lines in this star.

The P-Cygni absorption also shows small but detailed variation. During the early part of the orbit it shows a slight weakening, by $\sim$ 10%, but no movement. By $\phi =$ 0.40 the line has deepened again has begun to move to the red, and by $\phi = 0.51$ the

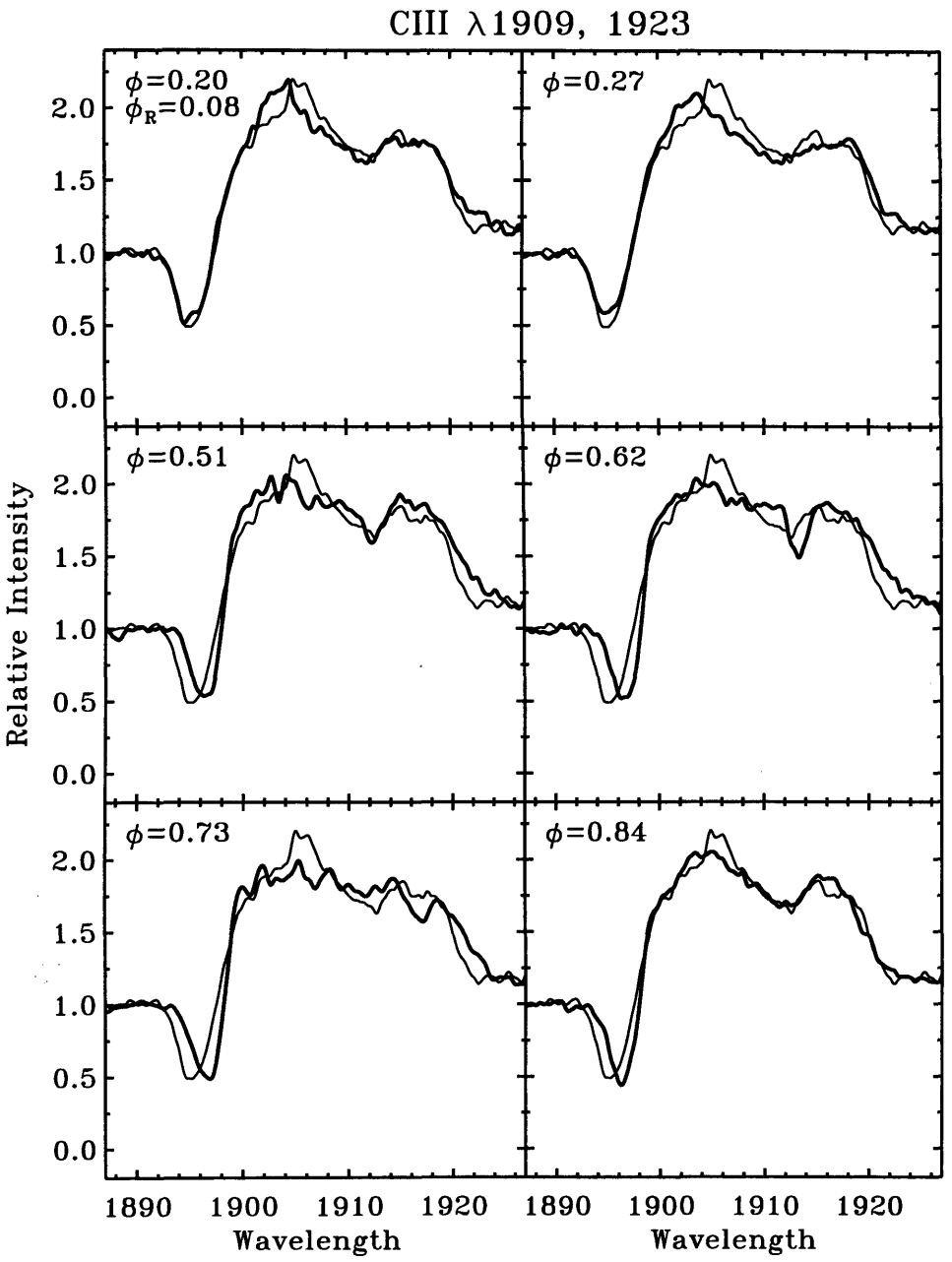

Figure 8.10: The principal feature is the C III λ1909 P-Cygni profile blended with a weaker C III λ1923 emission. Further details are as Figure 8.6.

absorption has moved $\sim$ 1Å to the red. Between $\phi = 0.51$ and $\phi = 0.73$ the profile continues to edge to the red but by $\phi = 0.84$ the core of the absorption has moved $\sim$ 0.5Å back to the blue, and it jumps the remaining 1.5Å by $\phi = 0.08$.

8.7.6 C III λ2297

The C III λ2297 line (Figure 8.11) lies in a spectral region where the sensitivity of the *IUE* detectors increases substantially from blue to red, and also where interstellar absorption takes its highest toll. The signal-to-noise ratio in this region is poor, particularly in the continuum to the blue of the line and the P-Cygni absorption, even in well exposed spectra. The line of the continuum through the profile is quite strongly curved and the rectified profile is sensitive to details of the nearby continuum. There is also a problem with the background subtraction on the blue edge of the P-Cygni absorption which, in a few spectra, results in significant negative fluxes. The profile variations are restricted to the emission peak which broadly follow the pattern of the other lines. However, the variations are much less progressive and less symmetrical than previously seen, and there is apparently a significant change between $\phi = 0.58$ and $\phi = 0.62$. The amplitude of the variation reaches 0.8 (similar to other lines) and 1.0 of the pseudo continuum at $\phi = 0.48$ and $\phi = 0.58$ respectively. As with the Si IV λ1393, 1402 line (Figure 8.7.3) the variation does not appear to be consistent with the moving features of the Lührs model.

Despite the noisy profiles there is very little indication of any real variation in the P-Cygni absorption. Where the fluxes are most reliably determined the profiles show no significant variation and are consistent with the reference profile. The best agreement is during the later phases, $\phi = 0.62 - 0.84$, which is when most of the other lines have shown a small shift.

8.7.7 C III λ1175

The line at C III λ1175 shown in Figure 8.12 is a complex blend of some six C III lines which share the same lower level as the C III λ2297 line. The line lies at the blue limit of the *IUE* short-wavelength range where the signal to noise drops rapidly and the

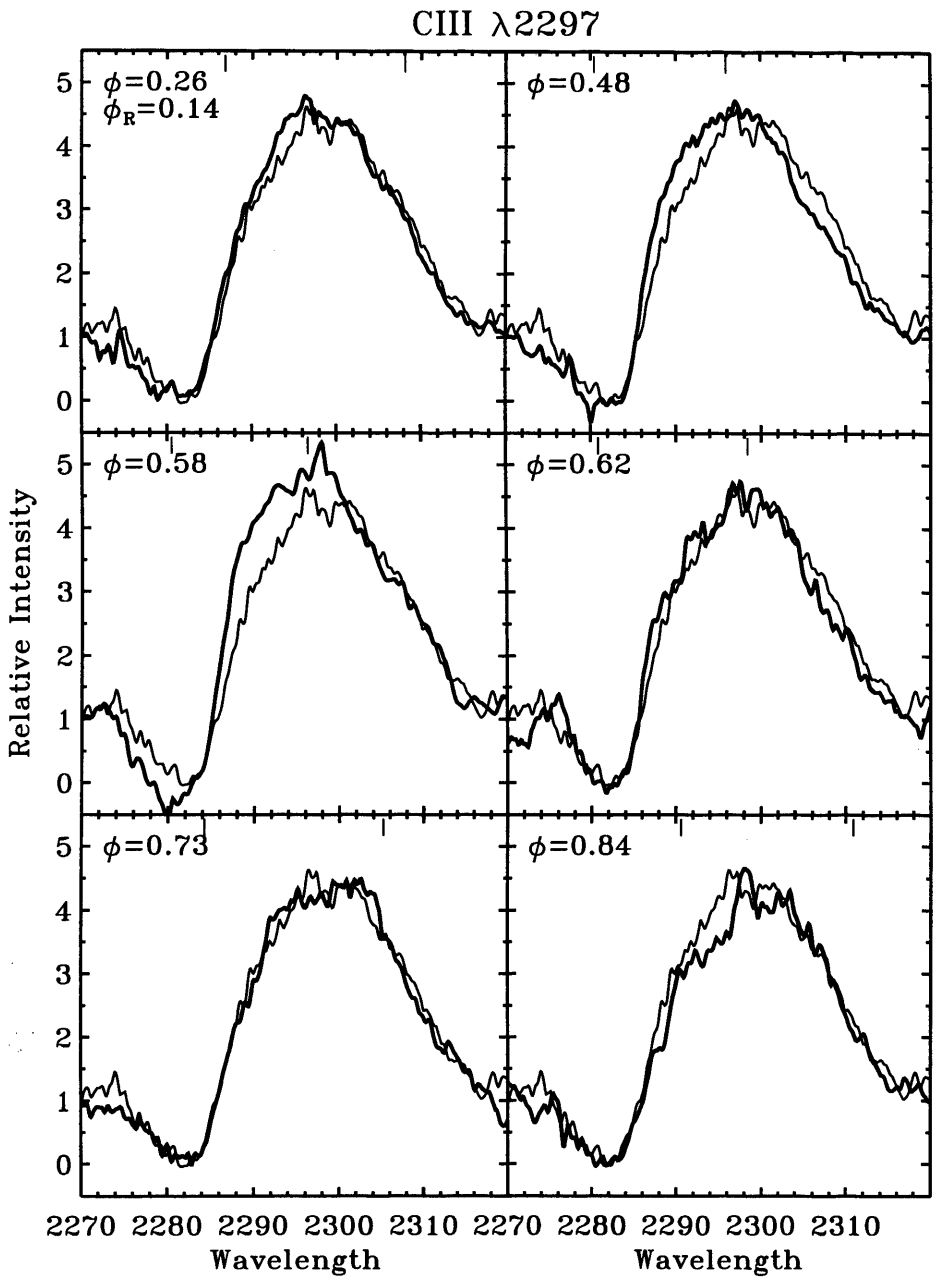

Figure 8.11: The C III λ2297 P-Cygni profile. The orbital phases are different to those of the *IUE* short-wavelength spectra. The blue side of the line suffers from poor signal to noise and at two phases, $\phi = 0.48$ and 0.58, problems with the background subtraction produce negative fluxes. Further information is given in the text and other details are as Figure 8.6.

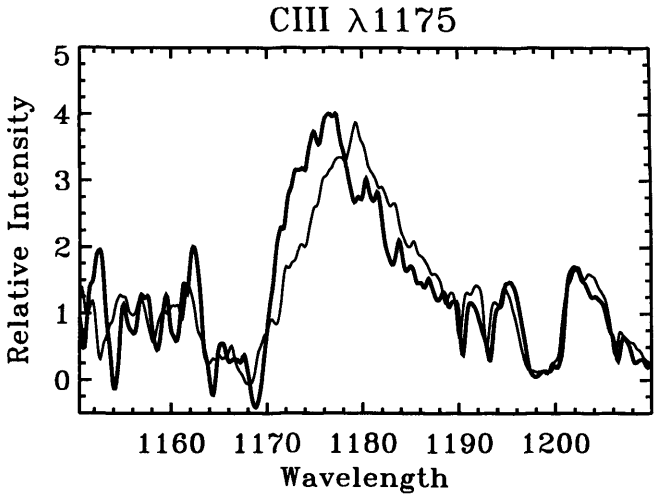

Figure 8.12: The C III λ1175 line for two phases, $\phi = 0.08$ (*thin line*) and 0.51 (*thick line*). The maximum variation is about equal to the level of the pseudo continuum and the profile bears a striking resemblance to that of the C III λ2297 line (Figure 8.11) at $\phi = 0.48$. The other features visible include S III λ1202 and the C I λ1190, 1193 interstellar lines.

rectification is least reliable. During the orbital cycle the variation in the emission follows the behaviour seen in the other lines although the same level of detail is not present. The maximum variation is about the level of the pseudo continuum and the profile seems to closely match that of the C III λ2297 line even to the extent of showing the same anomalous absorption at $\phi \sim 0.5$ on the red wing of the emission. The absorption suffers from very poor signal to noise and shows no clear variation.

8.7.8 C II λ1335

The region around λ1340 Å (Figure 8.13) contains the C II λ1335 line seen probably only in absorption, the C II λ1335 interstellar lines and the weak O IV λ1338, 1342 P-Cygni profile. During the orbital cycle the C II λ1335 shows only a slight weakening and during later phases a shift of 1 – 2Å to the red, similar to the shift seen in other lines.

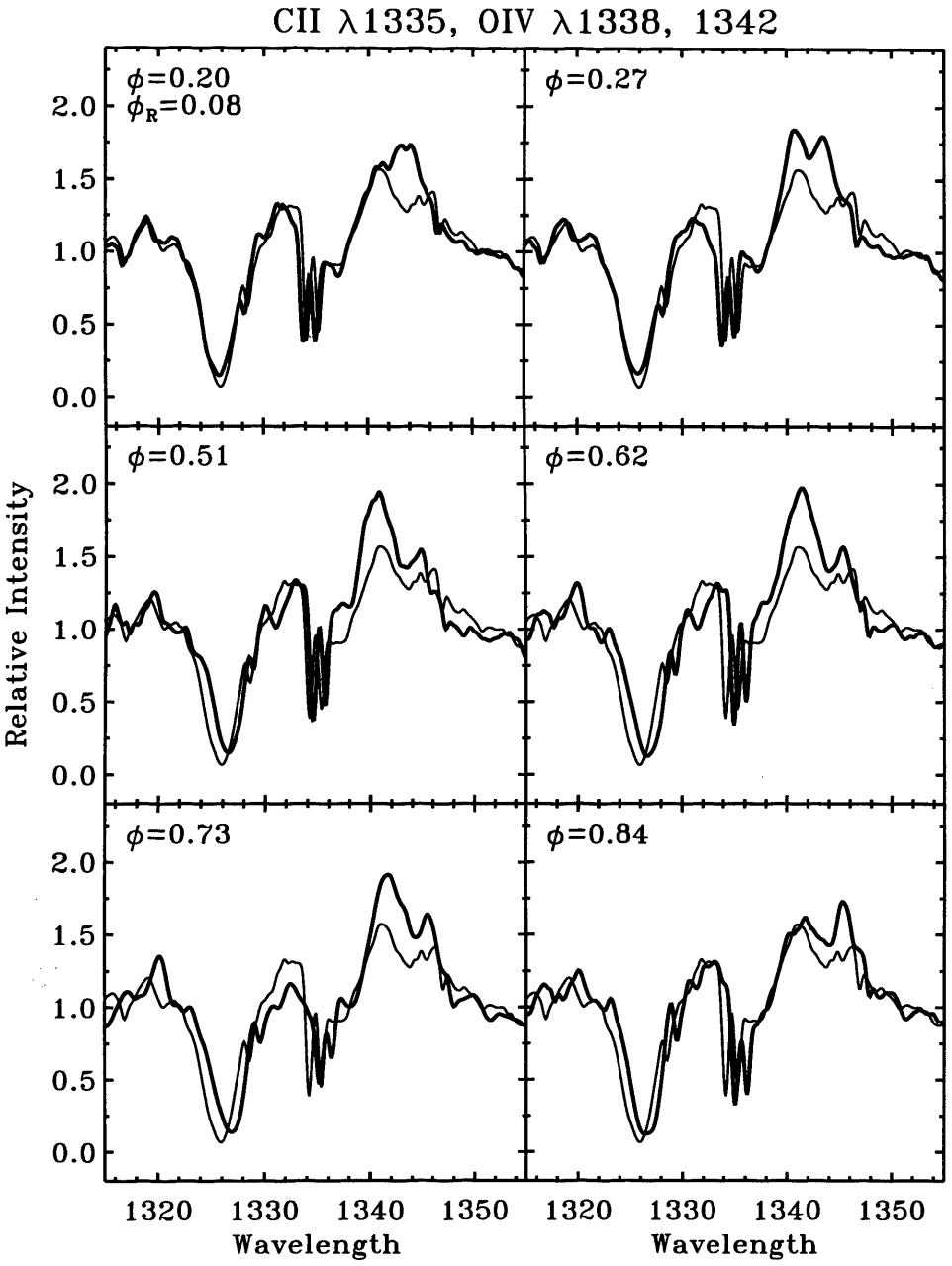

Figure 8.13: The C II λ1335 line seen in absorption with its interstellar lines, and the weak P-Cygni profile of the O IV λ1338, 1342 doublet. Other details are as Figure 8.6.

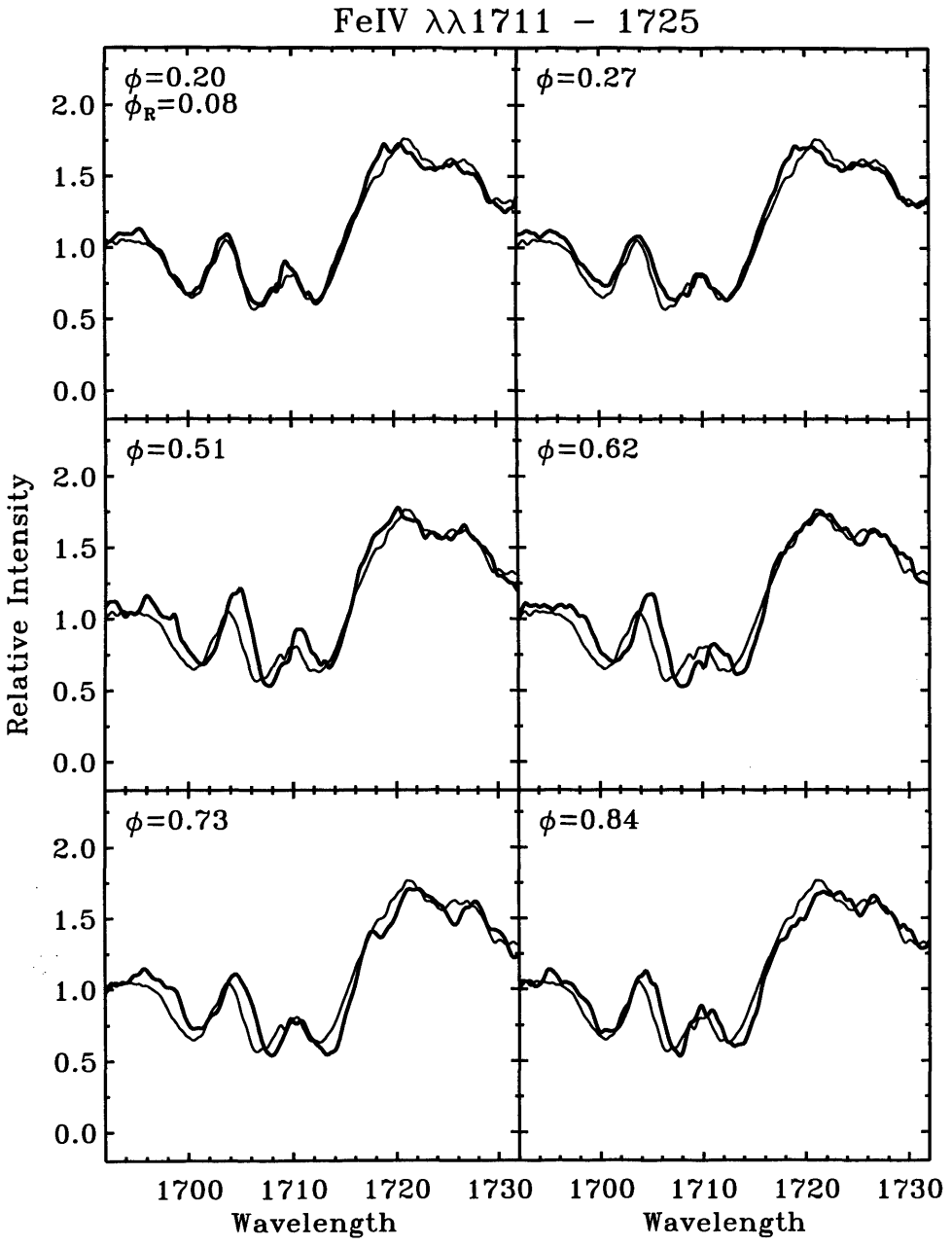

Figure 8.14: The Fe IV λλ1711 – 1725 pseudo continuum and the Si IV λ1722, 1727 emission lines. Other details are as Figure 8.6.

8.7.9 O IV λ1338, 1342

The O IVλ1338, 1342 emission peak (Figure 8.13) shows an irregular progression broadly following what has been seen before in the other emission lines. However, there is significant variation to the red of the rest wavelength where none is expected. The maximum variation is ~ 0.4 of the pseudo continuum.

8.7.10 Fe IV λλ1711 – 1725

The region around λ1720Å (Figure 8.14) contains several groups of lines due to Si IV, S III, Al III and Fe IV. There is a broad emission complex trailing off to the red usually attributed to Si IV λ1722, 1727 but which probably has other contributors. The absorption is mostly due to the stronger lines of the Fe IV pseudo continuum. During the cycle this region shows only very minor variations, mostly slight shifts to the red of small individual features. The absorption lines show rather more obvious shifts and small changes in intensity, following the behaviour seen previously in other strong absorptions.

The N IV λ1718 line, which is expected to be a strong feature of the O-star spectrum, also lies in this region but it is not unambiguously visible. At $\phi = 0.27$ and 0.73 the O star will have its maximum negative and positive velocity and the profile at λ1718Å does show some variation but it is not consistent with the orbital motion of the N IV line in the O star. In fact the intensity at this wavelength seems to cycle up and down with maximum at $\phi = 0.27$ and minimum at $\phi = 0.73$. The maximum variation of this feature is ~ 0.3 of the pseudo continuum, which is close to what would be expected of the N IV λ1718 line, if the luminosity ratio $L_{\rm O}/L_{\rm WR} = 2$, but the behaviour is not consistent.

8.8 Profile modelling

The clearest diagnostic in these variations is the behaviour of the P-Cygni and other absorptions. The shift to the red at $\phi \sim 0.5$ is precisely what is predicted by the

model and is due to absorption by material in the shock zone. See the example in § 5.7.3, Figure 5.11. To generate the observed shifts the O star has to be viewed almost along the outer boundary of the shock zone. Given the parameters of the system summarised in § 8.6 the combination of inclination and cone opening angle are too small to produce this effect. A simple reduction in the mass-loss rate of the WR star from its rather extreme value to $\dot{M} = 5 \times 10^{-5}$ increases the opening angle of the cone to $\theta = 37°$. After some experimenting, values of $i = 45°$, and $\theta = 40°$ were adopted.

The ionization balance of the wind has been determined from C II λ1335 and C III] λ1909 in exactly the same way as for γ^2 Vel, and a very similar pattern of ionization results. See § 7.8 for the details. As for γ^2 Vel the C III λ2297 and C IV λ1548, 1550 are saturated out to the terminal velocity and provide no useful constraints on the ionization balance or on β, which was assumed to be 1.0. In single WC stars the C II λ1335 line is very nearly saturated but it appears slightly weaker, by $\sim$ 10%, in the combined spectrum of HD 152270. The C III] λ1909 P-Cygni absorption in single WC stars is $\sim$ 0.3 of the pseudo continuum but in HD 152270 it is a little stronger at 0.5 of the pseudo continuum. The ionization balance was determined by fitting the profiles and then used to model other lines.

8.8.1 C II λ1335

Figure 8.15 shows the fit to the C II λ1335 line at $\phi = 0.08$ and 0.51. In order to fit broad wings of the line it was necessary to set the turbulent velocity of the wind, $v_{\rm turb} = 300$ km s^{-1}, as opposed to 200 km s^{-1} which is used for the other profiles. It is possible that this reflects a real increase in turbulence at the limit of the wind. The same value was used for the WR wind and the shock zone, which, perhaps surprisingly, suggests little difference in turbulent velocity between the two. At $\phi = 0.08$ the model provides an excellent fit to the line while at $\phi = 0.51$ when the system is viewed along the edge of the shock zone the fit is less good. The observed shift on the blue side of the profile has been followed but narrowing of the line and the slight change in intensity have not. The change in intensity occurs early in the orbit, so is

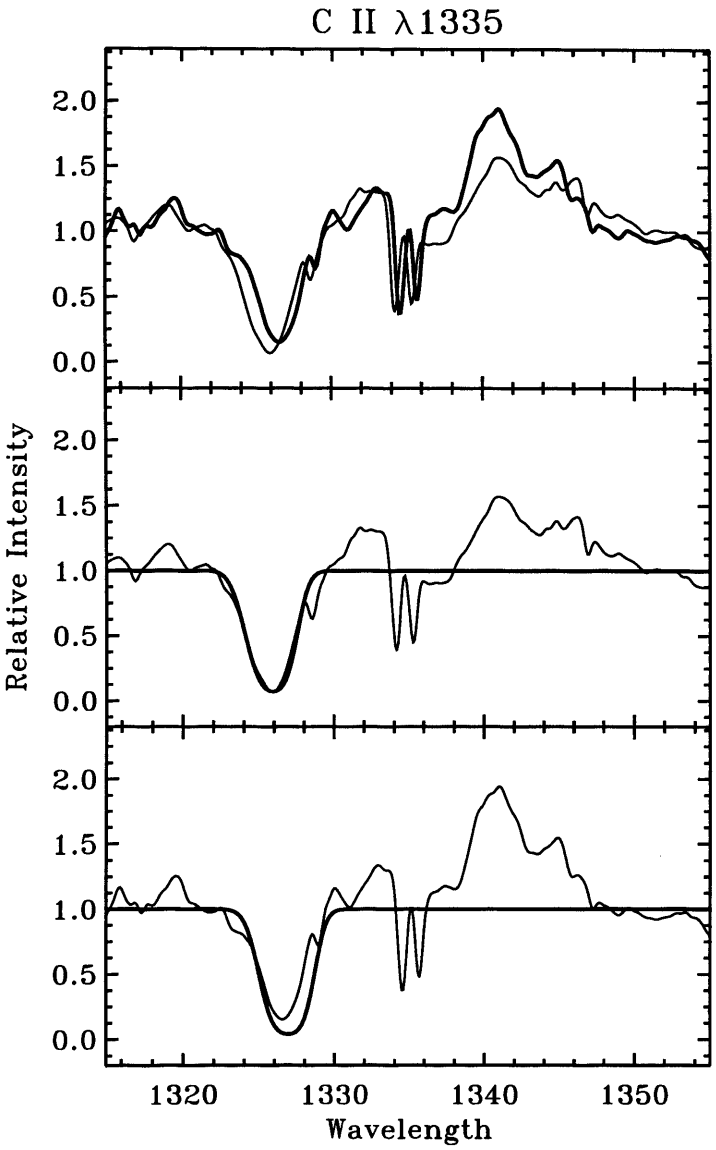

Figure 8.15: The C II λ1335 line calculated profile. The top panel shows the observed profiles at $\phi = 0.08$ (*thin line*) and $\phi = 0.51$ (*thick line*). The lower two panels show the observed (*thin line*) and calculated (*thick line*) profiles at $\phi = 0.08$ (*middle*) and $\phi = 0.51$ (*bottom*). At $\phi = 0.08$ the model provides an excellent fit to the line while at $\phi = 0.51$ when the system is viewed along the edge of the shock zone the fit is less good. The observed shift on the blue side of the profile has been followed but narrowing of the line and the slight change in intensity have not.

not obviously connected with the shock zone, although it may reflect on the conical approximation to the shock zone.

In single WC stars the C II λ1335 line is nearly saturated, so even if it is diluted by a factor of $\sim$ 2 it should still be visible at $\phi = 0.51$ on the blue edge of the profile. It is a small but significant detail which reveals that at $\phi \sim 0.5$ both the O star and the WR star are seen through the shock zone. The material which normally creates the 'single-star' P-Cygni absorption is replaced by material in the shock zone. It is therefore not possible to consider the variations in terms of a stationary 'single-star' profile and an 'additional' variable component. In fact the effect is visible on all strong P-Cygni and absorption lines. On none of these does the undisturbed wind profile show itself during the 'shifted' phases.

8.8.2 C III] λ1909

The fit to the C III] λ1909 line, Figure 8.8.2, is generally better than for C II λ1335. The adopted ionization balance provides an excellent fit to both the line shape and velocity of the observed profiles at $\phi = 0.08$ and 0.51. There is as slight variation in depth that the model is unable to match. It is interesting to note that at $\phi = 0.51$ both the λ1909 and λ1335 lines are weaker relative to $\phi = 0.08$, and that this variation begins early in the orbit. As with the C II λ1335 line the undisturbed wind profile is not visible during the later phases.

8.8.3 The saturated P-Cygni lines

For the saturated P-Cygni lines such as C IV λ1548, 1550 and C III $\lambda\lambda$1175, 1247, 2297 the wind absorption is saturated across the whole width of the profile. As the O star emerges from behind the WR star the whole contribution of the O-star continuum is progressively added to the profile from about the rest wavelength, ultimately to the red edge of the P-Cygni absorption. Of the strong lines C III λ1247 probably follows this pattern best, while C IV λ1548, 1550 and C III λ2297 show some extra variation in intensity. With additional components contributing to the lines it is difficult to know precisely what should be seen. However, the general level of change of $\sim$ 0.7

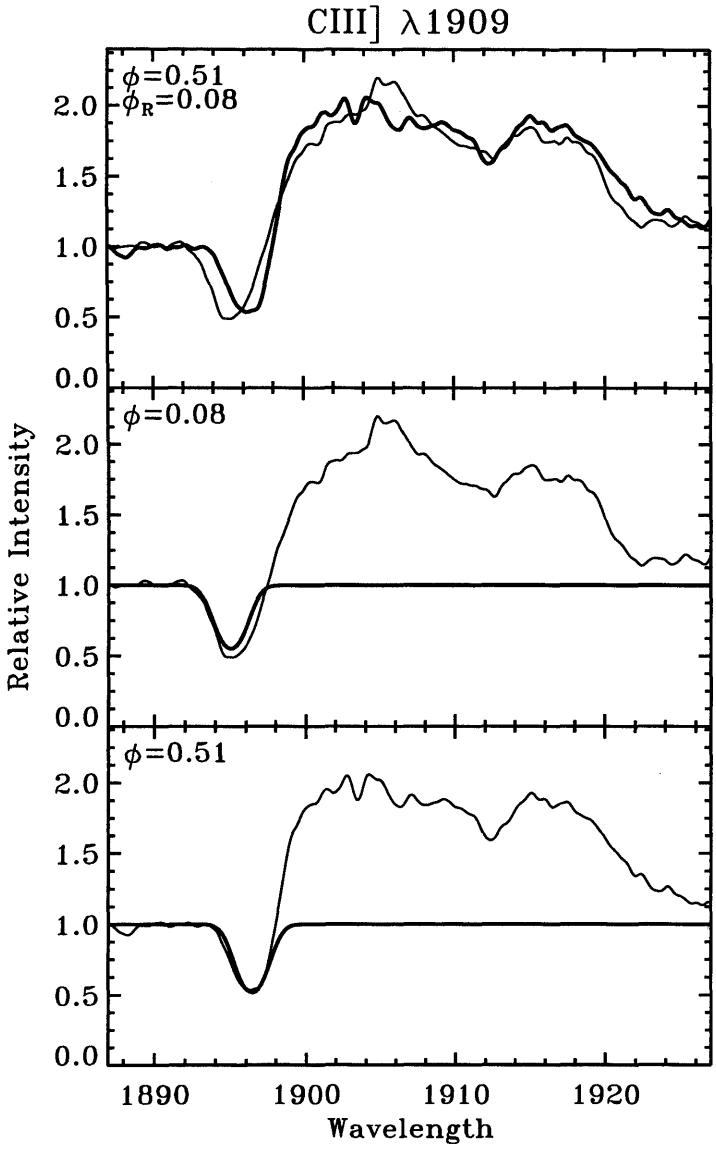

Figure 8.16: The C III] λ1909 line calculated profile. The top panel shows the observed profiles at $\phi = 0.08$ (*thin line*) and $\phi = 0.51$ (*thick line*). The lower two panels show the observed (*thin line*) and calculated (*thick line*) profiles at $\phi = 0.08$ (*middle*) and $\phi = 0.51$ (*bottom*).

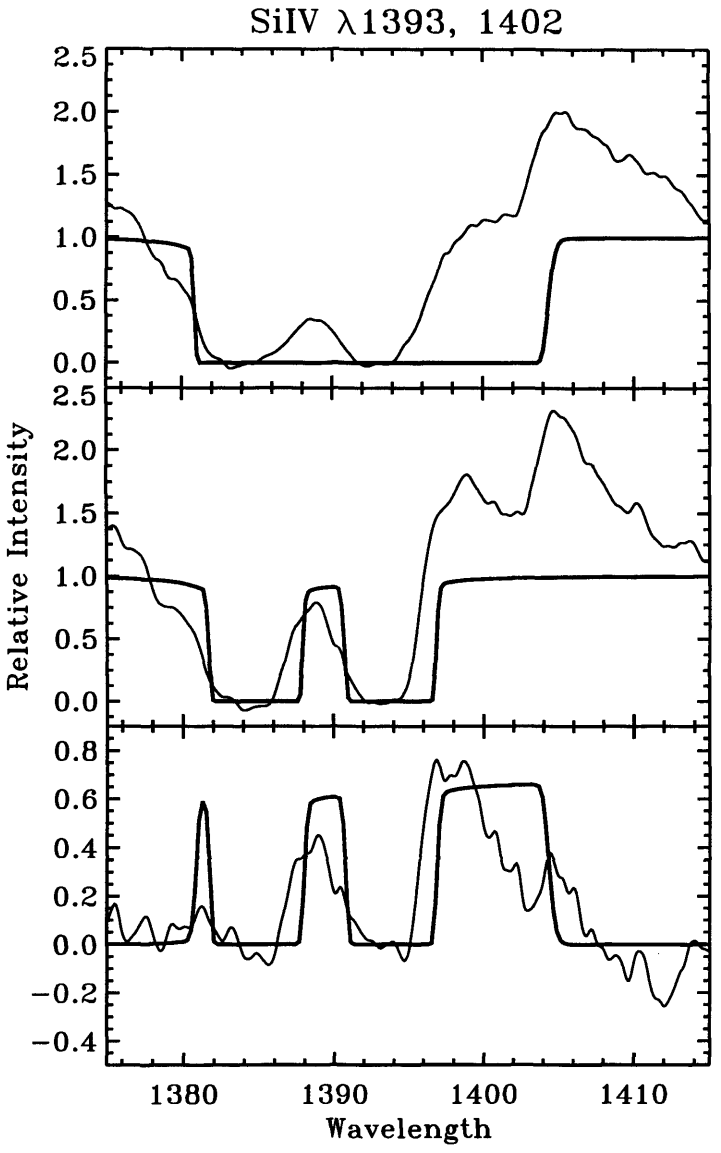

Figure 8.17: The Si IV λ1393, 1402 doublet calculated profile. The top panel shows the observed profile at $\phi = 0.08$ (*thin line*) and calculated profile of the *wind absorption*, not a fit to the profile (*thick line*), superimposed assuming a solar Si/He abundance. The middle panel shows the same for $\phi = 0.51$. The bottom panel show the difference between the two observed profiles (*thin line*) and calculated profiles (*thick line*) in order to show how the model fits the variation.

of the pseudo continuum is certainly the upper limit of what is expected, and the variation of C III λ1175 and 2297 amounting to the whole of the combined continuum requires another explanation.

The Si IV λ1393, 1402 doublet is also saturated out to the terminal velocity but it should be less confused than the stronger lines. However, as in the case of γ^2 Vel, the separation between the components makes it a particularly sensitive test of the lines generated by the model. Figure 8.17 shows the observed profiles at ϕ = 0.08 and 0.51 together with the calculated absorption component due to the wind. At ϕ = 0.08 the selective absorption is saturated across the whole width of the line. The calculated absorption appears too aggressive because there should be some indication of the saddle between the two absorption lines. At ϕ = 0.51 the model fits the shift in velocity and also follows the change in intensity at the saddle point. The correct way to use the model is to compare the differences it predicts with those observed, and that is done in the bottom panel of the figure. The main features are reproduced but there are detailed differences. The calculated profiles are too sharp, probably too strong, and reducing the Si/He ratio from solar, which is used in the figure, by a factor of 2 improves the fit in the region of the saddle point. By adjusting the temperature structure from that assumed it is also possible to improve some parts of the fit, but at the expense of others. The other factor which will have a large impact on the profiles is the luminosity ratio, as this is used to scale the calculated difference before comparison. However, the model takes no account of the excess emission from the shock zone which can equally account for much of the detailed difference.

8.8.4 Fe IV $\lambda\lambda$1711 – 1725

The emission lines at $\sim$ 1720 Å are usually attributed to the Si IV 1722, 1727 lines (e.g., Smith & Willis 1982, Auer et al. 1988) but as with γ^2 Vel modelling the lines reveals that the absorption components at least, are due to Fe IV lines. The three main features in Figure 8.18 are composed of some 10 Fe IV lines. The profiles were calculated using a solar Fe/He ratio and they fit the observed features well in both wavelength and relative strength. The shift in velocity and the accompanying change in strengths between ϕ = 0.08 and 0.51 is also well matched although there are differences of detail. At ϕ = 0.08 the model suggests absorption running into the emission peak which would lead to some variation at these wavelengths, but this is not seen. It is possible that there are errors in the f-values of the weak lines contributing

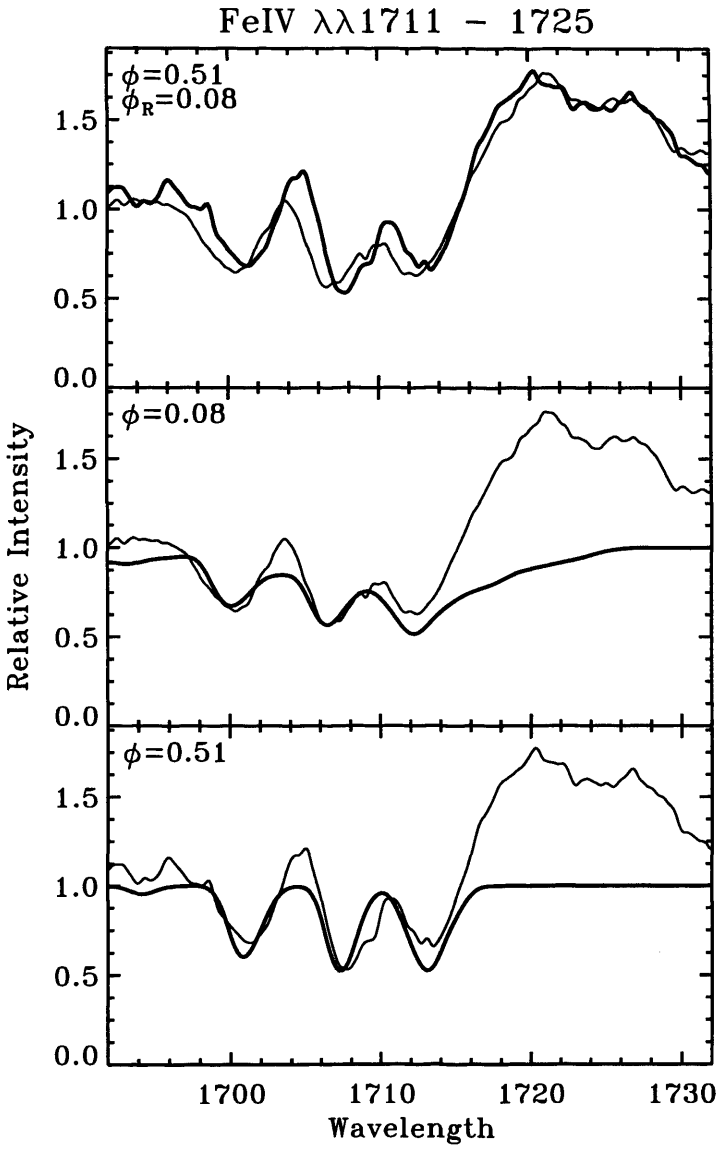

Figure 8.18: The Fe IV λ1711 – 1725 calculated profile. The top panel shows the observed profiles at $\phi = 0.08$ (*thin line*) and $\phi = 0.51$ (*thick line*). The lower two panels show the observed (*thin line*) and calculated (*thick line*) profiles at $\phi = 0.08$ (*middle*) and $\phi = 0.51$ (*bottom*).

to this feature or that the ionization balance used was not correct. However, by varying the abundance and ionization balance it was not possible to maintain the fit to the lines and eliminate this feature. At $\phi = 0.51$ the model produces an excellent fit.

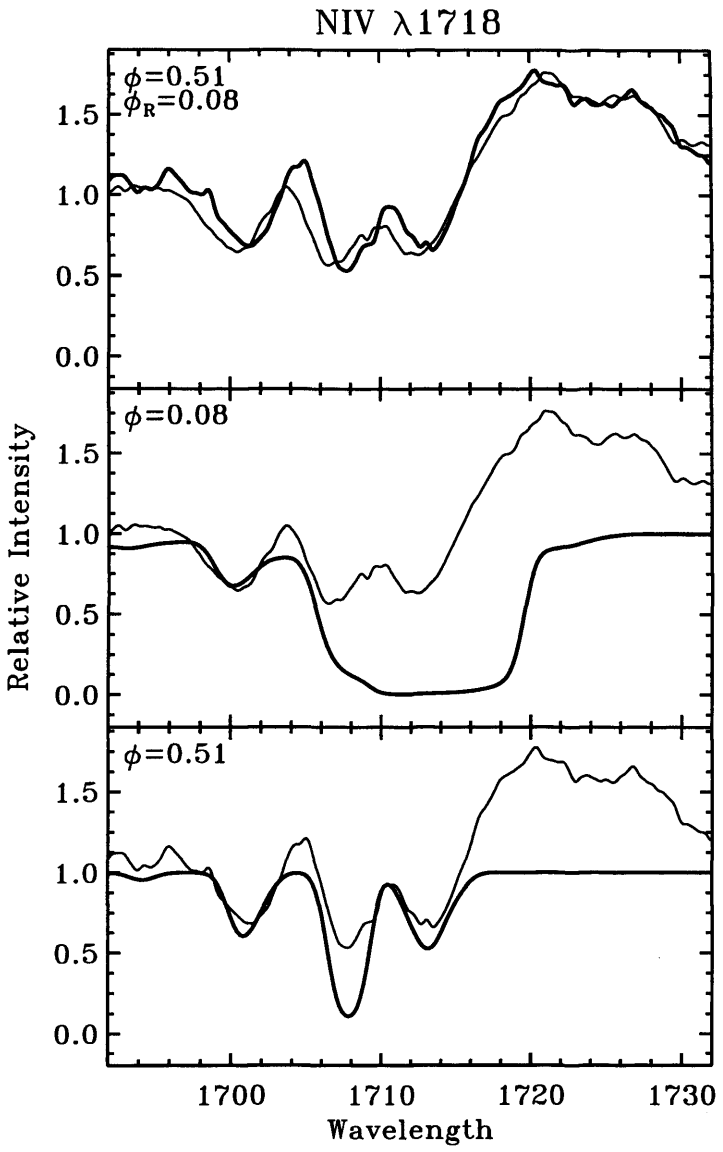

Figure 8.19: The region of the Fe IV λ1711 – 1725 lines showing the calculated profile including the N IV λ1718 line. The top panel shows the observed profiles at $\phi = 0.08$ (*thin line*) and $\phi = 0.51$ (*thick line*). The lower two panels show the observed (*thin line*) and calculated (*thick line*) profiles at $\phi = 0.08$ (*middle*) and $\phi = 0.51$ (*bottom*). The same region without the N IV line is shown in Figure 8.18.

8.8.5 Limit on N IV λ1718

By modelling this region of the spectrum, including the N IV λ1718 line with the Fe IV lines as in § 8.8.4, it is possible to place some limit on the nitrogen abundance.

Figure 8.19 shows the results with N/He = 10^{-5}. At $\phi = 0.08$ the line in the wind is saturated, so by implication it would also be saturated in the spectrum of the WR component alone. The red edge of the profile is very uncertain because the N IV line, if present, would contribute some emission, and there is also emission from other lines. However, the important point is that the difference between the two calculated spectra suggests a large variation in the region $\lambda\lambda$1710 – 1720 Å which is not observed. The profile at $\phi = 0.51$ suggests that the line present at λ1708 Å should be about twice as strong as observed with this level of nitrogen. Reducing the N/He ratio by a factor of 10 removes this difference at $\phi = 0.51$ but the model still suggests more variation than is observed in the $\lambda\lambda$1710 – 1720 Å region. Given the uncertainties in this process it is reasonable to take a conservative limit of N/He $< 10^{-5}$.

8.9 The shape of the shock zone

In the model the shock zone is taken as conical and tilted at a small angle to the line joining the two stars, to reflect orbital motion. Although this is a simple arrangement it correctly predicts the onset of the shift in the spectrum at $\phi \sim 0.4$ and provides an adequate fit to the lines at $\phi = 0.51$. However, at later phases the model does not correctly predict the observed shift in the spectrum. By this time the cone has moved too far from the line of sight and the stars are no longer viewed through the shock zone. The fact that the spectrum shift is observed to $\phi = 0.84$ implies that the shock zone still crosses the line of sight at these late phases. As this is impossible if the shock zone is conical it must mean that it is curved, which of course, is what is predicted. It is possible to crudely mimic this curvature by progressively increasing the offset angle with phase. When this is done the shifts are reproduced as observed.

8.10 Conclusions

The first conclusion is that the phase variation of the principal lines is well explained by the model. The detail of the intensity variations of the strong emission lines is also generally consistent with the model although it was less successful with the variation

in the inner part of the wind. As the adopted temperature structure is to some extent extrapolated towards the central regions this deviation is not too unexpected. The behaviour of the absorption lines is very well described by the model, both in terms of intensity and velocity variation. It has enabled abundance measurements which suggest Si (crudely) and Fe (more realistically) are about solar, and has placed an upper limit on N/He $< 1.0^{-5}$. The failure of the model to reproduce the velocity shifts at later phases has led to the discovery that the shock zone is curved. Although this is expected, evidence for it has not been seen before and it implies that a simple conical model is inadequate for intermediate- and short-period systems. The curvature may also explain some of the detailed difference in behaviour between some lines.

The analysis has also revealed some inconsistencies. The difference between the optical and UV determined luminosity ratios is about a factor of 2, but the UV measurement is based on line ratios showing considerable scatter. As discussed in § 8.4 there is evidence that the emission lines in HD 152270 are particularly strong; the alternative being that the O star is weaker than assumed, with $L_{\rm O}/L_{\rm WR} = 1/2 - 1$ (see Figures 8.2 and 8.3). However, the phase-dependent variations of the saturated lines typically show a range of $\sim 2/3$ of the pseudo continuum. Unless there are any additional factors this must represent the total luminosity of the O star, which implies $L_{\rm O}/L_{\rm WR} = 2$, and for obvious reasons was the value chosen for the modelling. The analysis also highlights variation in the emission lines which requires another explanation. Additional variations to the red of the rest wavelength amounting to ~ 0.3 of the continuum are clearly seen in He II λ1640, Si IV λ1402, O IV λ1342 and possibly C IV λ1548, 1550, which cannot be due to selective absorption by the wind. Also the C III λ2297 line and probably C III λ 1175 apparently shows a variation amounting to the combined continuum luminosity of the system (§ 8.8.3, Figure 8.11). The complexity of the variations makes it difficult to compare the profiles with the predicted behaviour of the additional emission peaks produced by the shock zone as given by Lührs (1997). From the profiles of the Si IV λ1393, 1402 (Figure 8.7.3) and C III λ2297 lines there are certainly no moving components than could be associated with this additional emission. However, there is undeniably excess emission and its most likely origin is in the shock zone. The effect is not as strong as in γ^2 Vel possibly

because the system is smaller and the terminal velocities aren't reached before the winds collide, or because the inclination is lower reducing the change in velocity.

The analysis also suggests that the momentum ratio of the O and WR star is not quite the same as that deduced from the measured mass-loss rates and terminal velocities. The line variation suggests that the shock cone is wider than calculated implying that the mass-loss rate of the WR star is a factor of ~ 2 lower (or the O star a factor of ~ 2 higher) than assumed.

Line identification in WR stars is a particularly difficult problem because the features are very broad and almost invariably contain blends due to different elements. Also the uncertainty in the level of the continuum makes it difficult to unambiguously identify dips in the spectrum as absorption lines or gaps between emission lines. The behaviour of the lines in HD 152270 makes it possible to use the shift caused by the passage of the shock zone to identify absorption lines. Combined with some simple spectrum synthesis from the model this could prove to be an extremely powerful instrument of line identification.

Chapter 9

Conclusions

Observations of the line-profile variations of γ^2 Vel and HD 152270 have been discussed in some detail in the context of selective absorption by the WR wind and wind collisions. Both stars show complex line-profile variations with phase. The large-scale variations in the strengths of the lines are smooth and progressive but around, and after, inferior conjunction the variations become much more complex. In the case of γ^2 Vel there are clear signs of the O star, with increasing visibility of the O-star spectral features, and a reduction in the strength of the WR wind lines, which is consistent with the view that the system is being seen through the cavity caused by the O-star wind. At the phase of maximum visibility of the O star the X-ray flux, due to the wind collision, is seen to peak sharply (Figure 7.1). The strength of the O-star lines is such that it seems likely that the line of sight actually passes along the compression region of the O-star wind, adjacent to the contact discontinuity, rather than the undisturbed wind. The inclination of HD 152270 is lower and the variations are more consistent with the view that, at inferior conjunction, the system is seen more along the outer edge of the shock zone. Features that are attributable to the O star are seen but they are less secure than for γ^2 Vel and also have to be stronger than is usually seen in O stars, again suggesting the influence of an O-star-wind compression region. Both systems show complex minor variations in strength and velocity which are probably attributable to the passage of the shock zone across the line of sight.

An absorption-line model has been developed which is able to quantify the change

in absorption with orbital phase. The model shows that a wide range of phase-dependent variations are possible, depending on the ionization balance of the wind and the velocity law. With the introduction of the shock zone much more complex variations in line strength and velocity are produced, which are sensitive to orbital inclination and the geometry of the shock zone (§ 5.7).

However, the current work has shown that from simple assumptions about the structure of the wind it is possible to model the selective absorption quantitatively, and successfully match the line profiles, as with the C II λ1335 and C III] λ1909 lines. The variations of the weaker absorption lines, particularly the Fe IV pseudo continuum, have been shown to be quantitatively consistent with the expectations of selective absorption. The model has been able to follow the variations in intensity and velocity, in a consistent way for the weaker and stronger lines alike. The agreement with saturated lines is generally more qualitative, and qualified. Part of the variation is consistent with the interpretation of selective absorption, but part is clearly not.

Using the derived model it has been possible to fit convincingly the Fe IV pseudo-continuum lines and determine an iron abundance which is approximately 1 – 2 times solar in both γ^2 Vel and HD 152270. By modelling the region around the N IV λ1718 line it has been possible to reduce the upper limit of the nitrogen abundance in WC stars by about 2 orders of magnitude, to N/He $< 10^{-4}$ and $< 10^{-5}$ by number, giving C/N > 1000 and > 20000, in γ^2 Vel and HD 152270 respectively. The carbon abundance is not tightly constrained but gives C/He $\sim 0.1 - 0.2$ which is in line with other recent determinations (Eenens & Williams 1992). The saturated absorptions in general yield little information about the wind structure but the modelled profiles are consistent with what is observed. From the Si IV λ1393, 1402 doublet it is possible to draw a weak conclusion that the Si abundance is of the order of solar. These lines have not allowed any investigation of the velocity law.

The emission lines have been shown to vary by more than can be explained by selective absorption alone, e.g., C IV λ 1548 1550, C III λ11175, 1247 and 2297, and Si IV λ1393, 1402, or in the case of C III] λ1909 and probably O IV λ1342, in a way which is inconsistent with selective absorption. These variations are broadly consistent with the scenario of excess emission from the shock zone fuelled by the colliding winds

(Lührs 1997). In both γ^2 Vel and to a lesser extent HD 152270 the ratios of the emission line strengths relative to single WCL stars suggest unusually strong lines which provides additional support to the idea of excess emission. The level of the excess emission in the lines is probably very large. In γ^2 Vel it is approximately equal to that of the O star, i.e. ~ 0.8 of the combined pseudo continuum and in HD 152270 is rather less, possibly ~ 0.3 of the combined pseudo continuum.

The spectra show complex variations, well beyond what can be described by the model. Both stars show continued activity after inferior conjunction as the O star returns to the back of the system. In HD 152270 the spectrum shows a clear shift in velocity which is predicted by the model to occur when the line of sight passes into the shock zone and is due to the deflection of material onto the contact surface. These and other details point to the shock zone not being conical as assumed by the model, but being curved, as expected due to orbital motion. Curvature of the shock zone would also help to explain the smooth transition of the line of sight from the WR wind to the shock zone.

The successes and limitations of the model which appear from this study suggest several lines for future work. Firstly, the model should be applied to other systems for which suitable observations are available. High resolution *IUE* spectra are available most importantly for HD 97152 (similar period to HD 152270) and WR140 (period 8 years), but also for a number of WN+O systems. The geometry could be improved to account for the curvature of the wind but at best this will still be a crude approximation of what is a complex hydrodynamical process. However, it must be remembered that the uncertainty caused by the excess emission limits the application of this technique. The ionization structure of the wind was deliberately chosen to be simple in form but it may conceal significant differences in the populations of absorbers responsible for important lines. In this respect one improvement would be to use the results from modern model atmospheres. The analysis is also restricted by the lack of suitable lines, both to constrain the model, and to explore the wind. An investigation of lines in the *Copernicus* wavelength region may pay dividends. Finally, a simple programme of line identification in HD152270 should be undertaken.

References

Abbott D.C., Bieging J.H., Churchwell E., Torres A.V., 1986, ApJ 303, 239

Abbott D.C., Lucy L., 1985, ApJ 288, 679

Allen C.W., 1973, *Astrophysical Quantities*, 3rd edn (Athlone Press)

Altenhoff W.J., Thum C., Wendker H.J., 1994, A&A 281, 161

Annuk K., 1991, *Wolf-Rayet Stars and Interrelations with Other Massive Stars in Galaxies*, eds. K. van der Hucht & B. Hidayat (Kluwer), IAU Symposium No. 143, p.245

Antokhin I.I., 1996, *33rd Liege International Astrophysical Colloquium, Wolf-Rayet Stars in the Framework of Stellar Evolution*, eds. J.-M. Vreux & P. Conti (Kluwer), p.177

Antokhin I.I., Bertrand J.-F., Lamontagne R., Moffat A.F.J., Matthews J.M., 1994a, AJ 107, 2179

Antokhin I.I., Bertrand J.-F., Lamontagne R., Moffat A.F.J., Matthews J.M., 1994b in prep

Aslanov A.A., Cherepashchuk A.M., 1990, Soviet Astron. A.J. 34, 602

Aspin C., Simmons J.F.L., Brown J.C., 1981, MN 194, 283

Auer L.H., Colomé C., Koenigsberger G., 1988, *A Decade of UV Astronomy with the IUE Satellite*, ESA SP-281 Volume 1, p.193

Auer L.H., Koenigsberger G., 1994, ApJ 438, 859

Baade D., Schmutz W., van Kerkwijk M., 1990, A&A 240, 105

Balona L.A., Shoobrook R.R., 1984, MN 211, 375

Balona L.A., et al. 1995, MN 276, 627

Barlow M.J., 1982, *Wolf-Rayet Stars: Observations, Physics, Evolution*, eds. C. de Loore & A.J. Willis (Reidel), IAU Symposium No. 99, p.149

Barlow M.J., Hummer D.C., 1982, *Wolf-Rayet Stars: Observations, Physics, Evolution*, eds. C. de Loore & A.J. Willis (Reidel), IAU Symposium No. 99, p.99

Barlow M.J., Roche P.F., Aitken D.K., 1988, MN 232, 821

Baschek B., Scholz M., 1971, A&A 11, 83

Beals C.S., 1929, MN 90, 202

Bhatia A.K., Underhill A.B., 1988, ApJ Suppl. 67, 187

Bjorkman J.E., Cassinelli J.P., 1993, ApJ 409, 429

Bohannan B., 1990, *Proceedings of the First Boulder-Munich Workshop: Properties of Hot, Luminous Stars*, ed. C.D. Garmany , ASP Conference Series 7, 39

Brown J.C., McLean I.S., Emslie A.G., 1978, A&A 68, 415

Brown J.C., Aspin C., Simmons J.F.L., McLean I.S., 1982, MN 198, 787

Brownsberger K.R., Conti P.S., 1993, Bull. Am. Astron. Soc. 191, 128.03

Burton W.M., Evans R.G., Griffin W.G., Lewis C., Paxton H.J.B., Shenton D.B., Macchetto F., Boksenberg A., Wilson R., 1973, Nature 246, 37

Burton W.M., Evans R.G., Griffin W.G., 1975, Phil. Trans. R. Soc. Lond. A. 279, 355

Cassinelli J.P., 1991, *Wolf-Rayet Stars and Interrelations with Other Massive Stars in Galaxies*, eds. K. van der Hucht & B. Hidayat (Kluwer), IAU Symposium No. 143, p.289

Castor J.I., Abbott D.C., Kline R.I., 1975, ApJ 195, 157 (CAK)

Chlebowski T., Garmany C.D., 1991, ApJ 368, 241

Cherepashchuk A.M., 1976, Soviet Astron. A.J. Letts. 2, 138

Cherepashchuk A.M., 1996, *33rd Liege International Astrophysical Colloquium, Wolf-Rayet Stars in the Framework of Stellar Evolution*, eds. J.-M. Vreux & P. Conti (Kluwer), p.155

Clampin M., Nota A., Golimowski D.A., Leitherer C., Durrance S.T., 1993, ApJ Letts. 410, L35

Conti P.S., Smith L.F., 1972, ApJ 172, 623

Conti P.S., 1976, Mim. Soc. Roy. Sci. Liège 6e Sér., Tome IX, p.193

Conti P.S., Ebbets 1977, ApJ 213, 438

Conti P.S., Leep E.M., Perry D., 1983, ApJ 268, 228

Conti P.S., Bohannan B., 1989, *Physics of Luminous Blue Variables*, eds. K. Davidson et al. (Kluwer), IAU Colloquium No. 113, p.297

Conti P.S., Massey P., 1989, ApJ 337, 251

Crawford I.A., 1989 MN 241, 575

Crawford I.A., 1992 MN 259, 47

Crawford I.A., 1995 MN 277, 458

Crowther P.A., Smith L.J., Willis A.J., 1995a, A&A 293, 172

Crowther P.A., Smith L.J., Hillier D.J., Schmutz W., 1995b, A&A 293, 427

Crowther P.A., Smith L.J., Hillier D.J., 1995c, A&A 302, 457

Crowther P.A., Bohannan B, 1997, A&A 317, 532

Crowther P.A., Smith L.J., 1997, A&A 320, 500

Crowther P.A., Szeifert T., Stahl O., Zickgraf F.-J., 1997, A&A 318, 543

Dalton M.J., Crowther P.A., Willis A.J., 1995, *Wolf-Rayet Stars: Binaries, Colliding Winds, Evolution*, eds. K. van der Hucht & P.M. Williams (Kluwer), IAU Symposium No. 163, p.154

De Greve J.P., 1996, *33rd Liege International Astrophysical Colloquium, Wolf-Rayet Stars in the Framework of Stellar Evolution*, eds. J.-M. Vreux & P. Conti (Kluwer), p.55

Eaton J.A., Cherepashchuk A.M., Khaliullin K.F., 1985, ApJ 297, 266

Eenens P.R.J., Williams P.M., 1992 MN 255, 227

Eenens P.R.J., Williams P.M., 1994 MN 269, 1082

Eichler D., Usov V., 1993, ApJ 402, 271

Firmani C., Koenigsberger G., Bisiacchi G.F., Moffat A.F.J., Isserstedt J., 1980, ApJ 239, 607

Friend D.B., Castor J.I., 1983, ApJ 272, 259

Friend D.B., Abbott D.C., 1986, ApJ 311, 701

Fullerton A.W., 1994, Astrophys. Space Sci. 221, 105

Gayley K.G., Owocki S.P., Cranmer S.R., 1997, ApJ 475, 786

Ganesh K.S., Bappu M.K.V., 1967, Kodaikanal Obs. Bull. No. 183

van Genderen A.M., Bijleveld W., van Groningen E., 1984, A&A Suppl. 58, 537

van Genderen A.M., van der Hucht K.A., Larsen I., 1990, A&A 229, 123

Giddings J., Rees P., Mills D., Clayton M., 1996, *IUEDR - IUE Data Reduction Package, version 3.2-0*, Starlink User Note 37

Gies D.R., Lambert D.L., 1992, ApJ 387, 673

Gosset E., Rauw G., Manfroid J., Vreux J-M., 1994, *The Impact of Long-Term Monitoring on Variable Star Research, Proc. NATO Workshop*, (Kluwer) eds. C. Sterken & M.J.H. de Groot, p.101

Hanbury Brown R., Davies J., Herbinson-Evans D., Allen L.R., 1970, MN 148, 103

Hanbury Brown R., Davies J., Lake R.J.W., Thompson R.J., 1974, MN 167, 475

Hamann W.-R., Wessolowski U., 1990, A&A 227, 171

Hamann W.-R., Leuenhagen U., Koesterke L., Wessolowski U., 1992, A&A 255, 200

Hamann W.-R., 1996, *33rd Liege International Astrophysical Colloquium, Wolf-Rayet Stars in the Framework of Stellar Evolution*, eds. J.-M. Vreux & P. Conti (Kluwer),

Harries T.J., Howarth I.D., 1996, A&A 310, 533

Harries T.J., Hilditch R.W., 1997, MN 291, 544

Hatchett S.P., McCray R., 1977, ApJ 211, 552

Herrero A., Kudritzki R.P., Vilchez J.M., Kunze D., Butler K., Haser S., 1992, A&A 261, 209

Hester J.J., Light R.M., Westphal J.A., Currie D.G., Groth E.J., Holtzman J.A., Lauer T.R., O'Neil E.J., 1991, AJ 102, 654

van den Heuvel E.P.J., 1976, *IAU Symposium No. 73*, eds. P. Eggleton et al., p.35

Hillier D.J., 1987a, ApJ Suppl. 63, 947

Hillier D.J., 1987b, ApJ Suppl. 63, 965

Hillier D.J., 1988, ApJ 327, 822

Hillier D.J., 1989, ApJ 347, 392

Hillier D.J., 1990, A&A 231 116

Hillier D.J., Allen D.A., 1992, A&A 262, 153

Hillier D.J., Kudritzki R.P., Pauldrach A.W., Baade D., Cassinelli J.P., Puls J., Schmitt J.H.M.M., 1993, A&A 276, 117

Hillier D.J., 1995, *Wolf-Rayet Stars: Binaries, Colliding Winds, Evolution*, eds. K. van der Hucht & P.M. Williams (Kluwer), IAU Symposium No. 163, p.116

Hillier D.J., 1996, *33rd Liege International Astrophysical Colloquium, Wolf-Rayet Stars in the Framework of Stellar Evolution*, eds. J.-M. Vreux & P. Conti (Kluwer), p.509

Hiltner W.A., Schild R.E., 1966, ApJ 143, 770

Howarth I.D., Willis A.J., Stickland D.J., 1982, *Proceedings of the Third European IUE conference*, Madrid, p.331

Howarth I.D., 1984, MN 211, 167

Howarth I.D., Prinja R.K., 1989, ApJ Suppl. 69, 527

Howarth I.D., Prinja R.K., Massa D., 1995, ApJ Letts. 452, L65

Howarth I.D., Murray J., Mills D., Berry D.S., 1996, *DIPSO (V3.3) – A friendly spectrum analysis program* , Starlink User Note 50

Howarth I.D., Siebert K.W., Hussain G., Prinja R.K., 1997, MN 284, 265

Hubeny I., Heap S.R., Lanz T., 1998, *Proceedings of the Second Boulder-Munich Workshop: Properties of Hot, Luminous Stars*, ed. I.D. Howarth, ASP Conference Series 131, p.108

van der Hucht K.A., 1975, in *Astronomy in the Ultraviolet*, Phil. Trans. R. Soc. Lond. A. 279, 451

van der Hucht K.A., Conti P.S., Lundström I., Stenholm B., 1981, *The Sixth Catalogue of Galactic Wolf-Rayet Stars; Their Past and Present*, Space Sci. Rev. 28, 227

van der Hucht K.A., Cassinelli J.P., Williams P.M., 1986, A&A 168, 111

van der Hucht K.A., Hidayat B., Admiranto A.G., Supelli K.R., Doom C., 1988, A&A 199, 217

van der Hucht K.A., 1996, *33rd Liege International Astrophysical Colloquium, Wolf-Rayet Stars in the Framework of Stellar Evolution*, eds. J.-M. Vreux & P. Conti (Kluwer), , p.1

van der Hucht K.A., Schrijver H., Stenholm B., et al., 1997, New A. 2, 245

Humphreys R., Davidson K., 1979, ApJ 232, 409

Humphreys R., Davidson K., 1994, PASP 106, 1025

Hutchings J.B., Massey P., 1983, PASP 95, 151

Ignace R., Cassinelli J.P., Bjorkman J.E., 1996, ApJ 459, 671

Jeffers S.J., Stiff T., Weller W.G., 1985, AJ 90, 1852

Kallrath J., 1991, MN 248, 653

Kaper L., Henrichs H.F., 1994, Astrophys. Space Sci. 221, 115

van Kerkwijk M.H., Geballe T.R., King D.L., van der Klis M., van Paradijs J., 1996, A&A 314, 521

Kilian J., Montenbruck O., Nissen P.E., 1994, A&A 284, 437

Kippenhahn R., Weigert A., 1967, Z.f.Astrof. 65, 251

Koenigsberger G., Auer L.H., 1985, ApJ 297, 255

Koenigsberger G., Moffat A.F.J., Auer L.H., 1987, ApJ Letts. 322, L41

Koenigsberger G., Moffat A.F.J., Auer L.H., 1988, *A Decade of UV Astronomy with the IUE Satellite*, ESA SP-281 Volume 1, p.197

Koenigsberger G., 1990, A&A 235, 282

Koesterke L., Hamann W.-R., Wessolowski U., 1992, A&A 261, 535

Kondo Y., Feibelman W.A., West D.K., 1982, ApJ 252, 208

Kudritzki R.P., 1996, *33rd Liege International Astrophysical Colloquium, Wolf-Rayet Stars in the Framework of Stellar Evolution*, eds. J.-M. Vreux & P. Conti (Kluwer), p.467

Kuhi L.V., 1973, *Wolf-Rayet and High Temperature Stars*, eds. M.K.V. Bappu & R.N. Thomas (Reidel), IAU Symposium No. 49, p.205

Lamers H.J.G.L.M, Maeder A., Schmutz W., Cassinelli J.P., 1990, *Angular Momentum and Mass Loss from Hot Stars*, eds. L.A. Willson & R. Stalio (Kluwer), NATO ASI Series C 316, p.349

Lamers H.J.G.L.M, Maeder A., Schmutz W., Cassinelli J.P., 1991, ApJ 368, 538

Lamers H.J.G.L.M, Leitherer C., 1993, ApJ 412, 771

Lamontagne R., Moffat A.F.J., Drissen L., Robert C., Matthews J.M., 1996, AJ 112, 2227

Langer N., El Eid M.F., Fricke K.J., 1985, A&A 145, 179

Langer N., 1991, A&A 248, 531

Langer N., Hamann W.-R., Lennon M., Najarro F., Pauldrach A.W.A., Puls J., 1994, A&A 290, 819

Leitherer C., Chapman L.M., Koribalski B., 1997, ApJ 481, 898

Lèpine S., 1994, *Instability and Variability of Hot Star Winds*, eds. A.F.J. Moffat, S.P. Owocki, A.W. Fullerton & N. St.-Louis (Kluwer), Astrophys. Space Sci. 221, 371

Lèpine S., 1995, *Wolf-Rayet Stars: Binaries, Colliding Winds, Evolution*, eds. K. van der Hucht & P.M. Williams (Kluwer), IAU Symposium No. 163, p.60

Lloyd C., Stickland D.J., 1995a, *Wolf-Rayet Stars: Binaries, Colliding Winds, Evolution*, eds. K. van der Hucht & P.M. Williams (Kluwer), IAU Symposium No. 163, p.58

Lloyd C., Stickland D.J., 1995b, *Wolf-Rayet Stars: Binaries, Colliding Winds, Evolution*, eds. K. van der Hucht & P.M. Williams (Kluwer), IAU Symposium No. 163, p.239

Lucy L.B., Soloman P.M., 1970, ApJ 159, 879

Lucy L.B., 1982, ApJ 255, 278

Lucy L.B., Abbott D.C., 1993, ApJ 405, 738

Lührs S., 1997, PASP 109, 504

Luna H.G., 1982, PASP 94, 695

Maeder A., 1987, A&A 178, 159

Maeder A., 1991, A&A 242, 93

Maeder A., Meynet G., 1994, A&A 287, 803

Maeder A., 1996, *33rd Liege International Astrophysical Colloquium, Wolf-Rayet Stars in the Framework of Stellar Evolution*, eds. J.-M. Vreux & P. Conti (Kluwer), p.39

Massa D. et al., 1995, ApJ 452, L53

Mazzali P.A., 1990, A&A 238, 191

Meynet G., Mermilliod J.-C., Maeder A., 1993, A&A Suppl. 98, 477

Meynet G., Maeder A., Schaller G., Schaerer D., Charbommel C., 1994, A&A Suppl. 103, 97

Mihalas D., 1987, *Stellar Atmospheres*, 2nd edn (Freeman & Co.),

Moffat A.F.J., 1977, A&A 57, 151

Moffat A.F.J., 1982, *Wolf-Rayet Stars: Observations, Physics, Evolution*, eds. C. de Loore & A.J. Willis (Reidel), IAU Symposium No. 99, p.263

Moffat A.F.J., Vogt N., Paquin G., Lamontagne R., Barrera L.H., 1986, AJ 91, 1386

Moffat A.F.J., Drissen L., Lamontagne R., Robert C., 1988, ApJ 334, 1038

Moffat A.F.J., Robert C., 1991, *Wolf-Rayet Stars and Interrelations with Other Massive Stars in Galaxies*, eds. K. van der Hucht & B. Hidayat (Kluwer), IAU Symposium No. 143, p.109

Moffat A.F.J., Piirola V., 1993, ApJ 413, 724

Moffat A.F.J., Lèpine S., Henriksen R.N., Robert C., 1994, Astrophys. Space Sci. 216, 55

Moffat A.F.J., 1995, *Wolf-Rayet Stars: Binaries, Colliding Winds, Evolution*, eds. K. van der Hucht & P.M. Williams (Kluwer), IAU Symposium No. 163, p.213

Moffat A.F.J., 1996, *33rd Liege International Astrophysical Colloquium, Wolf-Rayet Stars in the Framework of Stellar Evolution*, eds. J.-M. Vreux & P. Conti (Kluwer), p.199

Morris P., van der Hucht, K.,Eenens P.R.J., Williams P.M., 1996, *33rd Liege International Astrophysical Colloquium, Wolf-Rayet Stars in the Framework of Stellar Evolution*, eds. J.-M. Vreux & P. Conti (Kluwer), p.405

Morton D.C., 1991, ApJ Suppl. 77, 119

Neutsch W., Schmidt H., Seggewiss W., 1981, Acta Astron. 31, 197

Nichols J.S., Fesen R.A., 1994, A&A 291, 283

Niedzielski A., 1994, A&A 282, 529

Niemela V.S., Sahade J., 1980, ApJ 238, 244

Nota A., Leitherer C., Clampin M., Greenfield P., Golimowski D.A., 1992, ApJ 398, 621

Nota A., Clampin M., Sirianni M., Greenfield P., Golimowski D.A., 1995, *Wolf-Rayet Stars: Binaries, Colliding Winds, Evolution*, eds. K. van der Hucht & P.M. Williams (Kluwer), IAU Symposium No. 163, p.78

Nota A., Pasquali A., Drissen L.,Leitherer C., Robert C., Moffat A.F.J., Schmutz W., 1996, ApJ Suppl. 102, 383

Nugis T., 1991, *Wolf-Rayet Stars and Interrelations with Other Massive Stars in Galaxies*, eds. K. van der Hucht & B. Hidayat (Kluwer), IAU Symposium No. 143, p.75

Nussbaumer H., Walder R., 1993, A&A 278, 209

Olsen G.L., Ebbets D., 1981, ApJ 248, 1021

Owocki S.P., 1991, *Wolf-Rayet Stars and Interrelations with Other Massive Stars in Galaxies*, eds. K. van der Hucht & B. Hidayat (Kluwer), IAU Symposium No. 143, p.155

Owocki S.P., Cranmer S.R, Blondin J.M., 1994, ApJ 424, 887

Owocki S.P., Gayley K.G., 1995, *Wolf-Rayet Stars: Binaries, Colliding Winds, Evolution*, eds. K. van der Hucht & P.M. Williams (Kluwer), IAU Symposium No. 163, p.138

Owocki S.P., Gayley K.G., Cranmer S.R., 1998, *Proceedings of the Second Boulder-Munich Workshop: Properties of Hot, Luminous Stars*, ed. I.D. Howarth, ASP Conference Series 131, p.237

Paczynski B., 1967, Acta Astron. 17, 355

Pauldrach A.W.A., Puls J., Hummer D.G., Kudritzki R.-P., 1985, A&A 148, L1

Pauldrach A.W.A., Puls J., Kudritzki R.-P., 1986, A&A 164, 86

Pike C.D., Stickland D.J., Willis A.J., 1983, Obs. 103, 154

Podsiadlowski P., Joss P.C., Hsu J.J.L., 1992, ApJ 391, 246

Polcaro V.F., Norci L., Rossi C., Viotti R., 1996, *33rd Liege International Astrophysical Colloquium, Wolf-Rayet Stars in the Framework of Stellar Evolution*, eds. J.-M. Vreux & P. Conti (Kluwer), p.23

Pollock A.M.T., 1987, ApJ 320, 283

Pollock A.M.T., 1989, ApJ 347, 409

Pollock A.M.T., 1995, *Wolf-Rayet Stars: Binaries, Colliding Winds, Evolution*, eds. K. van der Hucht & P.M. Williams (Kluwer), IAU Symposium No. 163, p.429

Pollock A.M.T., Haberl F., Corcoran M.F., 1995, *Wolf-Rayet Stars: Binaries, Colliding Winds, Evolution*, eds. K. van der Hucht & P.M. Williams (Kluwer), IAU Symposium No. 163, p.512

Prilutskii O., Usov V., 1976, Soviet Astron. A.J. 20, 2

Prinja R.K., Howarth I.D., 1988, MN 233, 123

Prinja R.K., Barlow M.J., Howarth I.D., 1990, ApJ 361, 607

Prinja R.K., 1992, *Nonisotropic and Variable Outflows for Stars*, eds. L. Drissen, C. Leitherer & A. Nota, ASP Conf. Series 22, p.167

Prinja R.K., Smith L.J., 1992, A&A 266, 377

Puls J., 1987, A&A 184, 227

Puls J., Kudritzki R.-P., Herrero A., Pauldrach A.W.A., Haser S.M., Lennon D.J., Gabler R., Voels S.A., Vilchez J.M., Wachter S., Feldmeier A., 1996, A&A 305, 171

Rees P., Giddings J., Mills D., Clayton M., 1996a, *IUEDR – Users Guide*, Starlink Miscellaneous Document 45

Rees P., Giddings J., Mills D., Clayton M., 1996b, *IUEDR – Reference Manual*, Starlink Guide 3

Reid A.H.N., Howarth I.D., 1996, A&A 311, 616

Robert C., Moffat A.F.J., Seggewiss W., 1991, *Wolf-Rayet Stars and Interrelations with Other Massive Stars in Galaxies*, eds. K. van der Hucht & B. Hidayat (Kluwer), IAU Symposium No. 143, p.147

Robert C., 1992, PhD thesis, Universitè de Montrèal

Rochowicz K., 1996, *33rd Liege International Astrophysical Colloquium, Wolf-Rayet Stars in the Framework of Stellar Evolution*, eds. J.-M. Vreux & P. Conti (Kluwer), p.311

Rosa M.R., Mathis J.S., 1990, *Proceedings of the First Boulder-Munich Workshop: Properties of Hot, Luminous Stars*, ed. C.D. Garmany , ASP Conference Series 7, p.135

Rumpl W.M., 1980, ApJ 241, 1055

Sahade J., 1955, PASP 67, 348

Santos J.F.C., Bica E., 1993, MN 260, 915

Schaerer D., 1995, *Wolf-Rayet Stars: Binaries, Colliding Winds, Evolution*, eds. K. van der Hucht & P.M. Williams (Kluwer), IAU Symposium No. 163, p.168

Schaerer D., Schmutz W., Grenon M., 1997, ApJ Letts. 484, L153

Schmutz W., 1990, *Angular Momentum and Mass Loss from Hot Stars*, eds. L.A. Willson & R. Stalio (Kluwer), NATO ASI Series C 316, p.227

Schmutz W., Vacca W.D., 1991, A&A Suppl. 89, 259

Schmutz W., Geballe T.R., Schild H., 1996, A&A 311, L25

Schmutz W., 1997, A&A 321, 268

Schmutz W., Schweickhardt J., Stahl O., Wolf B., Dumm Th., Gäng Th., Jankovics I., Kaufer A., Lehmann H., Mandel H., Peitz J., Rivinius Th., 1997, A&A 328, 219

Schmutz W., 1998, *Proceedings of the Second Boulder-Munich Workshop: Properties of Hot, Luminous Stars*, ed. I.D. Howarth, ASP Conference Series 131, p.119

Schulte-Ladbeck R.R., Meade M.R., Hillier D.J., 1992, *Nonisotropic and Variable Outflows for Stars*, eds. L. Drissen, C. Leitherer & A. Nota, ASP Conf. Series 22, p.118

Schulte-Ladbeck R.R., Clayton G.C., Meade M.R., 1993a, *Massive Stars: Their Lives in the Interstellar Medium*, (eds) J.P. Cassinelli & E.B. Churchwell, ASP Conference Series 35, p.237

Schulte-Ladbeck R.R., Leitherer C., Clayton G.C. Robert C., Meade M.R., 1993b, ApJ 407, 723

Schulte-Ladbeck R.R., Clayton G.C., Hillier D.J., Harries T.J., Howarth I.D., 1994, ApJ 429, 846

Schulte-Ladbeck R.R., Eenens P.J.R., Davies K., 1995, ApJ 454, 917

Schulte-Ladbeck R.R., Herald J.E., Eenens P.J.R., Morris P., 1996, *33rd Liege International Astrophysical Colloquium, Wolf-Rayet Stars in the Framework of Stellar Evolution*, eds. J.-M. Vreux & P. Conti (Kluwer), p.321

Seggewiss W, 1968, Veröffentl. Astron. Inst. Univ. Bonn 79

Seggewiss W, 1974, A&A 31, 211

Shore S.N., Brown D.N., ApJ 334, 1021

Smith H.J., 1955, Ph.D. thesis, Harvard University

Smith L.F., 1968a, MN 138, 109

Smith L.F., 1968b, MN 140, 409

Smith L.F., 1973ab, *Wolf-Rayet and High Temperature Stars*, eds. M.K.V. Bappu & R.N. Thomas (Reidel), IAU Symposium No. 49, p.15 *ibid* p.228

Smith L.F., Hummer D.G., 1988, MN 230, 511

Smith L.F., Maeder A., 1988, A&A 241, 77

Smith L.F., Meynet G., Mermilliod J.-C., 1994, A&A 287, 835

Smith L.F., 1995, *Wolf-Rayet Stars: Binaries, Colliding Winds, Evolution*, eds. K. van der Hucht & P.M. Williams (Kluwer), IAU Symposium No. 163, p.3

Smith L.F., Shara M.M., Moffat A.F.J., 1996, MN 281,163

Smith L.J., Willis A.J., 1982, MN 201, 451

Smith L.J., Willis A.J., 1983, A&A Suppl. 54, 229

Smith L.J., Crowther P.A., Prinja R.K., 1994, A&A 281, 833

Smith L.J., 1996, *33rd Liege International Astrophysical Colloquium, Wolf-Rayet Stars in the Framework of Stellar Evolution*, eds. J.-M. Vreux & P. Conti (Kluwer), p.381

Springman U., Puls J., 1995, *Wolf-Rayet Stars: Binaries, Colliding Winds, Evolution*, eds. K. van der Hucht & P.M. Williams (Kluwer), IAU Symposium No. 163, p.170

Springman U., Puls J., 1998, *Proceedings of the Second Boulder-Munich Workshop: Properties of Hot, Luminous Stars*, ed. I.D. Howarth, ASP Conference Series 131, p.286

St-Louis N., Drissen L., Moffat A.F.J., Bastien P., Tapia S., 1987, ApJ 322, 870

St-Louis N., Moffat A.F.J., Drissen L., Bastien P., Robert C., 1988, ApJ 330, 286

St-Louis N., Willis A.J., Stevens I.R., 1993, ApJ 415, 298

St-Louis N., Dalton, M.J., Marchenko S.V., Moffat A.F.J., Willis A.J., 1995, ApJ Letts. 452, L57

St-Louis N., Hill G., Moffat A.F.J., Bartzakos P., Antokhin I.I., 1996, *33rd Liege International Astrophysical Colloquium, Wolf-Rayet Stars in the Framework of Stellar Evolution*, eds. J.-M. Vreux & P. Conti (Kluwer), p.331

Stahl O., 1986, A&A 164, 321; Erratum 170, 197

Stevens I.R., Blondin J.M., Pollock A.M.T., 1992, ApJ 386, 265

Stevens I.R., 1993, ApJ 404, 281

Stevens I.R., Corcoran M.F., Willis A.J., Skinner S.L., Pollock A.M.T., Nagase F., Koyama K., 1996, MN 283, 589

Stickland D.J., Ford G., Lloyd C., Willis A.J., 1986, *New Insights in Astrophysics*, ESA SP-263 p.505

Stickland D.J., Lloyd C., 1990, Obs. 110, 1

Stickland D.J., Lloyd C., 1993, MN 264, 935

Stickland D.J., Lloyd C., 1995, Obs. 115, 90

Stickland D.J., Lloyd C., Penny L.R., Gies D.R., Bagnuolo W.G., 1996a, Obs. 116, 226

Stickland D.J., Lloyd C., Radziun-Woodham A., 1996b, MN 286, L21

Struve O., 1944a, ApJ 100, 189

Struve O., 1944b, ApJ 100, 384

Torres A.V., Conti P.S., Massey P., 1986, ApJ 300, 379

Underhill A.B., Nemec A.F.L., 1989, ApJ 345, 1008

Underhill A.B., Gilroy K.K., Hill G.M., Dinshaw N., 1990, ApJ 351, 666

Underhill A.B., 1996, *33rd Liege International Astrophysical Colloquium, Wolf-Rayet Stars in the Framework of Stellar Evolution*, eds. J.-M. Vreux & P. Conti (Kluwer), p.101

Usov V.V., 1995, *Wolf-Rayet Stars: Binaries, Colliding Winds, Evolution*, eds. K. van der Hucht & P.M. Williams (Kluwer), IAU Symposium No. 163, p.495

Vanbeveren D., 1995, A&A 294, 107

Vanbeveren D., 1996, *Evolutionary Processes in Binary Stars*, eds. M. Wijers, M. Davies & C. Tout (Kluwer), p.155

Venn K.A., 1993, ApJ 414, 316

Vreux J.-M., 1987, *Instabilities in Luminous Early-Type Stars*, eds. H. Lamers & C. de Loore (Reidel), Proc. Workshop in honour of C. de Jager, p.81

Vreux J.-M., Gosset E., Bohannan B., Conti P.S., 1992, A&A 256, 148

Walborn N.R., 1971, ApJ Letts. 167, L31

Walborn N.R., 1973, *Wolf-Rayet and High Temperature Stars*, eds. M.K.V. Bappu & R.N. Thomas (Reidel), IAU Symposium No. 49, in discussion after Conti's paper, p.104

Walborn N.R., 1977, ApJ 215, 53

Walborn N.R., 1988, *Atmospheric Diagnostics of Stellar Evolution*, ed. K. Nomoto (Springer), IAU Colloquium No. 108, p.70

Walder R., 1995, *Wolf-Rayet Stars: Binaries, Colliding Winds, Evolution*, eds. K. van der Hucht & P.M. Williams (Kluwer), IAU Symposium No. 163, p.420

Wallerstein G., Silk J., Jenkins E.B., 1980, ApJ 240, 834

Williams P.M., Eenens P.R.J., 1989, MN 240, 445

Williams P.M., van der Hucht K.A., Pollock A.M.T., Florkowski D.R., van der Woerd H., Wamsteker W., 1990, MN 243, 662

Williams P.M., 1996, *33rd Liege International Astrophysical Colloquium, Wolf-Rayet Stars in the Framework of Stellar Evolution*, eds. J.-M. Vreux & P. Conti (Kluwer), p.135

Willis A.J., Wilson R., 1976, A&A 47, 429

Willis A.J., Wilson R., Macchetto F., Beeckmans F., van der Hucht K.A., Stickland D.J., 1979, *The First Year of IUE*, University College London, p.394

Willis A.J., 1982, MN 198, 897

Willis A.J., van der Hucht K.A., Conti P.S., Garmany D., 1986, A&A Suppl. 63, 417

Willis A.J., Stickland D.J., 1990, A&A 232, 89

Willis A.J., 1991a, it Evolution of Stars: The Photospheric Abundance Connection, eds G. Michaud & A. Tutukov, p.195

Willis A.J., 1991b, *Wolf-Rayet Stars and Interrelations with Other Massive Stars in Galaxies*, eds. K. van der Hucht & B. Hidayat (Kluwer), IAU Symposium No. 143, p.265

Willis A.J., Schild H., Stevens I.R., 1995, A&A 298, 549

Willis A.J., Crowther P.A., 1996, *33rd Liege International Astrophysical Colloquium, Wolf-Rayet Stars in the Framework of Stellar Evolution*, eds. J.-M. Vreux & P. Conti (Kluwer), p.109

Willis A.J., Stevens I.R., 1996, A&A 310, 577

Willis A.J., Dessart, L., Crowther P.A., Morris P.W., Maeder A., Conti P.S., van der Hucht K.A., 1997, MN 290, 371

Wright A.E., Barlow M.J., 1975, MN 170, 41

Zahn J.P., 1992, A&A 265, 115